Doctor of Philosophy in Engineering

Department of Engineering

Italy

PhD in "Energy" Cycle XXXVI

Modeling and Control of Reversible Air-to-water Heat Pumps

PhD Student
Dhirendran Munith Kumar

PhD Coordinator
Prof. Riva Sanseverino Eleonora

Supervisor
Prof. Antonio Piacentino

Co-supervisor
Prof. Vincenzo Franzita

YEAR 2024

Acknowledgment

This thesis reflects my three years of research as a PhD student in 'Energy' at the University of Palermo. I am grateful to Prof. Antonio Piacentino and Prof. Vincenzo Franzita for providing me with this valuable opportunity to enter the world of research. A special acknowledgment goes to Prof. Pietro Catrini and Prof. Adriano Fagiolini for their consistent support, significant knowledge about research, and guidance on professional conduct, all of which undoubtedly benefit my career.

My heartfelt acknowledgment goes to my mentor Prof. Maurizio Cirrincone for motivating me to take up post-graduate research in the first place. I want to thank my lab colleagues Mr. Hamed Jafargholi, Mr. Guiseppe Dino, Mr. Ali, and Dr. Nguyen Quang for the constructive discussions in the University of Palermo PhD Lab. This opportunity significantly enhanced my experimental skills, introduced me to a different academic environment, and facilitated connections with people from around the world. Special thanks to Prof. Bibhya Sharma, Prof. Mansour Assaf, Dr. Krishneel Kumar, Dr. Rahul Kumar, Dr. Hiye Mudaliar, Mr. Siwan Narayan, Mr. Saiyad Kutty, Mr. Nathan Peter, Mr. Krish Raj, Mr. Shahil Kumar, and Mr. Krishnil Ram For their unwavering support during my research activities at the Laboratory in Fiji.

My sincere thanks to all,

Thank you!

Dedication

THIS THESIS IS DEDICATED TO MY FAMILY; FATHER – DHARMENDRAN KUMAR, MOTHER – MUNI LATA, SISTER – KAJAL RADHA SHIWANI, WIFE – SHIVANI LATA AND MY BABY DAUGHTER- YAADAVI KAAVYA LATA.

List of Publication

Kumar, D. M., Catrini, P., Piacentino, A., & Cirrincione, M. (2023a). Advanced modeling and energy-saving-oriented assessment of control strategies for air-cooled chillers in space cooling applications. *Energy Conversion and Management*, *291*, 117258. https://doi.org/10.1016/J.ENCONMAN.2023.117258

Kumar, D. M., Catrini, P., Piacentino, A., & Cirrincione, M. (2023b). Integrated Thermodynamic and Control Modeling of an Air-to-Water Heat Pump for Estimating Energy-Saving Potential and Flexibility in the Building Sector. *Sustainability (Switzerland)*, *15*(11). https://doi.org/10.3390/su15118664

Kumar, D. M., Narayan, S., Catrini, P., Cirrincione, M., Piacentino, A., & Fagiolini, A. (n.d.). Online Estimation of the Parameters and Diagnosis of Faults in an Air-cooled Chiller using Synchronous Reluctance motor drive. *Proceedings of the International Conference on Optimisation of Electrical and Electronic Equipment, OPTIM*, Istanbul. https://doi.org/10.1109/ACEMP-OPTIM57845.2023.10287042

Catrini, P., Villetta M. L., **Kumar, D. M**., Morale, M., Piacentino, A. (2024). Analysis of the operation of air-cooled chillers with variable-speed fans for advanced energy-saving-oriented control strategies, *Applied Energy*, Volume 367, 2024, 123393, ISSN 0306-2619, https://doi.org/10.1016/j.apenergy.2024.123393.

Kumar, K. S., Kumar, V., Vuruna, P., Naisorotabua, R. B., Prasad, R., **Kumar, D. M**., & Catrini, P. (n.d.). Comparative Study of SynRM and PMSM Efficiency in a Air-to-Water chiller using Variable Speed Drive. *2023 IEEE International Conference on Energy Technologies for Future Grids, ETFG 2023*, Wollongong. https://doi.org/10.1109/ETFG55873.2023.10407115

Buscemi, A., Catrini, P., Piacentino, A., Cardona, F., & **Kumar, D**.**M**. (2022). Energy-saving potential of ground source multiple chillers in simple and hybrid configurations for Mediterranean climates. *Energy Conversion and Management*, *263*. https://doi.org/10.1016/j.enconman.2022.115721

Chand, S. S., Prasad, R., Mudaliar, H. K., **Kumar, D. M**., Fagiolini, A., Benedetto, M. Di, & Cirrincione, M. (2023). Improving Power Delivery of Grid-Connected Induction Machine Based Wind Generators under Dynamic Conditions Using Feedforward Linear Neural Networks. *IEEE Access*, *11*, 63550–63564. https://doi.org/10.1109/ACCESS.2023.3288006

Table of Contents

List of figures:

List of Tables

Introduction

At present the global energy demand is at its peak compared to the past decades, a growth of 1.7% was recorded in 2022[1]. Overall global energy power mix for 2024 indicates the increase in renewables and immense focus is on adaptation of clean energy. European Union (EU) announced its REPowerEU and The Green Deal Industrial plan that reduces dependence on Russian fossil fuels and increases renewables by 50%[2]. Adaption of clean energy is largely anticipated worldwide, due to the recent policies for clean energy, political turmoil, and advancement in high power handling technologies. As a result, of the proposed plans of the EU, 50 GW worth of solar and wind technologies have been incorporated and it accounted for a 45% increase compared to the previous year. The rest of the world is also headed in the same direction as China deployed a massive 160 GW of renewable energy, accounting for about half of the total installed renewables for 2022. The Paris Agreement is the motivation factor for the boost of renewables, to aid in reducing greenhouse gas emissions and save smaller island nations. Energy consumption tends to fluctuate annually depending on various aspects, the major contributors include transportation, industries, and buildings. This thesis is oriented towards the energy consumption of buildings and understanding the vital role buildings currently play with renewables as a major source of energy.

Building

According to a recent study from the International Energy Agency[3] in 2022, buildings accounted for 30% of global final energy consumption and 26% of global energy-related emissions (8% being direct emissions in buildings and 18% indirect emissions from the production of electricity and heat used in buildings). Approximately, 38% of energy consumption in buildings is from heating, ventilation, AC, and refrigeration [4], [5], [6], [7], [8], [9] Focusing on heating, almost two-thirds of energy relies on fossil fuels[10], [11]. However, recent data showed that[3] the demand for natural gas dropped by more than 15% compared to 2021. Such a decline was consequent to the reduced space heating needs thanks to mild winter (almost 40%), while a substantial fraction was due to various gas-saving measures, hence it is vital to find novel ideas to reduce energy consumption without affecting comfort and air quality in the indoor environmentAn insight into the heating energy consumption that incorporates space and water heating. Recent studies suggest that two-thirds of heating energy relies on fossil fuels. However, the recent policies will reduce dependency from fossil fuels to renewables in the near future. Focusing on the cooling aspect, it

can be noted that 2022 was the fourth warmest year since the late 1900s, and it is a leading cause of heat stress often resulting in induced thermal comfort and labor productivity. As a result, a 5% increase in energy demand was noted in 2022 for space cooling which is bound to increase soon. Heating and cooling energy demand pose a risk to the overall electricity network since changes in weather patterns and increasing population tend to result in increased power demand and lead to power blackouts. It is important to understand the cooling and heating trend to prevent such actions. A huge opportunity exists in terms of energy and cost savings provided stringent policies and standards enforce minimum performance standards. The EU and united sates revised Energy Performance of Building Directives (EPBD) and zero net energy and zero net carbon standards respectively to make notable progress towards decarbonization[12].

Heat Pumps in Buildings sector: new opportunities

From a technological point of view, to reduce gas dependence from Russia and meet the heating demand sustainably, the REPowerEU plan proposed the cumulative installation of 10 million new hydronic heat pumps (HP) in the next 5 years and 30 million units in the buildings sector by 2030 [13]. In this respect, according to recent data HP sales in Europe enjoyed a record year, with sales growing by nearly 40%, reaching around 3 million installations and supporting the reduction in natural gas demand in 2022. Worth noting that HPs are currently considered key technologies not only for decarbonizing the heating sector in buildings but also for the achievement of 100% renewable energy systems [14], [15], [16]. In this respect, they could provide ancillary services to the power grid thus allowing for the integration of renewable energy sources (RES) [17], [18]. In particular, through demand response (DR) programs [19], HPs will be activated (or modulated and deactivated) in case of electricity surplus (or deficit) from RES, with the thermal energy produced directly consumed or stored in ad-hoc systems [20], [21]. Regarding the latter option, in the case of the connection of buildings to low-temperature heating networks, the heat produced onsite by the HPs could be sold to the grid, and buildings could thus contribute to a more sustainable heat generation [22]. Looking at the building scale, the adoption of HPs along with thermal storage contributes to increasing the so-called “flexibility”, which is the capability of the building to modify its demand to meet external requests from the grid while assuring occupants’ comfort [23], [24], [25], [26].

Area of Focus

The thesis will focus on the modeling of a reversible air-to-water HP where the thermodynamic aspects are jointly solved with the models of the electric motor used to drive compressors and one of the embedded controls. More specifically, the thesis will address the capability of the integrated modeling to provide insights into the dynamic response of the HP such as the time needed to reach new steady-steady operation, overshoot of supply water temperature after load change, number of compressors cycling per hour, etc. which are useful in the framework of novel applications of this technology. To show these capabilities, the dynamic response of HP for the two typical compressor management strategies: (i) a sequential control of multiple compressors, with compressors running at a constant speed, and (ii) a variable-speed control where the rotating speed of the compressors is continuously varied. the capability to analyze new HPs' management strategies aimed at increasing the seasonal COP or improving building flexibility. In this respect, this paper investigates the typical control of the HPs based on "heating (or cooling) curves" which assumes a variable temperature setpoint of the hot (cold water) water with the outdoor temperature. Finally, the capabilities of controller to minimize the effects of common faults such as fouling or improper charge on energy performance degradation will be investigated.

Thesis Outline

A concise description of the thesis outline is laid out. ***Chapter 1*** is dedicated to an in-depth literature review on various modeling techniques for Heating Ventilating and Air Conditioning (HVAC) systems, with a focus on different motors deployed in HVAC systems along with the appropriate control techniques. Finally, a focus on integrated thermodynamic and control modeling of reversible heat pumps is provided and literature gaps are outlined. In ***Chapter 2*** the model of an induction motor drive is presented. ***Chapter 3*** gives brief introduction to the basic concepts of a heat pump, the components, and the heating and cooling mode operations.It also provides different modelling techniques that will be used in this thesis of a reversible heat pump in cooling and heating mode. A state space model is also presented. ***Chapter 4***, gives the implementation of scalar control technique using a voltage source inverter with space vector modulation. The control of constant and variable speed with set water temperature is also discussed. ***Chapter 5***, consists of the advanced control techniques that are used to improve the system energy efficiency ratio and

coefficient of performance of the plant in various fault conditions. ***Chapter 6***, presents the results and discussion of the thesis for heating and cooling mode operation for a case study in Palermo, Italy. Finally, the conclusions and future works of the thesis are presented in the appendices.

Chapter 1: State of the art

Objectives:

The scope of the state-of-the-art involves:

- a thorough review of the recent and traditional technologies works will be reviewed that tend to address these impacts will be presented. Identify the major contributors and their impacts on society and the globe.

1.1 HVAC Modeling Techniques

Firstly, a summary of different types of HVAC modeling techniques of existing installed plants is presented[27], [28], [29]. Modelling of HVAC system is a sophisticated task, due to the wide range of complexity that is involved and the new advancements in the technology. A wide variety of modeling techniques are available in the literature for HVAC systems. Fig. 1 presents the three classes of HVAC models.

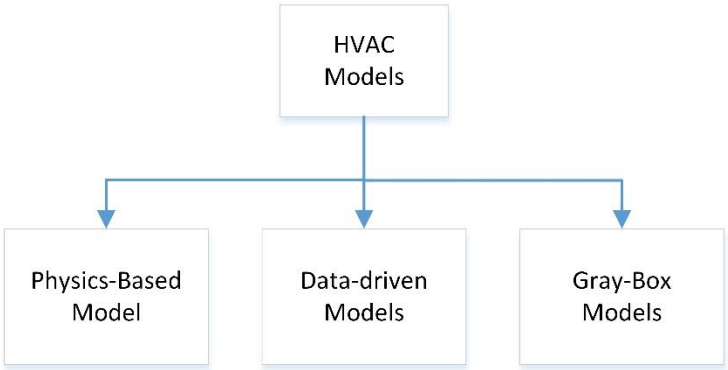

Figure 1 Types of HVAC models

I. Physics-based (White-box /Mathematical/forward) Models

As stated, Physic-based models are derived from fundamental laws of energy, taking into consideration mass balance, momentum, flow balance, and heat transfer. The models are developed for each component and the majority of the application is in the design stage, it is important to predict and analyze the performance with complex mathematical modeling. Examples of developed white-box models include the following components: sensor model[30], duct model[30], pump model[30], [31], [32], chiller model[33], [34], [35], cooling tower model[36], [37], [38], and coil models[28], [29]. Due to the complex nature of the HVAC system is difficult

to model each parameter. At times it is difficult to acquire certain parameters in a physics-based model[39], [40].

II. Data-driven (Black-box /inverse) Models

The concept of a data-driven model is to use mathematical techniques (statistical regression or artificial neural network (ANN))) to establish the characteristics between the input and output data of a real system[29]. This type of model does not pose any specific physical or mathematical characteristics of the existing plant[28]. Data-driven approaches are suitable for existing HVAC systems for performance improvement when sufficient data is available. As shown in Fig.2 data-driven approaches are classified into 9 types: Frequency domain model, Data mining model, Fuzzy logic model, Statistical model, State-space model, Geometric model, case-based model, Stochastic model, and instantaneous model.

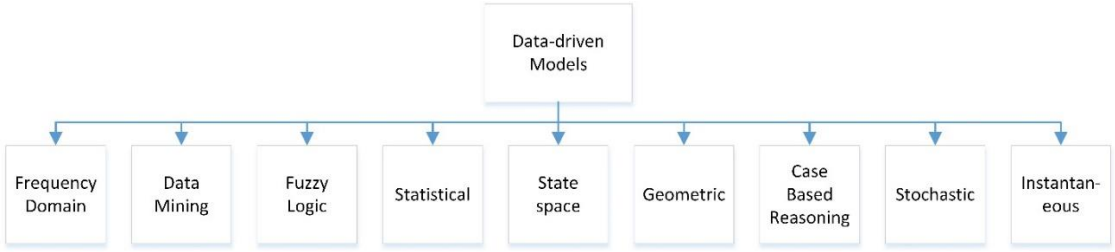

Figure 2 Data-driven model classification

Frequency domain model

The processes involved in an HVAC system are in general slow (e.g., zone temperature and humidity), due to the large thermal inertia of the system. Such systems can be modeled using first and second-order systems with a dead time to account for the inertia[41], [42], [43], [44]. First-order models are usually used to model linear processes and a Proportional integral and derivative (PID) controller tuning is sufficient. Contrary to second-order models which use advanced controllers within the HVAC system. Both the modeling techniques are used for linear and time-invariant (LTI) systems, hence inapplicable to complicated and time-varying dynamics.

A. Data mining model

Data mining models include ANN and Support Vector Machine (SVM) based models capable of characterizing complex and non-linear systems dynamics of the HVAC system[45]. ANN and SVM have been deployed in numerous research on HVAC systems as stated in the review article[29] The disadvantages of using both techniques are that no physical characteristics of the

HVAC system are interpreted, and the performance degrades when conditions deviate from training and testing conditions[46]

B. Fuzzy logic (FL) model

FL model includes rules based on if-then-else statements expressed as a table or database. It is divided into fuzzy adaptive network FAN), Takagi-Sugeno (T-S), and Adaptive-network-based fuzzy interference system (ANFIS). The models developed are used for nonlinear adaptive control, fault detection, diagnosis, forecasting, occupant behavior modeling, performance analysis, and knowledge extraction[47]. The drawback of FL models is that data and knowledge for the different components are often unavailable.

C. Statistical model

Statistical models are developed from large datasets by understanding particular trends. Examples of the available models from the literature include finite impulse response (FIR), output error (OE), single and multivariate regression, Box-Jenkins (BJ), autoregressive integrated moving average (ARIMA), autoregressive exogenous (ARX), and autoregressive moving average exogenous (ARMAX). The statistical models developed pose shortcomings such as low accuracy, inability to capture nonlinear dynamics, and large order and parameters[48].

D. State-space model

state-space model is crucial for control system design for a wide range of conditions. Relation between the input and the output states is given concerning HVAC parameters[29]. The drawback is that only a few works are presented on the state space model in the literature.

E. Geometric model

The model presents the HVAC system with the aid of two-dimensional (2D) and three-dimensional (3D) geometric shapes[45], [49]. The model technique is computationally penalized with large data sizes, and it is sensitive to noise. The application of geometric modeling is quite rare in HVAC systems.

F. Case-based reasoning (CBR)

CBR model is commonly used for ill-defined or non-linear systems, similar past cases as used, and the accuracy of prediction increases with time for future predictions for a given dataset[46], [50]. The topological CBR (TCBR) model is when a subset of the given dataset is used to develop the models, such models are used to monitor and analyze system performance [51], [52].

G. Stochastic model

Stochastic models are developed using a probability density (PDF) function to model random processes in HVAC systems. It is deployed in applications to understand occupant time schedules and activity levels. However, the models are mostly simulation-based based, and hardware validation is needed[51], [53].

H. Instantaneous model.

Instantaneous models comprise a statistical and pattern model known in the literature as Just in Time (JIT). HVAC components and thermal load models are developed from a large database.

III. Gray-box

The Gray-box model is a combination of white-box and black-box models, the idea is to address the shortcomings of both modeling approaches. The advantage of the gray-box model is its beneficial for control applications when presented as a state-space or transfer function [54]. Due to its relevance in control applications gray-box model will be developed in these and explained in detail in Chapter 3. Various shortcomings are highlighted in literature in the area of control techniques that are yet to be considered for implementation [55]

1.2 Heat Pump modeling techniques

The HVAC system contains three major components: the Heat pump (HP), the Air handling unit (AHU), and the cooling tower. A wide variety of modeling techniques are available in the literature for heat pumps. The models can be distributed into three classes depending on the uses: Calculation method, Dynamical system Behavior, and Heat pump design [56], [57]

The calculation methods are used for seasonal performance factors either for comparison between different types of HPs (product comparison) or individual building technology.

Product comparison: A simple equation with a set of conditions and boundaries provides a standard rating (e.g., seasonal coefficient of performance). In Europe, the SIST EN 14825:2019 standard is enlisted and sets the guidelines for the calculation of seasonal energy efficiency (SEER), seasonal space cooling energy efficiency, SCOP and seasonal space heating energy efficiency, and seasonal energy performance ratio (SEPR).

Comparison of individual building technology: the individual building technologies are governed by EN 15316-4-2:2017 standard to set up guidelines for calculation values of system energy requirement and system energy efficiencies.

Dynamical system simulations are used to depict system behavior over a short or long period and achieve a control action. An empirical approximation can predict the energy cost of a given building and energy use given the hourly weather information by using a curve fitting[58].

Performance map model: Quasi-static models are mostly used in dynamic simulation programs to model heat pumps (e.g., TRNSYS[59], ESP-r, Insel, EnergyPlu, MATLAB/Simulink[60]). A finite point of data is provided, and curve-fitting techniques can be used to interpolate the overall model to obtain heating and cooling capacity and electrical demand. Due to the fact of extrapolating the user must pay attention to the output data of the model as frosting may be an issue[61].

Heat pump design models are composed of the most complex form of modeling at HP. A strong theoretical background is essential to derive a model of all the known components. This particular approach requires computing the refrigerant cycle and operational condition of individual components. *Refrigerant cycle models* aim to improve and optimize the components of an HP in the refrigeration cycles shown in. This model is also a quasi-static model of each of the components rather than the entire HP as shown in the performance map model. This detailed approach will require specific measurements or catalog data to model the overall HP system and the targeted component to be optimized is improved via a design or control method.

1.3 Electrical Motors used in HPs.

A compressor, in an HP system, is considered the active component since it contributes maximum towards the energy consumption. Many advancements have been accomplished in the control of Alternation Current (AC) Machines with immense contributions towards reducing energy consumption. It is vital to use a suitable AC machine for an appropriate high-speed application: Commonly used electrical motors for HP systems comprise Induction Motors (IM), Permanent Magnet Synchronous motors (PMSM), and Switched Reluctance Motors (SRM). The characteristics of each motor are described:

I. Induction motor

IMs have been used as a constant speed with a non-inverter configuration in the global market. An on-off control cycle has been adopted to maintain a set-point temperature with the IM directly connected to the local grid[62], [63]. VFD with IM has been used in electrical vehicle

applications[64], [65], household refrigeration[66], and HVAC applications [67]. The advantages of using an IM are its simplicity in construction, high robustness, and low cost.

II. Permanent Magnet Synchronous Motor

PMSM is considered a successor of the traditionally used IM in many industry applications, due to its high efficiency, simple excitation, low noise, and output power density[68], [69], [70]. PMSMs can be categorized into two sub-classes (interior or surface), depending on the placement of the permanent magnets. Disadvantages of using a PMSM can be the high cost, increasing volume, and inertia[69].

III. Switched Reluctance Motor

SRM is regarded as the successor of PMSM because of the low manufacturing cost, insensitivity to high temperature, high reliability, and high-speed capability[71], [72]. Disadvantages of SRM are more torque ripple and high noise[70], [73].

The user-dependent factors with redesign and improvements may contribute towards reducing energy consumption. However, both factors require either a very well-educated and aware public to minimize the cooling load or immense dedication to redesign and improvement at ground level on existing components by leading experts. These factors will require a significant amount of finance to be achieved and implemented.

Each type of motor packs a set of advantages and disadvantages as mentioned above. The induction motor will be used due to its low cost and high robustness nature which makes IMs suitable for a VFD coupled with a compressor for cooling applications. The state-space model of IM (Chapter 2) and a dynamic heat pump model (Chapter 3) will be presented. The aim is to improve the performance of a traditionally used induction motor VFD by enhancing the control technique to improve system performance. This moves the focus towards improvements attained from adopting an optimal control approach for HPs.

1.4 Control of Heat Pumps

Control is a vital aspect of the overall performance of an HVAC system. Literature gives insight into the control of various components in an HVAC system. i.e. Control of Pumps[74], [75], Compressors[74] and expansion valves[76], [77], [78], [79], [80]. The focus of this thesis is on the control of the compressor. Control techniques that have been deployed in recent studies to compressors in HPs include constant-speed and Variable-speed drive [81], [82].

I. Constant Speed (Start/stop) control.

Constant speed control is also referred to as Start/stop control. Initially, the heat pump was made up of only constant-speed motors. i.e. generally used in small-scale compressor systems with an on-and-off strategy to maintain a desired set point with a constant duty cycle and speed [83], [84]. It is important to highlight that capacity control is achieved for constant speed HP via two possibilities: ON-OFF capacity control using a single or mono-compressor or multi-compressor. The control of a compressor is dependent on the monitoring variable, in most cases, water return and supply temperatures are considered. The logic of a Start/stop or on/off strategy for cooling and heating is shown in Fig.3. a. and Fig.3. b. respectively. The controllers are used in a simple hysteresis comparator with a given dead band value. The dead band value is the temperature ranges between each on-off sequence as shown in Fig.3.a and b a $2^{o}C$ range is set for both the operating conditions. The dead band and set point are generally determined by the manufacturer or user depending on the need at hand.

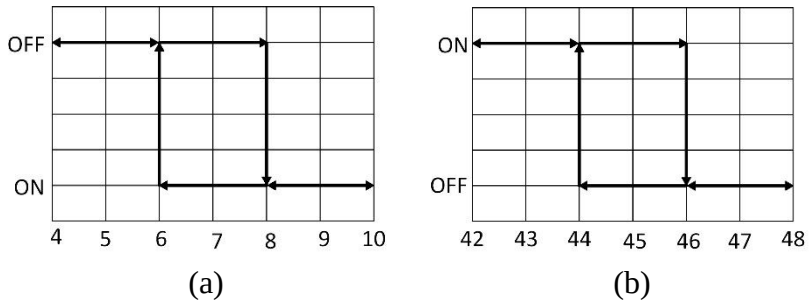

Figure 3 Start/stop control behavior of compressor for: (a) cooling mode (b) Heating mode

Such control techniques are valid only for a single-stage HP i.e. only a single HP is used to control the thermal capacity. However, for a multi-stage HP, the number of compressors available is more than one, hence depending on the thermal capacity of each compressor, it is modulated or sequenced on and off to deliver the required thermal capacity. The control strategy for a multi-stage HP is shown in Fig. 4. a. and 4. b. for cooling and heating model operation for a dual compressor set-up.

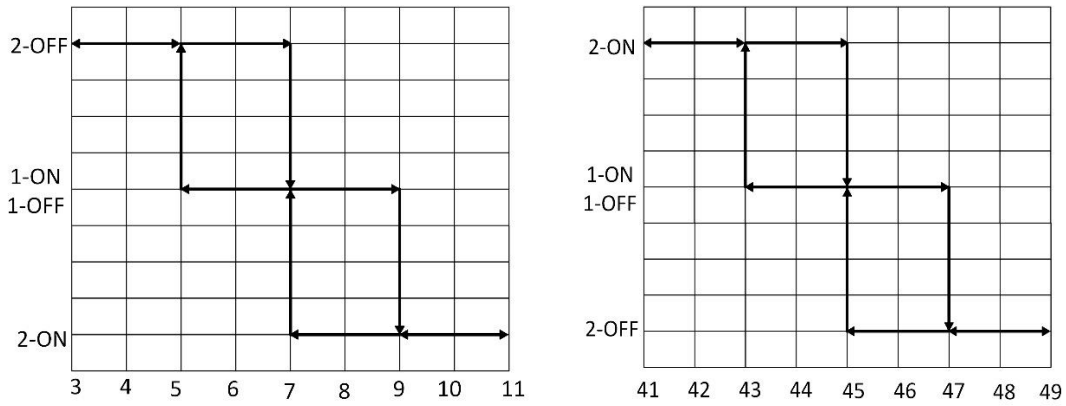

(a) (b)

Figure 4 Start/stop control behavior of dual compressor for (a) cooling mode and (b) Heating mode

The hysteresis logic to control a dual compressor system for heating and cooling mode operation is resented with the set point at 7^{o}C and 45^{o}C. Such control techniques are widely used for small, medium, and large applications. This particular control technique tends to be uneconomical in terms of energy consumption and water consumption[85]. Plume control is used for hot water systems that consist of solar collectors in sub-tropic regions[86]. However, recent technological advancements have introduced inverter-driven HPs controlled at variable speeds and it is important to understand its operation.

II. Variable speed control (VSC)

VSC is the most likely solution for small-scale applications, with an inverter-driven heat pump and a single compressor used. Due to the variable speed operation, the compressor can provide a thermal capacity of up to 20% of the rated capacity. An alternating current (AC) supply motor is used, the variable speed control depends on the supply frequency of the motor and, to achieve variable speed control a variable drive is essential[87]. Control techniques such as Field-oriented control or Scalar control are necessary. The maintain the thermal capacity at a set temperature Proportional integrator controller is used. For instance, Bechtel et al. [36] used model predictive control to optimize HP operation while considering variable electricity prices. Ding et al. [37] proposed an optimization approach to operating the HPs and the heating system for an office building in case of demand response provision including building load uncertainty by using a quantile regression neural network. The results showed a 35.8% reduction in operating costs compared with the conventional robust optimal operating strategy. Abookersh et al. [38] compared two control strategies for the flexible operation of HPs coupled to seasonal storage in a low-

temperature district heating network. Montrose et al. [39] proposed an optimal control algorithm, which aimed at minimizing the overall power consumption of variable-speed HPs by regulating the indoor temperature setpoint through peer-to-peer communication. Lee et al. [40] proposed an operation strategy for variable-speed HP based on mixed-integer model predictive control. The model allowed not only to prevent the operation of the HP with lots of compressor cycling but also to predict future heat load and ambient air temperatures. Results showed a maximum 22% reduction in electricity cost and carbon emissions. Dengiz et al. [41] proposed a heuristic control for the flexible operation of HPs coupled with a photovoltaic supplying underfloor heating system and a domestic hot water tank. The authors found a maximum 13.3% reduction in operating cost compared to a conventional control strategy and a 52.6% reduction in the surplus of energy produced onsite. Maier et al. [21] found that HP management through model predictive control outperforms operating strategies based on heating curves. Baeten et al. [42] propose a multi-objective model predictive control for residential heat pumps for promoting a flexible operation. Results indicated the capability of the controller to shift peak load. However, the authors stressed that in case of demand response need, heat pump owners should be encouraged to participate by remunerating them for their additional expenses. Efkarpidis et al. [43] proposed an optimization method to operate heat pumps along with solar thermal collectors, batteries, and thermal energy storage aiming at maximizing self-consumption. Arteconi and Polonara [44] developed an HP control based on electricity price which varied HP's temperature set point based on the variation of electricity market price. The study revealed that a substantial decrease in peak demand could be achieved. Schibuola et al. [45] compared operating strategies for DR for an HP-coupled photovoltaic system. Some studies have investigated the capability of HPs to support transmission and system operators by providing ancillary services. Meesenburg et al. [46] found that large two-stage ammonia HPs can provide ancillary services thanks to their capability to quickly vary the electrical energy consumed. More specifically, the authors estimated that the HP's power input could be varied by about 50% in 85 s while maintaining a safe compressor's operation. Regarding HPs in the residential sector, Manner et al. [47] found that the aggregation of residential HPs could guarantee valid support for ancillary services. However, the authors stressed the importance of developing a real-time control system to manage the whole aggregated system. Rodriguez et al. [48]developed and validated a model for managing a cluster of residential HPs in the case of frequency regulation. The model revealed that the DR potential of aggregated HPs is significant,

but particular attention needs to be given to the number of activation times of HPs, and most importantly to the duration. Bartolucci et al. [49] showed that worthy cost savings could be achieved by the provision of ancillary services via large HPs coupled with thermal storage.

Gap Analysis

The previous literature review has shown a strong research interest in modeling HP behavior (as demonstrated by the large use of machine learning techniques or from research on frost buildup and removal) or improving performance during operation by advanced supervisory controllers. However, regardless of the purposes, integrated thermodynamic and control modeling has never been performed. More specifically, regarding thermodynamic modeling, the performance variation due to time-changing boundary conditions (e.g., the outdoor temperature) or the part-load operation is typically estimated using catalogs' data corrected by empirical factors [23], [88]. In addition, the control strategy adopted to meet the user's heating demand (and then the dynamic response) is not accounted for [89], [90]. Finally, other studies focused on the development of refined HPs' control strategies for the provision of DR but using very simplified thermodynamic modeling [88], [91], [92]. Considering the novel applications of HPs, it is of paramount importance to rely on a detailed thermodynamic and control model. In this respect, some papers have pointed out that issues could arise when HPs are used to provide flexibility, which cannot be detected by relying on very simplified models. For instance, Liu et al. [93] pointed out that drastic changes in the compressor speed due to load balancing can lead to wet compression and then to compressor damage. Clauß and Georges [94] underlined that in short-time operation the transient effects of the HP, such as cycling losses during start-up, are important. Bagarella et al. [95] found via experiments that cycling losses due to ON-OFF control could reduce the performance by up to 13% compared to a steady-state operation.

In this framework, the provision of modeling on a detailed thermodynamic modeling and the embedded architecture control is of paramount importance to achieve more reliable results. More specifically, the developed models should provide insights into (i) the ability of the RHP to quickly respond to the variation in the cooling and heating demand of the users (e.g., buildings); (ii) the capability to adapt to the variation in the local while accounting for limits of the electric motor and the embedded controller, and (iii) the possibility to compare new control strategies aimed at

improving the overall energy performance. The thesis compared different controls (e.g., proportional-integral for variable speed, and hysteresis controller for sequential control.) and they demonstrated that the modeling complexity of the system control has a significant impact on the key performance indicators, proving that this aspect should not be overlooked. For instance, for short-term operation, the modeling of the heat pump controller and the transient effects of the heat pump, such as cycling losses during start-up, are important.

Chapter 2

Machine modeling

Objectives:

- Present the steady-state model of an Induction motor.
- Give a detailed methodology for obtaining the parameters
- Present the state-space model

The chapter explores the extensive domain of induction machine modeling, encompassing both dynamic and steady-state models across references. It elaborates on the differential equations governing the electromagnetic interactions within both the stator and rotor, as well as the equation governing motion. These equations are formulated using the space-vector theory, under the same foundational assumptions. While applicable to any three-phase AC machine, the focus here primarily is on induction motors. The chapter presents formulations in the stator reference frame, the rotor reference frame, and a generalized reference frame. This generalized framework enables representation in the stator flux-linkage reference frame, the rotor flux-linkage reference frame, and the magnetizing flux-linkage reference frame.

2.1 Steady-State Modeling

The concept of open-loop voltage/frequency (V/f) control (scalar control) has been extensively documented in various papers within the literature [96], [97]. To maintain coherence, the fundamental idea is outlined here. Fig. 5. illustrates the steady-state per-phase equivalent circuit of a symmetrical three-phase operation induction machine.

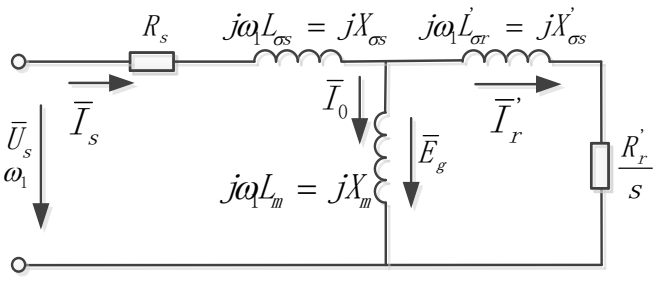

Figure 5Steady-State per-phase equivalent circuits of IM

USE THE VOLTAGES WITH TIPS ON THE OTHER SIDE (European convention)

Where:

- -$\bar{U}_s, \bar{E}_g$ are the phasors of supply voltage, air gap voltage respectively,
- -$\bar{I}_s, \bar{I}_o, \bar{I}'_r$ are the phasors of stator, mutual, rotor current,
- -R_s, R_r, $L_{\sigma s}$, $L_{\sigma r}$, are the resistance, leakage inductance of stator and rotor,
- $X_{\sigma s}$, $X_{\sigma r}$ are the stator and rotor reactance,
- $\boldsymbol{\omega_1}$ represents the supply frequency in electrical *rad/s*,
- s=slip,

where the ' refers to stator, taking the steady-state space-vector equations of the IM, the air-gap electromagnetic torque is related to the mechanical power and air-gap power as:

$$T_e = \frac{P_m}{\omega_m} = \frac{P_{gap}(1-s)}{\omega_1(1-s)} = 3\frac{\left|I_r'^2\right|R_r'}{\omega_1 s} \qquad 2.1$$

Where P_m and P_{gap} are the mechanical and air gap power, and ω_m is the rotor mechanical speed (in electrical radians).

The current can be obtained from Fig. 5 as

$$\bar{I}_r' = \frac{\bar{U}_s}{(1+\sigma_s)\left\{R_s + R_r'/s + j\left[X_{\sigma s}/(1+\sigma_s) + X'_{\sigma r}\right]\right\}} \qquad 2.2$$

Where: $\sigma_s = \dfrac{X_{\sigma s}}{X_m}$ is the stator leakage factor.

Thus, by substitution of eqn. 2.2 into eqn. 2.1, the electromagnetic torque can be presented in terms of the IM parameters as,

$$T_e = \frac{3}{\omega_1} \frac{\left|\overline{U}_s\right|^2}{(1+\sigma_s)^2} \frac{R_r^{'}/s}{(R_s + R_r^{'}/s)^2 + X^{'2}} \qquad 2.3$$

Where:

$$X^{'} = X_{\sigma r}^{'} + \frac{X_{\sigma s}}{1+\sigma_s} \qquad 2.4$$

X' is the transient rotor reactance of the induction machine.

It follows from 2.3, that by assuming the machine parameters constant, the electromagnetic torque is proportional to the square amplitude of the stator voltage for a given slip. By equaling the first derivative of 2.3 with respect to the slip to zero, $dT_e/ds = 0$, the critical slip (breakdown slip) is given by:

$$s_{\max} = \frac{\pm R_r^{'}}{(R_s^2 + X^{'2})^{1/2}} \qquad 2.5$$

This slip corresponds to the maximum torque given by:

$$T_{e\max} = \frac{\frac{3}{\omega_1}\left(\frac{U_s}{1+\sigma}\right)^2}{2\left[R_s \pm (R_s^2 + X^{'2})^{1/2}\right]} \qquad 2.6$$

Within eqn. 2.5 and 2.6, the 'positive' corresponds to the maximum motoring torque, which is also referred to as breakdown torque, and the 'negative' is referred to as maximum generated torque. It can be observed that the maximum torque is directly proportional to the stator voltage value squared and it is inversely proportional to the transient rotor reactance $X^{'}$ of the IM. Considering only the motor mode, it follows from eqn. 2.3 and 2.6 that the ratio of the breakdown torque and the torque can be expressed as:

$$\frac{T_e}{T_{e\max}} = \frac{2(1+k)}{(s/s_{\max} + s_{\max}/s + 2k)} \cong \frac{2}{s/s_{\max} + s_{\max}/s} \qquad 2.7$$

Where:

$$k = \frac{R_s}{(R_s^2 + X'^2)^{1/2}} \approx 0 \qquad 2.8$$

Equation 2.7 indicates that the steady-state torque, for the same value of the voltage and supply frequency, depends only on the slip; this relationship is almost linear for smaller values, where speed is almost equal to the synchronous speed. We can say that:,

$$T_e \cong 2\frac{T_{e\max p}}{s_{\max}} s \qquad 2.9$$

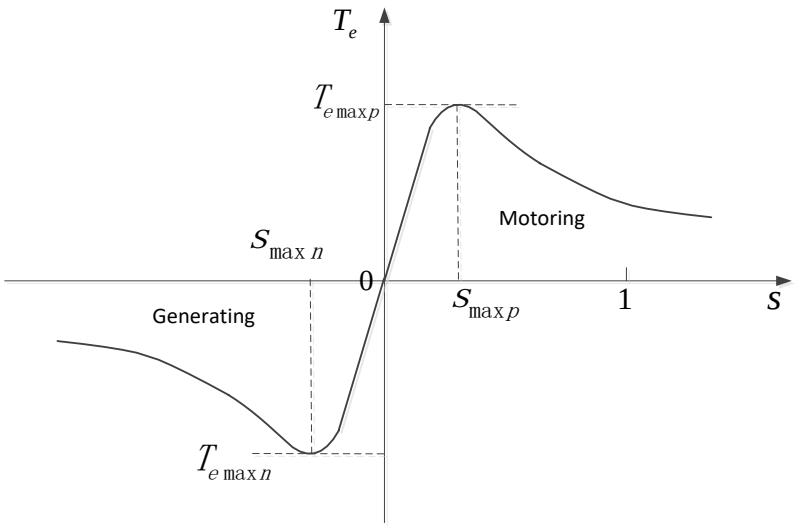

Figure 6 Torque-slip characteristic of an IM at steady-state operation

Fig. 6 shows a typical torque-slip curve of IM in steady state for negative and positive values of slip. On the other hand, the flux linkage of an IM is linked to the air gap voltage as:

$$\overline{\psi}_m = \frac{\overline{E}_g}{j\omega_1} \qquad 2.10$$

The flux linkage can be maintained constant by keeping the ratio between air gap voltage and supply angular frequency constant. The rotor current can be rewritten from fig. 5 as a function of $\bar{E}_g$

$$\bar{I}_r^{'} = \frac{\bar{E}_g}{\frac{R_r^{'}}{s} + jX_{\sigma r}^{'}} \tag{2.11}$$

Meanwhile, the expression for torque for a constant $\bar{\psi}_m$, can be rewritten as:

$$T_{eE_g/f} = \frac{3}{\omega_1} \cdot \frac{\bar{E}_g^2}{\left(\frac{R_r^{'}}{s}\right)^2 + X_{\sigma r}^{'\,2}} \cdot \frac{R_r^{'}}{s} = 3(\psi_m)^2 \frac{s\omega_1 R_r^{'}}{R_r^{'2} + s^2\omega_1^2 L_{lr}^{'2}} \tag{2.12}$$

Where the subscript E_g/f omlpies that the constant flux linkage at eqn2.12. The slip at maximum torque can be given following the same procedure as (2.5)

$$s_{\max E_g/f} = \frac{\pm R_r^{'}}{\omega_1 L_{lr}^{'}} \tag{2.13}$$

And the maximum torque is equal to:

$$\mathrm{T_{emax\,E_g/f}} = \frac{3}{2}\left(\frac{\bar{\mathrm{E}}_s}{\omega_1}\right)^2 \frac{1}{\mathrm{L_{lr}^{'}}} \tag{2.14}$$

A revised version of equation (2.9) under constant $\bar{\psi}_m$ at a speed close to the synchronous speed yields:

$$T_{eE_g/f} \cong 2\frac{T_{e\max}}{s_{\max}} s = \frac{3}{2}\frac{|\bar{\psi}_m|^2}{R_r^{'}} s \tag{2.15}$$

Equation (2.14) shows that the maximum torque is only dependent of the ratio E_g/f , and hence remains the same for constant E_g/f. Fig.7 displays a series of steady-state torque-speed characteristics for an induction motor operating under constant flux linkage. The parameters pertinent to this motor are detailed in Chapter 6. This illustration distinctly indicates that as the supply frequency increases, so does the synchronous speed of the motor. Furthermore, at a lower supply frequency, the starting torque increases, provided the maximum torque remains consistent. Notably, the maximum torque remains nearly unchanged despite fluctuations in frequency.

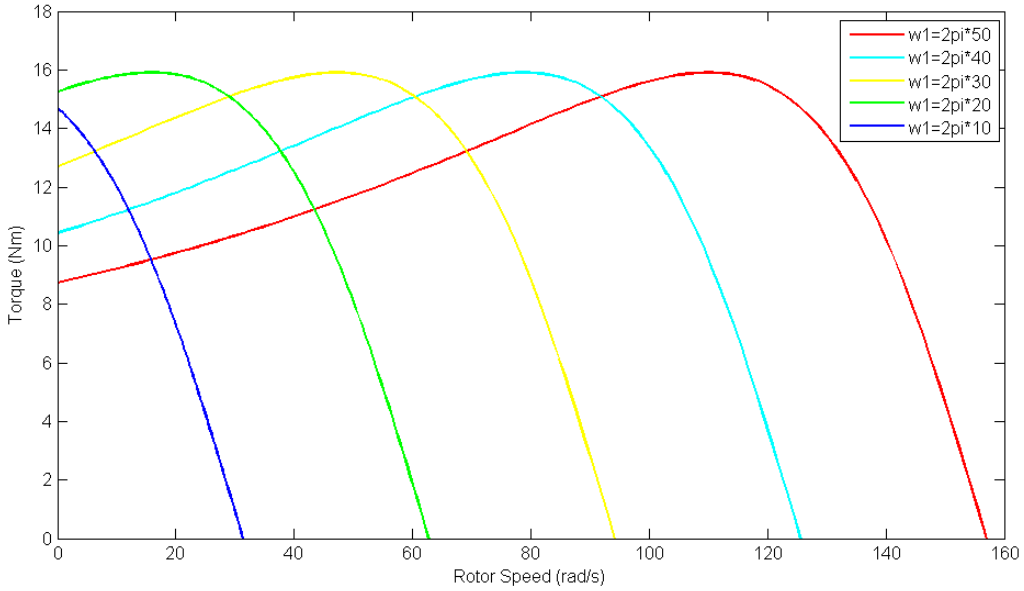

Figure 7.a Torque-speed characteristic of an IM under constant Eg/f

2.2 Definition of the machine space-vector quantities

Consider a three-phase electrical machine characterized by a cylindrical structure, a smooth air gap, and a single pole pair, featuring three-phase windings on both the stator and the rotor. The cross-sectional surface of this configuration is depicted in Figure 7.b. The following assumptions are applied:

- Infinite permeability of iron.
- Flux density in the air gap is oriented radially.
- Neglect the stator and rotor slotting effects.
- Neglect the stator and rotor losses.
- Each stator and rotor three-phase winding is treated as a full-pitch multi-turn winding.
- The axes of each stator three-phase winding (s_A, s_B, s_C) are spatially displaced by an angle of $2\pi/3$ from each other around the stator periphery.
- The axes of each rotor three-phase winding (r_a, r_b, r_c) are spatially displaced by an angle of $2\pi/3$ from each other around the rotor periphery. The electrical angle between the axis of the rotor a phase (r_a) and the stator A phase (s_A) is denoted as θ_r, and the rotor speed in electrical radians per second is expressed as $\omega_r = d\theta_r/dt$.

Absence of zero-sequence stator current, such as when the neutral point of the stator three-phase system is isolated.

$$i_{sA}(t) + i_{sB}(t) + i_{sC}(t) = 0 \qquad (2.15)$$

where t is the time variable and $i_{sA}(t)$, $i_{sB}(t)$, $i_{sC}(t)$ are the instantaneous values of the stator currents for each stator phase. Under these assumptions, the time and space waveform $f_s(\theta,t)$ of the resultant total mmf, (magneto-motive force) caused by the three stator phases, can be expressed as [2.16]:

$$f_s(\theta,t) = N_{se}\left[i_{sA}(t)\cos(\theta) + i_{sB}(t)\cos(\theta - 2\pi/3) + i_{sC}\cos(\theta - 4\pi/3)\right] \qquad (2.16)$$

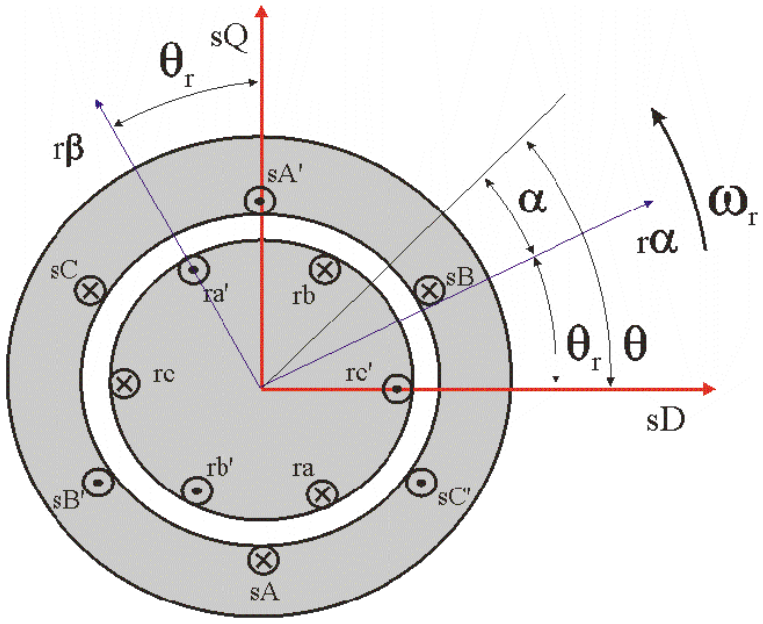

Figure 7.b Cross section of a three-phase machine

where θ is the electrical angle coordinate along the stator periphery from the "sD" axis, coincident with the axis of phase s_A (Fig.7.b), and N_{se} is the number of effective turns of each stator winding (given by the number of turns N_s multiplied by the winding factor k_{ws} of the stator winding). If complex numbers are used, (2.16) can be re-written as:

$$f_s(\theta,t) = \frac{3}{2} N_{se}\,\mathrm{Re}\left\{\frac{2}{3}\left[i_{sA}(t) + a\, i_{sB}(t) + a^2\, i_{sC}(t)\right]e^{-j\theta}\right\} \qquad (2.17)$$

Where Re means "real part", j is the imaginary unit and $a=e^{j2\pi/3}$ is a complex operator that makes a vector rotate of $2\pi/3$ rad. From (2.17) it is possible to define the stator current space-vector in the stationary reference frame, coincident with the stator reference frame "sD-sQ", as follows:

$$\mathbf{i_s}(t)=\frac{2}{3}\left[i_{sA}(t)+a\,i_{sB}(t)+a^2\,i_{sC}(t)\right]=|\mathbf{i_s}|e^{j\alpha_s}=i_{sD}(t)+j\,i_{sQ}(t) \tag{2.18a}$$

where $|\mathbf{i_s}|$ is the amplitude of the stator current space-vector, α_s is the angle of the stator current space-vector from the sD axis, $i_{sD}(t)$ and $i_{sQ}(t)$ are respectively the instantaneous values of the sD and sQ components of the stator current space-vector. It should be however remarked that $i_{sD}(t)$ and $i_{sQ}(t)$ can be directly computed from the phase variables by the so-called two-axis Park transformation (also called $3\rightarrow 2$ transformation), given by:

$$\begin{cases} i_{sD}=\dfrac{2}{3}\left(i_{sA}-\dfrac{1}{2}i_{sB}-\dfrac{1}{2}i_{sC}\right) \\ i_{sQ}=\dfrac{1}{\sqrt{3}}\left(i_{sB}-i_{sC}\right) \end{cases} \tag{2.18b}$$

It should be emphasized that, since the current are time-varying, also the amplitude and the angle of the stator current space-vector are time-varying. The stator current space-vector then encompasses, thanks to its complex representation, the instantaneous amplitude and angle of the sinusoidal mmf distribution produced by the three stator currents. The above considerations permit the definition of the stator mmf space-vector as:

$$\mathbf{f}_s(t)=N_{se}\mathbf{i_s}(t) \tag{2.19}$$

By analogy with the stator currents and mmf, the rotor current space-vector and the rotor mmf space-vector can be defined in a similar way. Actually if $i_{ra}(t)$, $i_{rb}(t)$, $i_{rc}(t)$ are the instantaneous values of the rotor currents in the three rotor phases and if N_{re} is the number of effective turns of each rotor winding (given by the number of turns N_r multiplied by the winding factor k_{wr} of the rotor winding), under the assumption that there are no zero-sequence rotor currents, the space and time mmf distribution produced by the rotor currents is given by:

$$f_r(\theta,t)=N_{re}\left[i_{ra}(t)\cos(\alpha)+i_{rb}(t)\cos(\alpha-2\pi/3)+i_{rc}\cos(\alpha-4\pi/3)\right] \tag{2.20}$$

where α, which is a function of the angle θ, is the electrical angle coordinate along the rotor periphery from the "rα" axis, coincident with the axis of phase "ra" (Fig. 4.1). If complex numbers are used, (2.20) can be re-written as:

$$f_r(\theta,t) = \frac{3}{2} N_{re} \,\mathrm{Re}\left\{\frac{2}{3}\left[i_{ra}(t) + a\, i_{rb}(t) + a^2\, i_{rc}\right] e^{-j\alpha}\right\} \tag{2.21}$$

It is possible to define the rotor current space-vector in the rotor reference frame, coincident with the reference frame "rα-rβ", as:

$$\mathbf{i}_r(t) = \frac{2}{3}\left[i_{ra}(t) + a\, i_{rb}(t) + a^2\, i_{rc}(t)\right] = |\mathbf{i}_r| e^{j\alpha_r} = i_{r\alpha}(t) + j\, i_{r\beta}(t) \tag{2.22}$$

where $|\mathbf{i}_r|$ is the amplitude of the rotor current space vector, α_r is the angle of the rotor current space vector from the rα axis, $i_{r\alpha}(t)$ and $i_{r\beta}(t)$ are respectively the instantaneous values of the rα and rβ components of the rotor current space-vector. With a rotational transformation of θ_r the rotor current space vector can be expressed in the stationary reference frame as follows:

$$\mathbf{i}_\mathbf{r}^{'}(t) = \mathbf{i}_\mathbf{r}(t) e^{j\theta_r} = |\mathbf{i}_\mathbf{r}| e^{j(\theta_r+\alpha_r)} = |\mathbf{i}_\mathbf{r}| e^{j\alpha_r^{'}} = i_{rd}(t) + j\, i_{rq}(t) \tag{2.23}$$

Where $\alpha'_r = \alpha_r + \theta_r$ is the angle of the rotor current space-vector from the direct sD axis of the stationary reference frame and $i_{rd}(t)$ e $i_{rq}(t)$ are respectively the instantaneous sD and sQ components of the rotor current space in the stationary reference frame. The rotor mmf space-vector can be likewise defined as:

$$\mathbf{f}_\mathbf{r}(t) = N_{re}\mathbf{i}_\mathbf{r}(t) \tag{2.24}$$

In the same way, the stator flux linkage space-vector and the rotor flux linkage space-vector can be defined. Particularly the stator flux linkage space vector is defined from the instantaneous value of the total flux linkage in the stator phases sA, sB, sC, i.e. $\psi_{sA}(t)$, $\psi_{sB}(t)$, $\psi_{sC}(t)$ in the stationary reference frame, as follows:

$$\boldsymbol{\psi}_\mathbf{s} = \frac{2}{3}\left(\psi_{sA}(t) + a\,\psi_{sB}(t) + a^2\,\psi_{sC}(t)\right) \tag{2.25}$$

The total flux linkage in the stator phases due to the combined effect of stator and rotor currents is given by the following relationships:

$$\begin{cases} \psi_{sA} = \bar{L}_s i_{sA} + \bar{M}_s i_{sB} + \bar{M}_s i_{sC} + \\ \quad + \bar{M}_{sr} \cos\theta_r \; i_{ra} + \bar{M}_{sr} \cos(\theta_r + 2\pi/3)\, i_{rb} + \bar{M}_{sr} \cos(\theta_r + 4\pi/3)\, i_{rc}; \\ \psi_{sB} = \bar{L}_s i_{sB} + \bar{M}_s i_{sA} + \bar{M}_s i_{sC} + \\ \quad + \bar{M}_{sr} \cos(\theta_r + 4\pi/3)\, i_{ra} + \bar{M}_{sr} \cos\theta_r \; i_{rb} + \bar{M}_{sr} \cos(\theta_r + 2\pi/3)\, i_{rc}; \\ \psi_{sC} = \bar{L}_s i_{sC} + \bar{M}_s i_{sB} + \bar{M}_s i_{sA} + \\ \quad + \bar{M}_{sr} \cos(\theta_r + 2\pi/3)\, i_{ra} + \bar{M}_{sr} \cos(\theta_r + 4\pi/3)\, i_{rb} + \bar{M}_{sr} \cos\theta_r \; i_{rc}; \end{cases} \qquad (2.26 \text{ a, b, c})$$

where $\bar{L}_s$ is the self-inductance of each stator phase (assumed equal for each phase for symmetry reasons), $\bar{M}_s$ is the mutual inductance between one stator winding and one of the other two stator windings (also, in this case, assumed equal for each phase for symmetry reasons), and $\bar{M}_{sr}$ is the maximum value of the mutual inductance between the stator and the rotor windings. Due to symmetry reasons, this value is constant whatever stator and rotor winding is considered. However the mutual inductance between the stator and the rotor windings varies with the rotor angle. By using (2.26 a, b, c) and (2.25) and some algebra, the stator flux linkage space-vector can be expressed as a function of the stator current space-vector and the rotor current space-vector in the stator reference frame:

$$\boldsymbol{\psi}_{\mathbf{s}} = L_s \mathbf{i}_{\mathbf{s}} + L_m \mathbf{i}_{\mathbf{r}}' = L_s \mathbf{i}_{\mathbf{s}} + L_m \mathbf{i}_{\mathbf{r}} \; e^{j\theta_r} = \psi_{sD}(t) + j\, \psi_{sQ}(t) \qquad (2.27)$$

where $L_s = \bar{L}_s - \bar{M}_s$ is the total three-phase stator self-inductance, $L_m = 3/2\, \bar{M}_{sr}$ is the three-phase magnetizing inductance, $\psi_{sD}(t)$ and $\psi_{sQ}(t)$ are respectively the instantaneous values of the sD and sQ components of the stator flux linkage space-vector. Eq.(2.27) shows that the stator flux linkage is made up of two terms: one is the stator self-flux linkage $L_s \mathbf{i}_{\mathbf{s}}$ due only to the stator currents, and the other is the mutual flux component $L_m \mathbf{i}_{\mathbf{r}}'$ due only to the rotor currents which link the stator winding.

Likewise the rotor flux linkage space-vector is defined from the instantaneous value of the total flux linkage in the rotor phases r_a, r_b, r_c, i.e.$\psi_{ra}(t)$, $\psi_{rb}(t)$, $\psi_{rc}(t)$, in the rotor reference frame as follows:

$$\boldsymbol{\psi}_r = \frac{2}{3}\left(\psi_{ra}(t) + a\, \psi_{rb}(t) + a^2\, \psi_{rc}(t)\right) \qquad (2.28)$$

Also in this case the total flux linkage in the rotor phases due to the combined effect of stator and rotor currents is given by the following relationships:

$$\begin{cases} \psi_{ra} = \overline{L}_r i_{ra} + \overline{M}_r i_{rb} + \overline{M}_r i_{rc} + \\ \quad + \overline{M}_{sr} \cos\theta_r \; i_{sA} + \overline{M}_{sr} \cos(\theta_r + 4\pi/3)\, i_{sB} + \overline{M}_{sr} \cos(\theta_r + 2\pi/3)\, i_{sC}; \\ \psi_{rb} = \overline{L}_r i_{rb} + \overline{M}_r i_{ra} + \overline{M}_r i_{rc} + \\ \quad + \overline{M}_{sr} \cos(\theta_r + 2\pi/3)\, i_{sA} + \overline{M}_{sr} \cos\theta_r \; i_{sB} + \overline{M}_{sr} \cos(\theta_r + 4\pi/3)\, i_{sC}; \\ \psi_{rc} = \overline{L}_r i_{rc} + \overline{M}_r i_{ra} + \overline{M}_r i_{rb} + \\ \quad + \overline{M}_{sr} \cos(\theta_r + 4\pi/3)\, i_{sA} + \overline{M}_{sr} \cos(\theta_r + 2\pi/3)\, i_{sB} + \overline{M}_{sr} \cos\theta_r \; i_{sC}; \end{cases} \qquad \begin{matrix} (2.29. \\ \text{a,b,c}) \end{matrix}$$

where $\overline{L}_r$ is the self-inductance of each rotor phase (assumed equal for each phase for symmetry reasons), and $\overline{M}_r$ is the mutual inductance between one rotor winding and one of the other two rotor windings (also in this case assumed equal for each phase for symmetry reasons). By using (2.29 a, b, c) and (2.28) and some algebra, the rotor flux linkage space-vector can be expressed as a function of the stator current space-vector and the rotor current space-vector in the rotor reference frame:

$$\boldsymbol{\psi}_{\mathbf{r}} = L_r \mathbf{i}_r + L_m \mathbf{i}_s^{'} = L_r \mathbf{i}_r + L_m \mathbf{i}_s \; e^{-j\theta_r} = \psi_{r\alpha}(t) + j\, \psi_{r\beta}(t) \tag{2.30}$$

where $L_r = \overline{L}_r - \overline{M}_r$ is the total three-phase rotor self-inductance, $\mathbf{i}_{\mathbf{s}}^{'} = \mathbf{i}_{\mathbf{s}} \; e^{-j\theta_r}$ is the stator current space-vector in the rotor reference frame, $\psi_{r\alpha}(t)$ and $\psi_{r\beta}(t)$ are respectively the instantaneous values of the rα and rβ components of the rotor flux linkage space-vector.

The rotor flux linkage space-vector in the stator reference frame can be expressed by:

$$\boldsymbol{\psi}_{\mathbf{r}}^{'} = \boldsymbol{\psi}_{\mathbf{r}} \; e^{j\theta_r} = L_r \mathbf{i}_{\mathbf{r}}^{'} + L_m \mathbf{i}_{\mathbf{s}} = \psi_{rd}(t) + j\, \psi_{rq}(t) \tag{2.31}$$

Where $\psi_{rd}(t)$ and $\psi_{rq}(t)$ are respectively the instantaneous values of the s_D and s_Q components of the rotor flux linkage space-vector. Similarly to the above definition, the stator voltage space-vector and the rotor voltage space-vector can be introduced. Thus, in absence of zero-sequence stator voltages, the stator voltage space-vector in the stator reference frame is defined as:

$$\mathbf{u}_{\mathbf{s}} = \frac{2}{3}\left[u_{sA}(t) + a\, u_{sB}(t) + a^2\, u_{sC}(t)\right] = u_{sD}(t) + j\, u_{sQ}(t) \tag{2.32}$$

Where $u_{sA}(t)$, $u_{sB}(t)$, $u_{sC}(t)$ are the instantaneous values of the voltages in the stator phases s_A, s_B, s_C and $u_{sD}(t)$ and $u_{sQ}(t)$ are respectively the instantaneous values of the s_D and s_Q components of the stator voltage space-vector. Likewise, in absence of zero-sequence rotor voltages, the rotor voltage space-vector in the rotor reference frame is defined as:

$$\mathbf{u}_r = \frac{2}{3}\left[u_{ra}(t) + a\, u_{rb}(t) + a^2\, u_{rc}(t)\right] = u_{r\alpha}(t) + j\, u_{r\beta}(t) \tag{2.33}$$

Where $u_{ra}(t)$, $u_{rb}(t)$, $u_{rc}(t)$ are the instantaneous values of the voltages in the rotor phases r_a, r_b, r_c and $u_{r\alpha}(t)$ and $u_{r\beta}(t)$ are respectively the instantaneous values of the rα and rβ components of the rotor voltage space-vector. The rotor voltage space-vector in the stator reference frame is given by:

$$\mathbf{u}_\mathbf{r}^{'} = \mathbf{u}_\mathbf{r}\, e^{j\theta_r} = u_{rd}(t) + j\, u_{rq}(t) \tag{2.24}$$

where $u_{rd}(t)$ and $u_{rq}(t)$ are respectively the instantaneous values of the sD and sQ components of the rotor voltage space-vector.

2.3 Phase equations of the induction machine

In the stator reference frame, the equations describing the AC machine for each stator phase are:

$$\begin{cases} u_{sA}(t) = R_s i_{sA}(t) + \dfrac{d\psi_{sA}(t)}{dt}; \\ u_{sB}(t) = R_s i_{sB}(t) + \dfrac{d\psi_{sB}(t)}{dt}; \\ u_{sC}(t) = R_s i_{sC}(t) + \dfrac{d\psi_{sC}(t)}{dt}; \end{cases} \tag{2.35 a,b,c}$$

where R_s is the resistance of each stator winding and the stator flux-linkages ψ_{sA}, ψ_{sB}, ψ_{sC} are functions of stator and rotor currents (see eq.s 2.26 a, b, c). Similarly, in the rotor reference frame, the equations describing the AC machine for each stator phase are:

$$\begin{cases} u_{ra}(t) = R_r i_{ra}(t) + \dfrac{d\psi_{ra}(t)}{dt}; \\ u_{rb}(t) = R_r i_{rb}(t) + \dfrac{d\psi_{rb}(t)}{dt}; \\ u_{rc}(t) = R_r i_{rc}(t) + \dfrac{d\psi_{rc}(t)}{dt}; \end{cases} \tag{2.36. a,b,c}$$

Where R_r is the resistance of each rotor winding and the rotor flux-linkages ψ_{ra}, ψ_{rb} ψ_{rc} are functions of stator and rotor currents (see eq.s 2.29 a, b, c).

The equation of motion is given by:

$$t_e(t) - t_l(t) = J_m \frac{d\omega_{rm}(t)}{dt} + D\omega_{rm}(t) \tag{2.37}$$

where t_e is the electromagnetic torque, t_l the load torque, J_m is the inertia of the rotating masses, D is the damping constant which accounts for losses due to friction and windage, and ω_{rm} is the mechanical rotor speed expressed in mechanical angles.Eq (2.36 a, b, c) and (2.35 a, b, c) together with eq, (2.26 a, b, c) and (2.29 a, b, c) as well as the equation of the motion (2.37) constitute the so-called "phase-variable" dynamical mathematical model of the induction motor. In this model the input-output relationship between currents and voltages requires a matrix impedance of 36 terms, half of which are time-dependant because of the presence of cosine functions of the rotor position.

2.4 Space-vector equations in the stator reference frame

The differential equations (2.35. a, b, c) and (2.36 a, b, c) can be easily re-written by using the space-vector theory in the stator or stationary reference frame, which yields the following two equations, written for the stator and the rotor respectively:

$$\mathbf{u_s} = R_s \mathbf{i_s} + \frac{d\boldsymbol{\psi}_\mathbf{s}}{dt} \tag{2.38}$$

$$\mathbf{u_r'} = R_r \mathbf{i_r'} + \frac{d\boldsymbol{\psi}_\mathbf{r}'}{dt} - j\,\omega_r \boldsymbol{\psi}_\mathbf{r}' \tag{2.39}$$

The stator and rotor flux-linkages can be expressed as a function of the rotor and stator currents by using eq.s (2.27) and (2.31) re-written beneath for convenience:

$$\boldsymbol{\psi}_\mathbf{s} = L_s \mathbf{i_s} + L_m \mathbf{i_r'} = L_s \mathbf{i_s} + L_m \mathbf{i_r}\, e^{j\theta_r} = \psi_{sD}(t) + j\,\psi_{sQ}(t) \tag{2.40}$$

$$\boldsymbol{\psi}_\mathbf{r}' = \boldsymbol{\psi}_\mathbf{r}\, e^{j\theta_r} = L_r \mathbf{i_r'} + L_m \mathbf{i_s} = \psi_{rd}(t) + j\,\psi_{rq}(t) \tag{2.41}$$

By replacing the flux-linkages of (2.40) and (2.41) into (2.38) and (2.39) results in the differential equations relating rotor and stator voltage space-vectors to rotor and stator current space:

$$\mathbf{u_s} = R_s \mathbf{i_s} + \frac{d\left(L_s \mathbf{i_s}\right)}{dt} + \frac{d\left(L_m \mathbf{i_r'}\right)}{dt} \tag{2.42}$$

$$\mathbf{u_r'} = R_r \mathbf{i_r'} + \frac{d\left(L_r \mathbf{i_r'}\right)}{dt} + \frac{d\left(L_m \mathbf{i_s}\right)}{dt} - j\omega_r \left(L_r \mathbf{i_r'} + L_m \mathbf{i_s}\right) \tag{2.43}$$

The above two equations (2.42) and (2.43) together with the equation of the motion (2.37) constitute the dynamical model of the induction motor expressed with space-vectors in the stator reference frame. The electromagnetic torque t_e created by the induction motor can be written, by

using space-vectors in the stator reference frame, as a function of the stator (or rotor) flux-linkage and the rotor or stator current, or directly as a function of only the stator and rotor currents, as shown below:

$$t_e = -\frac{3pL_m}{2L_s}\boldsymbol{\psi}_\mathbf{s} \wedge \mathbf{i}_\mathbf{r}^{'} = \frac{3pL_m}{2L_r}\boldsymbol{\psi}_\mathbf{r}^{'} \wedge \mathbf{i}_\mathbf{s} = -\frac{3}{2}pL_m\mathbf{i}_\mathbf{s} \wedge \mathbf{i}_\mathbf{r}^{'} \tag{2.44}$$

where p is the number of pair poles of the machine and "$\wedge$" is the symbol of vector product for complex numbers.

2.5 State-Space Model of the Induction Machine

If the stator current and the rotor flux-linkage space vectors are chosen as state variables, the state equations of the induction machine in the stationary reference frame can be written as:

$$\frac{d}{dt}\begin{bmatrix}\mathbf{i}_\mathbf{s}\\ \boldsymbol{\psi}_\mathbf{r}^{'}\end{bmatrix} = \frac{d\mathbf{x}}{dt} = \begin{bmatrix}\mathbf{A_{11}} & \mathbf{A_{12}}\\ \mathbf{A_{21}} & \mathbf{A_{22}}\end{bmatrix}\begin{bmatrix}\mathbf{i}_\mathbf{s}\\ \boldsymbol{\psi}_r^{'}\end{bmatrix} + \begin{bmatrix}\mathbf{B_1}\\ \mathbf{0}\end{bmatrix}\mathbf{u}_\mathbf{s} = \mathbf{A}\,\mathbf{x} + \mathbf{B}\mathbf{u}_\mathbf{s} \tag{2.45 a}$$

$$\mathbf{i}_\mathbf{s} = \mathbf{C}\,\mathbf{x} \tag{2.45 b}$$

where:

$$\begin{cases} \mathbf{A_{11}} = -\{R_s/(\sigma L_s) + (1-\sigma)/(\sigma T_r)\}\mathbf{I} = a_{11} \\ \mathbf{A_{12}} = L_m/(\sigma L_s L_r)\{(1/T_r)\mathbf{I} - \omega_r\mathbf{J}\} = a_{12}\{(1/T_r)\mathbf{I} - \omega_r\mathbf{J}\} \\ \mathbf{A_{21}} = \{L_m/T_r\}\mathbf{I} = a_{21}\mathbf{I} \\ \mathbf{A_{22}} = -(1/T_r)\mathbf{I} + \omega_r\mathbf{J} = a_{22}\{(1/T_r)\mathbf{I} - \omega_r\mathbf{J}\} \\ \mathbf{B_1} = 1/(\sigma L_s)\mathbf{I} = b\,\mathbf{I} \end{cases} \tag{2.46 a,b,c,d,e}$$

with:

$\mathbf{i}_\mathbf{s} = \begin{bmatrix} i_{sD} & i_{sQ}\end{bmatrix}^T$, $\mathbf{u}_\mathbf{s} = \begin{bmatrix} u_{sD} & u_{sQ}\end{bmatrix}^T$, $\boldsymbol{\Psi}_\mathbf{r}^{'} = \begin{bmatrix}\Psi_{rd} & \Psi_{rq}\end{bmatrix}^T$, $\mathbf{C}^{'} = [\mathbf{0}\ \ \mathbf{I}]$, $\mathbf{C} = [\mathbf{I}\ \ \mathbf{0}]$, $\mathbf{I} = \begin{bmatrix}1 & 0\\ 0 & 1\end{bmatrix}$, $\mathbf{J} = \begin{bmatrix}0 & -1\\ 1 & 0\end{bmatrix}$.

In the above state representation $\mathbf{x} = \left[\mathbf{i}_\mathbf{s}, \boldsymbol{\psi}_r^{'}\right]$ is the state vector, comprised of the stator current and rotor flux linkage direct and quadrature components in the stationary reference frame, $\mathbf{u}_\mathbf{s}$ is the input vector composed of the stator voltage direct and quadrature components in the stationary reference frame, **A** is the state matrix (4x4 matrix) depending on the rotor speed ω_r, **B** is the input matrix and finally **C** is the output matrix. Refer to Appendix 3 to see the detailed computation of the motor parameters.

Summary:

Chapter 2 presents a full insight into induction motor drives. The steady-state model of an Induction motor and introduction to machine space vector quantites are also presented. The motor phase equationa are given with the state-space model of IM. A detailed methodology for obtaining the parameters of an IM is presented in appendix 3.

Chapter 3

Reversible heat pump modeling

Objectives:

- Model the heating and cooling modes of an RHP
- Implement the state-space model of the RHP

Recent technologies perform heating and cooling utilizing a reversible heat pump technology incorporating refrigerants and secondary fluid.

Basic refrigeration concepts that govern the Heating Ventilating and Air Conditioning (HVAC) system are covered in this chapter. The process of heating, cooling, humidifying, dehumidifying, and seasonal operation is covered. An insight into different refrigeration cycles is presented to introduce the topic. Heating is the gaining of heat or energy from the environment into a given space utilizing temperature differences. The process is maneuvered in various ways:

- Direct radiation
- Free convection
- Direct heating of air using forced circulation
- Indirect heating of air by transferring a secondary heated fluid (e.g. water)

The last point is of interest as the gain of temperature or heat in the air by the transfer of heated water is called sensible heat transfer. See chapter (4) to see the equation related to sensible heat transfer.

Humidification is the transfer or gain of water vapor to atmospheric air and the heat transfer is increased with the increasing ratio of water in the water-air concentration. The gain of temperature or heat by water is called Latent heat Transfer. To maintain the concentration water vapor or droplets are sprayed that are evaporated into the circulating stream of air[98].

Cooling is removing of heat or energy from a space and rejecting it to the environment outside by means of using means of temperature difference between gases and liquids or vapor (e.g., air, water, or various refrigerants). The sensible heat transfer in cooling mode operation is a negative value is removed or extracted from the air stream.

Dehumidification is the transfer or removal of water vapor from atmospheric air, as a consequence it results in the removal of heat known as latent energy and is denoted as negative.

3.1 Vapor compression cycle

The vapor compression cycle continuously changes a chemical substance or refrigerant from liquid to gas and vice-versa using the following stages[35]:

I. Compression- a low-pressure gas is compressed via a compressor, as a result, the overall pressure is increased.

II. Condensation- a high-pressure hot gas is in contact with the outdoor air via the condenser. As a result, heat is lost to the environment, and hot gas changes state to a liquid or vapor.

III. Expansion- an expansion value changes the volumetric area of the inlet and outlet ratio, reducing the pressure and temperature of the liquid.

IV. Evaporation- a low-pressure liquid removes heat from the given space or liquid via the evaporator. The liquid evaporates to a gas and the overall temperature is increased and the stage is repeated.

A refrigerant is a term that refers to any substance that absorbs heat. *Secondary refrigerant* is the term to classify substances that do not change state (gas to liquid or vice versa) water and brine that absorb heat but do not undergo a phase or state change. The above-listed stages define the process of each of the components of a basic refrigeration cycle in a vapor compression device. It is also important to understand the types of components used.

3.2 Compressor types

Typically, used compressors for the compression stage in the vapor compression cycle are presented below.

Rotary Compressor

Rotary compressors are used for large reversible heat pump applications and are comprised of screw and centrifugal compressors[99]. The capacity ranges from 150 tons to 10,000 tons and due to various configurations and complexity of the large plants, it will not be the focus of this research work.

Scroll Compressor

A scroll compressor is composed of two spiral-shaped vessels with a positive displacement. For this study, a scroll compressor is used to cater to a medium-scale commercial building. Fig. 8

depicts One scroll vessel is fixed while the counterpart is rotational about its axis and coupled to an electric motor.

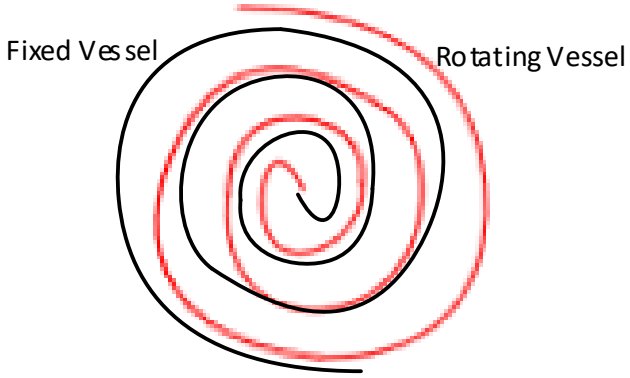

Figure 8 Scroll Vessel

The rotating scroll plate continuously compresses the refrigerant by changing the geometry of the scroll plates. This action results in compression of the refrigerant (working fluid). Scroll compressors are regarded as medium-capacity compressors with a working capacity from 1.5 tons to 40 tons (5.28 kW to 140.68 kW), with a maximum combined capacity of about 60-160 tons. Let us also understand the other components that are used in the Reversible Heat Pump (RHP).

Heat Exchangers (HE)

HEs are used in the condensation and evaporation stage of the vapor compression cycle. For this research a brazed plate HE and a fin and tube HE are used as the heat exchangers for cooling and heating mode operations. Brazed-plate HE is used on the water-to-refrigerant side and a fin and tube HE is used are the air-to-refrigerant side.

Brazed plate HE

The Brazed plate HE is utilized due to its higher operating pressure and temperature levels compared to the traditional Plate HE. The traditional gaskets are replaced with brazed plates and were originally developed in 1977[100]. It consists of several identical 0.3 mm thick stainless-steel plates compacted together with brazed metal in the middle. Multiple layers are assembled in succession, the brazed metal commonly used is copper with about 0.1 mm thickness while nickel alloy is used with ammonia compounds[100]. The operational range in terms of the temperature of a BPHE is -196 to 225 Degrees Celsius at about 30 bar pressure. BPHEs are less bulky, light in weight, relatively cheaper, and have higher operating points making them widely divested in district heating, refrigeration, and domestic boilers for medium heat capacity. To understand the thermal and hydraulic characteristics of a BPHE work by [101] gives a full insight.

Fin-and-tube HE

It is one of the most commonly used HEs, used in air-conditioning, refrigeration process equipment, and power plants. The fin-and-tube HE is used in application with the heat transfer coefficient of one fluid being lower in comparison to the other (Air to refrigerant). The high heat coefficient fluid is low in the pipes while the lower coefficient fluid flows along the fins[102]. Air flows outside in between the fins and the tubes that contain the refrigerant giving the name "Air-cooled HE". The fins are manufactured and arranged individually or continuously around the tubes.

Expansion Valve (EV)

EVs are used in the expansion stage of a vapor compression cycle. Typically, various types of EVs are available for heating and cooling applications. EVs are used for several reasons[77]:

a) maintain the pressure between the condenser and evaporator.
b) Meter flowrate of refrigerant to the evaporator (cooling) and condenser (heating) in reversible heat pump.
c) Ensure the compressor input is gas.

Traditionally, Thermostatic EVs (TEV) were widely used to control the flow rate of refrigerant while electronic EVs are currently diffused into the Vapor Compression (EEV) cycle for heating and cooling applications. The advantages of using an EEV over a TEV are that; the quick response in transient conditions [78], increases the overall Coefficient of Performance (COP) [103]and the smaller pressure difference between the high and low sides[79], [80]. The overall operation of RHP in cooling or heating mode depends on the positioning of the 4-way valve, it will be discussed in detail. Let's understand the cooling and heating process of an RHP.

HVAC technologies have an essential purpose in providing and maintaining a comfortable indoor environment for occupants. This thesis will focus mainly on Reversible Heat pumps (RHPs), as an essential cooling and heating mechanism, and provide an overview of different classifications of the technology, different components, and different modeling techniques (Chapter 3). To begin with, the working principle of a heat pump is to transfer heat via a circulating refrigerant (working fluid). The refrigerant tends to heat upon compression and cools once expanded, hence in a liquid state the refrigerant tends to evaporate (Vapor state) in a low-temperature heat exchanger (condenser) and is able to reject heat in a defined space. Once in vapor state, the refrigerant is

compressed and condensation occurs in the high temperature heat exchanger (evaporator) where heat is released to the environment as shown in Fig.9.

3.3 Cooling mode

During cooling mode operation, a reversible heat-pump operates as a chiller where the air-to-refrigerant heat exchanger is the condenser, the brazed-plate heat exchanger is the evaporator, the cooling mode expansion value (EV) is operational and the refrigerant is moving the direction indicated by the blue arrow. In cooling mode operation, the desired goal is to maintain the water supply temperature (T_{ws}) at a fixed temperature (e.g. 7 ^{o}C). The water return temperature (T_{wr}) tends to be warmer, it depends on the cooling demand of the building at any given instant.

Heat is removed from the warm water in the evaporator, by the flow of refrigerant and rejected to the environment at the condenser. An electric motor is used to maintain or regulate the flow of the refrigerant.

3.4 Heating mode

During heating mode operation, a reversible heat pump operates as a heat pump where the air-to-refrigerant heat exchanger is the evaporator, the brazed-plate heat exchanger is the condenser, and the heating mode EV is operational. The refrigerant is moving in the direction indicated by the red arrow. In heating mode operation, the desired goal is to maintain the water supply temperature (T_{ws}) at a fixed temperature (e.g. 40-55^{o}C). The water return temperature (T_{wr}) tends to be cooler, it depends on the cooling demand of the building at any given instant.

The active component exerting work in the system is the compressor, the work traditionally was achieved using engines, and as known from literature the efficiency of an engine is lower than available technologies, it is polluting to the environment and highly expensive to maintain. Motors succeeded as the workforce of RHP technologies due to high efficiency, low maintenance cost, less pollution to the environment, and its robust nature. The focus of this thesis will be on electrical motor-driven RHP systems.

3.5 Reversible Heat Pumps Operation with electrical drive

Before delving into the details of the thermodynamic and control modeling of a reversible air-to-water heat pump (HP), it is necessary to provide a schematic description of the reference unit. Fig. 9 illustrates the components, main variables, and acronyms. The refrigerant flow direction is indicated by red arrows for the 'heating mode' and blue arrows for the 'cooling mode'. In this system, an air-to-refrigerant heat exchanger (such as a tube-and-fin coil or a plate-and-fin unit) functions as the condenser (CND) during summer and as the evaporator (EVP) during winter. It is important to note that the outdoor air's temperature and relative humidity are denoted as ODT and RH, respectively. Additionally, a brazed-plate heat exchanger is employed to either cool or heat the water circulating in the hydraulic loop.

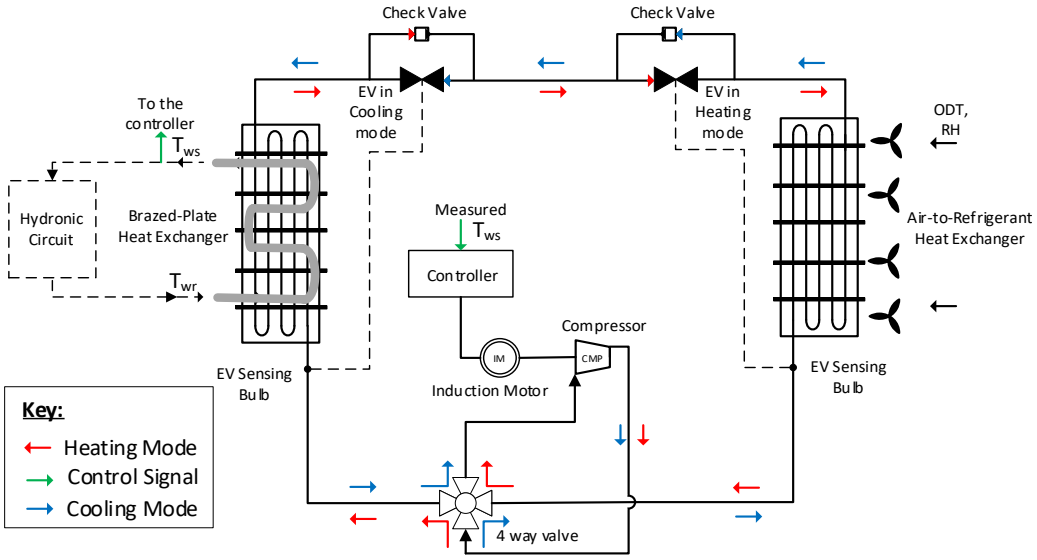

Figure 9 Simplified scheme of a reversible air-to-water HP

The temperature of the water returning from the hydronic loop is indicated as T_{wr}. Then, the HP heats (or cools down) the water flow rate to a desired temperature, indicated here as “supply temperature”, T_{ws} (green arrow in the figure). As shown in the figure, the compressor (CMP) is typically driven by an Induction Motor (IM). To maintain a de-sired value of the temperature of T_{ws}, the controller (CTRL) will act on the IM by regulating the speed (in the case of variable speed control) or cycling it “ON” and “OFF” (in the case of Start-stop control).

The model of a RHP is dependent upon the mode of operation (heating or cooling) and control topology (Constant or variable speed). This chapter will present all 4 configurations:

- Variable speed drive for cooling
- Variable speed drive for heating
- Constant speed control for cooling
- Constant speed control for heating

3.6 Variable Speed Drive (VSD)

Cooling mode:

An RHP model with VSD for cooling mode operation as an air-cooled chiller is presented. Two important quantities from literature are the cooling capacity delivered by the chiller (CC) and the mechanical power required by the CMP ($P_{m,C}$), Eqs 3.1.a-b are used respectively presented. More specifically, these quantities are given as a function of the compressor rotating speed (ω_{CMP}), the dry-bulb temperature of the outdoor air (ODT), and the temperature of the water returning from the hydronic circuit and entering the evaporator (T_{wr}).

$$CC = L_1\omega_{CMP} + L_2 ODT + L_3 T_{wr} \quad (3.1.a)$$

$$P_{m,C} = K_1\omega_{CMP} + K_2 ODT + K_3 T_{wr} \quad (3.1.b)$$

K_1, L_1, L_2, K_2, L_3, and K_3 are coefficients for ω_s, ODT and T_{wr}. These coefficients can be found by using numerical methods data available from experiments or ad-hoc simulations (see chapter 6). The temperature of the water entering the EVP, i.e., T_{wr} into the brazed plate heat exchanger, it is obtained from the dynamic model of the hydronic circuit served by the chiller. This simplified model, which is sufficient for this analysis is presented in Eq.3.2,

$$\frac{dT_{wr}}{dt} = \frac{1}{C_s}(\mathrm{CC} - \mathrm{CL}) \quad (3.2)$$

where the time variation of T_{wr} is proportional to the difference between the CC and the building cooling load (i.e., CL). C_s is a coefficient that quantifies the thermal inertia of the hydronic circuit coupled to the HP. Eqs.3.3.a-b were used to estimate this quantity. In particular, Eq.3.3.b is also known as the "Portoso's Equation" [34]which is typically used in Italy during the design phase of hydronic loops for air conditioning, to quantify the amount of water in the hydronic circuit for a safe operation of the compressors of vapor compression systems [104].

$$C_s = \rho_w \, c_{p,w} V_{des} \tag{3.3.a}$$

$$V_{des} = \frac{60 CC_{nom}}{\rho_w \, c_{p,w} \left(\frac{\Delta T_{wr}}{\Delta \tau}\right)_{ref}} \tag{3.3.b}$$

More specifically, ρ_w is the density of water, $c_{p,w}$ is the isobaric specific heat capacity of water, and V_{des} is the volume of the water desired in the hydronic loop for the safe operation of the HP. CC_{nom} is the nominal cooling capacity delivered by the reversible HP in the design point and $\left(\frac{\Delta T}{\Delta \tau}\right)_{ref}$ is the maximum variation of the water return from the hydronic loop in one minute. Typically, it is assumed to be 5 °C/min. This value was derived from observation in the field. If values larger than the mentioned threshold are assumed, it will be likely that the refrigerant exiting the EVP could be not superheated, thus damaging the CMP.

Once the CC, the temperature of the water supplied to the building (T_{ws}) is computed using the energy conservation applied to the chiller as shown in Eq.3.4,

$$T_{ws} = T_{wr} - \frac{\mathrm{CC}}{\dot{m}_w c_{p,w}} \tag{3.4}$$

where $\dot{m}_w$ is the mass flowrate of water circulating in the hydronic loop. The mass flowrate of water is constant through the operational period. Note that T_{ws} is typically assumed as the controlled variable by the action of the controller.

Once known the mechanical power required by the CMP (Eq.3.1-b), the mechanical load torque T_L is calculated using Eq.3.5, as a function of the compressor rotating speed (ω_{CMP} usually measured in rpm/min). The factor $\frac{60}{2\pi}$ is used to covert ω_{CMP} from rpm/min to rad/s [105].

$$T_L = \frac{60 \ \mathrm{P}_{m,C}}{2\pi \ \omega_{CMP}} \tag{3.5}$$

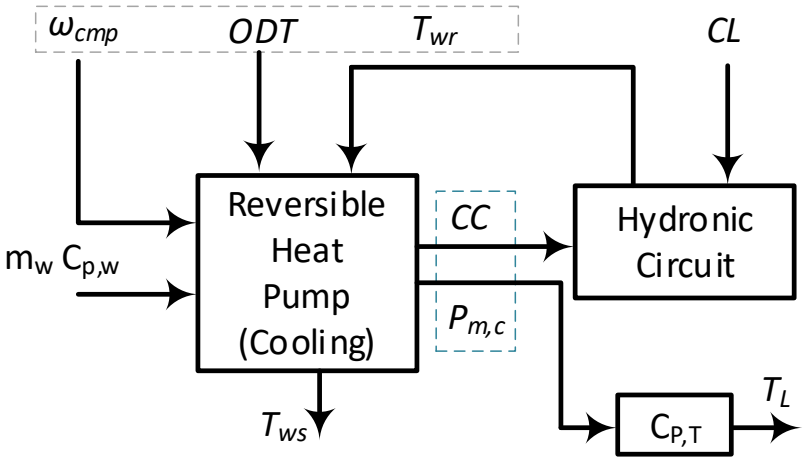

Figure 10 VSD Cooling Mode HP model

As depicted in Figure 10, the Refrigerant Heat Pump (RHP) in cooling mode is operational. The process begins by utilizing equation 3.1.a and 3.1.b, with inputs comprising ω_{CMP} (Compressor Speed), ODT (Outdoor Temperature), and T_{wr} (Return Water Temperature) as shown by the grey dotted lines. The outcomes of these equations are the Cooling Capacity (CC) and the Mechanical Power of the Compressor ($P_{m,C}$) as depicted by the blue botted lines. Both CC and the Cooling Load (CL) serve as inputs to the hydronic loop, facilitating the computation of T_{wr}, as outlined in equation 3.2. Concurrently, the Chiller Setpoint (C_s) is determined using equations 3.3.a and 3.3.b. Subsequently, T_{ws} is redefined according to equation 3.4 and employed as the controlling variable in a Variable Speed Drive (VSD) chiller during its cooling mode operation.

Heating mode:

An HP model with VSD for heating mode operation is presented. Two important quantities from the literature are the delivered heating capacity (HC) and the required mechanical power ($P_{m,H}$) for an HP. More specifically, both quantities are dependent on the compressor rotating speed (ω_{CMP}), the dry-bulb temperature, and the relative humidity of the outdoor air (indicated as ODT and RH, respectively), and the temperature of the water returning from the building and entering the HP's CND (T_{wr}).

In this work, Eqs.3.5.a-b are used for representing Eqs. 3.1.a-b. More specifically, as shown in the cited equations, HC and $P_{m,H}$ are given as a linear function of the main variables,

where K_1, L_1, L_2, K_2, L_3 , and K_3, are fitting coefficients for ω_{CMP}, ODT, and T_{wr}. These unknown coefficients can be derived by using numerical methods applied to data collected from experiments or ad-hoc simulations. It is worth noting that RH is not included in Eqs 3.5.a-b. As will be seen later, the moderately cold winter of the reference climatic zone does not result in frost formation on the evaporator surface. Therefore, the RH value has a negligible influence in this case. In addition, it also necessary to stress that for these reason, the model described in the following is limited only for those cases where the defrosting cycle is rarely activated. Regarding the *ODT* values in Eqs 3.5.a-b, they can be obtained by using a weather database. Conversely, the temperature of the water returning from the hydraulic loop, i.e., T_{wr}, depends on the heating demand of the user (in the following indicated as heating load, *HL*) and the thermal inertia of the hydronic loop. More specifically, Eq. 3.6 represents the dynamic model of the hydronic circuit served by the HP,

$$HC = L_1\omega_{CMP} + L_2 ODT + L_3 T_{wr} \tag{3.5.a}$$

$$P_{m,H} = K_1\omega_{CMP} + K_2 ODT + K_3 T_{wr} \tag{3.5.b}$$

$$\frac{dT_{wr}}{dt} = \frac{1}{C_s}(HC - HL) \tag{3.6}$$

where the variation of T_{wr} is directly related to the difference between *HC* and *HL* (i.e., the difference between the HP's capacity and the heating load). C_s is a coefficient (kJ/°C) used to account for the inertia of the hydronic loop coupled to the HP. Eqs 3.7.a-b were adopted to estimate this quantity. More specifically, in Eq. 3.7.a ρ_w is the density of water, c_w is the specific heat capacity of water, and V_{des} is the desired volume of water in the hydronic loop. This quantity is derived from "Portoso's Equation" [106], and it is often adopted as a "Rule of Thumb" to estimate the desired amount of water in the hydronic loop, needed for a safe operation of the CMPs,

$$C_s = \rho_w\, c_w V_{des} \tag{3.7.a}$$

$$V_{des} = \frac{60\, C_{nom}}{\rho_w\, c_w \left(\frac{\Delta T}{\Delta \tau}\right)_{ref}} \tag{3.7.b}$$

In Eq. 3.7.b, C_{nom} is the nominal capacity delivered by the HP (typically in cooling mode) at the design condition and $\left(\frac{\Delta T}{\Delta \tau}\right)_{ref}$ is the maximum variation of the water return temperature from

the hydronic loop (typically set to 5 °C/min). Finally, the temperature of the water supplied to the building (T_{ws}) is calculated by applying the energy conservation equation to the HP as shown in Eq. 3.8,

$$T_{ws} = T_{wr} + \frac{HC}{\dot{m}_w c_w} \tag{3.8}$$

where $\dot{m}_w$ is the mass flow rate of water circulating entering the HP. Note that T_{ws} is assumed as the controlled variable by the action of the controller.

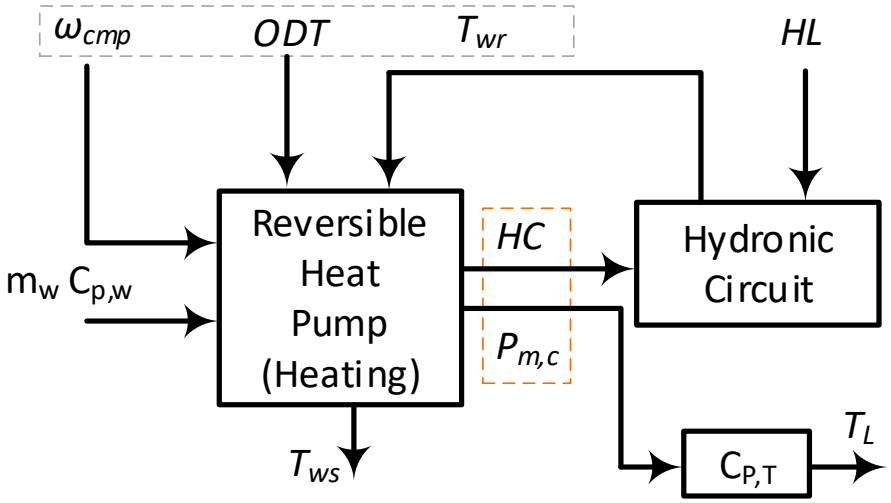

Figure 11 VSD heating mode model

As depicted in Figure 11, the Reversible Heat Pump (RHP) in heating mode operation. The process begins by utilizing equations 3.5.a and 3.5.b, with inputs comprising ω_{CMP} (Compressor Speed), ODT (Outdoor Temperature), and T_{wr} (Return Water Temperature) as shown by the grey dotted lines. The outcomes of these equations are the Heating Capacity (HC) and the Mechanical Power of the Compressor ($P_{m,H}$) as depicted by the red botted lines. Both HC and the Heating Load (HL) serve as inputs to the hydronic loop, facilitating the computation of T_{wr}, as outlined in equation 3.6. Concurrently, the Chiller Setpoint (C_s) is determined using equations 3.7.a and 3.7.b. Subsequently, T_{ws} is redefined according to equation 8 and employed as the controlling variable in a Variable Speed Drive (VSD) heat pump during its heating mode operation.

3.7 Constant Speed Control (CSC)

Cooling mode

An HP model with CSC for cooling mode operation is presented. Two important quantities from literature are the cooling capacity delivered by the chiller (CC) and the mechanical power required by the CMP ($P_{m,C}$), Eqs 3.9.a-b are used respectively. More specifically, these quantities are given as a function of the dry-bulb temperature of the outdoor air (ODT), and the temperature of the water returning from the hydronic circuit and entering the evaporator (T_{wr}).

$$CC = L_1 ODT + L_2 T_{wr} \quad (3.9.a)$$

$$P_{m,C} = K_1 ODT + K_2 T_{wr} \quad (3.9.b)$$

K_1, L_1, L_2, K_2, L_3, and K_3 are coefficients for ω_s, ODT and T_{wr}. These coefficients can be found by using numerical methods data available from experiments or ad-hoc simulations. In order to model the overall system equation 3.2 to equation 3.5 can be used from sections.

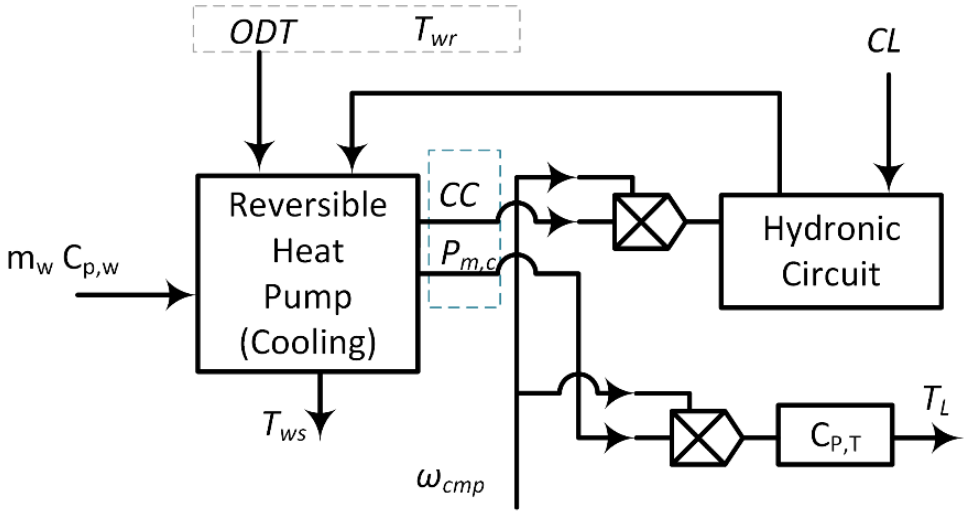

Figure 12 CSC model for cooling mode

As shown in Figure 12, the Reversible Heat Pump (RHP) is in cooling mode operation. The process begins by utilizing equations 3.9.a and 3.9.b, with inputs ODT (Outdoor Temperature), and T_{wr} (Return Water Temperature) as shown by the grey dotted lines. The outcomes of these equations are the Cooling Capacity (CC) and the Mechanical Power of the Compressor ($P_{m,C}$) as depicted by the blue botted lines. Both CC and the Cooling Load (CL) serve as inputs to the hydronic loop, facilitating the computation of T_{wr}, as outlined in equation 3.2. Concurrently, the Chiller Setpoint (C_s) is determined using equations 3.3.a and 3.3.b. Subsequently, T_{ws} is redefined according to

equation 3.4 and employed as the controlling variable in a Constant speed control (CSC) chiller during its Cooling mode operation.

Heating mode:

An HP model with VSD for heating mode operation is presented. Two important quantities from literature are the delivered heating capacity (HC) and the required mechanical power ($P_{m,H}$) for an HP. More specifically, both quantities are dependent on the compressor rotating speed (ω_{CMP}), the dry-bulb temperature, and the relative humidity of the outdoor air (indicated as ODT and RH, respectively), and the temperature of the water returning from the building and entering the HP's CND (T_{wr}).

$$HC = L_1\omega_{CMP} + L_2 ODT + L_3 T_{wr} \quad (3.10.a)$$

$$P_{m,H} = K_1\omega_{CMP} + K_2 ODT + K_3 T_{wr} \quad (3.10.b)$$

In this work, Eqs. 3.10.a-b are used for representing Eqs 3.1.a-b. More specifically, as shown in the cited equations, HC and $P_{m,H}$ are given as a linear function of the main variables, where K_1, L_1, L_2, K_2, L_3 , and K_3, are fitting coefficients for ω_{CMP}, ODT, and T_{wr}. These unknown coefficients can be derived by using numerical methods applied to data collected from experiments or ad-hoc simulations. It is worth noting that RH is not included in Eqs 3.2.a-b. As will be seen later, the moderately cold winter of the reference climatic zone does not result in frost formation on the evaporator surface.

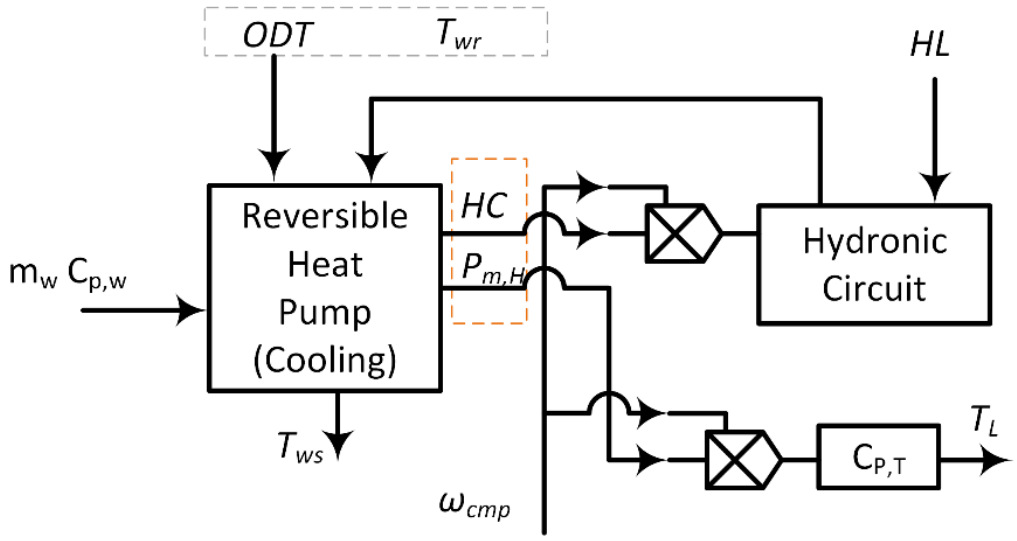

Figure 13 CSC model for heating model

As depicted in Figure 13, the Reversible Heat Pump (RHP) in heating mode operation. The process begins by utilizing equations 3.10.a and 3.10.b, with inputs comprising ODT (Outdoor Temperature), and T_{wr} (Return Water Temperature) as shown by the grey dotted lines. The outcomes of these equations are the Heating Capacity (HC) and the Mechanical Power of the Compressor ($P_{m,H}$) as depicted by the red botted lines. Both HC and the Heating Load (HL) serve as inputs to the hydronic loop, facilitating the computation of T_{wr}, as outlined in equation 3.6. Concurrently, the Chiller Setpoint (C_s) is determined using equations 3.7.a and 3.7.b. Subsequently, T_{ws} is redefined according to equation 8 and employed as the controlling variable in a Variable Speed Drive (VSD) heat pump during its heating mode operation.

3.8 Multi-variable model:

For cooling mode operation of chiller linear equations for modeling CC and P_m are presented below:

$$CC = A_0 + A_1 T_{wr} + A_2 ODT + A_3 f + A_4 ODT\, T_{wr} + A_5 f^2 + A_6 T_{wr} f + A_7 ODT\, f \qquad (3.11)$$

$$P_{m,C} = B_0 + B_1 T_{wr} + B_2 ODT + B_3 f + B_4 ODT\, T_{wr} + B_5 f^2 + B_6 T_{wr} f + B_7 ODT\, f \qquad (3.12)$$

The coefficients $A_0,\ A_1,\ A_2,\ A_3,\ A_4,\ A_5,\ A_6,\ A_7,\ B_0,\ B_1,\ B_2,\ B_3,\ B_4,\ B_5,\ B_6,\ and\ B_7$ are obtained using regression methodology to model the quantities. This approach it used in few published articles [107], [108] where a combination of the input variables are used. However, unlike the initially proposed model, this particular approach increases the

For heating mode operation of chiller linear equations for modelling HC and $P_{m,H}$ are presented below:

$$HC = A_0 + A_1 T_{wr} + A_2 ODT + A_3 f + A_4 ODT\, T_{wr} + A_5 f^2 + A_6 T_{wr} f + A_7 ODT\, f \qquad (3.13)$$

$$P_{m,H} = B_0 + B_1 T_{wr} + B_2 ODT + B_3 f + B_4 ODT\, T_{wr} + B_5 f^2 + B_6 T_{wr} f + B_7 ODT\, f \qquad (3.14)$$

The coefficients $A_0,\ A_1,\ A_2,\ A_3,\ A_4,\ A_5,\ A_6,\ A_7,\ B_0,\ B_1,\ B_2,\ B_3,\ B_4,\ B_5,\ B_6,\ and\ B_7$ are obtained using regression methodology to model the quantities

3.9 State space model

To implement the state-space model of an RHP, separate model will be presented for a chiller (cooling mode) and heat-pump (heating mode). Considering to above steady state Eqs 3.1.a. and 3.1.b are rewritten with dynamics. It also important to highlight that eqn 3.1.b is considered redundant since the induction motor modelling (see chapter 2) already incorporates the electrical power and mechanical power is achieved using eqn. 3.15 since the electromagnetic torque is already known.

$$\mathrm{P}_{m,C} = \frac{\omega_{CMP}\ \mathrm{T}_e}{2\pi\ \omega_{CMP}} \qquad (3.15)$$

3.9.1 VSD Cooling Mode

Let's rewrite eqn. 3.1.a with dynamics, by taking $CC = u$, where $u = L_1 \omega_{CMP}(\mathrm{k}) + L_2 ODT(k) + L_3 T_{wr}(k)$. This gives the definition of:

$$\dot{CC}(\mathrm{k}) = -\alpha CC(k) + u \qquad (3.16.a)$$

Expanding the term:

$$\dot{CC}(\mathrm{k}) = -\alpha CC\ (k) + L_1 \omega_{CMP}(\mathrm{k}) + L_2 ODT(k) + L_3 T_{wr}(k) \qquad (3.16.b)$$

Using Euler's backward difference discretization to eqn. 3.16.b:

$$CC(\mathrm{k}+1) = (1 - \alpha T_s) CC(k) + T_s L_1 \omega_{CMP}(\mathrm{k}) + T_s L_2 ODT(k) + T_s L_3 T_{wr}(k) \qquad (3.17)$$

Taking the Euler difference discretization for eqn. 3.2, note $\frac{dT_{wr}}{dt} = \dot{T_{wr}}(k)$:

$$T_{wr}(\mathrm{k}+1) = T_{wr}(\mathrm{k}) + \frac{T_s}{C_s}(\mathrm{CC(k)} - \mathrm{CL(k)}) \qquad (3.18)$$

Taking eqn.3.17 and eqn. 3.18 the state space equation for RHP is cooling mode as a chiller is obtained:

$$\begin{bmatrix} CC(\mathrm{k}+1) \\ T_{wr}(\mathrm{k}+1) \end{bmatrix} = \begin{bmatrix} 1-\alpha T_s & T_s L_3 \\ \frac{T_s}{C_s} & 1 \end{bmatrix} \begin{bmatrix} CC(k) \\ T_{wr}(k) \end{bmatrix} + \begin{bmatrix} T_s L_1 & T_s L_2 & 0 \\ 0 & 0 & -\frac{T_s}{C_s} \end{bmatrix} \begin{bmatrix} \omega_{CMP}(\mathrm{k}) \\ ODT(k) \\ \mathrm{CL(k)} \end{bmatrix} \quad (3.19)$$

The states of the RHP in cooling mode are $\begin{bmatrix} CC(k) \\ T_{wr}(k) \end{bmatrix}$ and system inputs are $\begin{bmatrix} \omega_{CMP}(\mathrm{k}) \\ ODT(k) \\ \mathrm{CL(k)} \end{bmatrix}$.

it is note worthy that the control variable is T_{ws} and it is obtained using eqn. 3.4 in discrete form as shown in eqn. 3.20:

$$T_{ws}(\mathrm{k}) = T_{wr}(\mathrm{k}) - \frac{\mathrm{CC\ (k)}}{\dot{m}_w c_{p,w}} \quad (3.20)$$

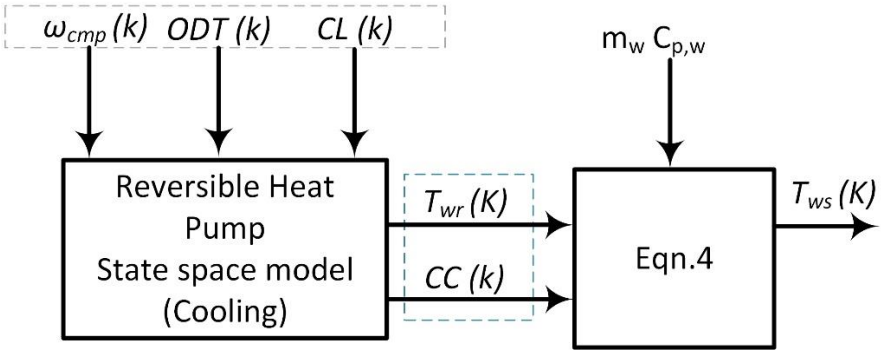

Figure 14 RHP State-space model for VSD in cooling operation

Figure 14, illustrates the Reversible Heat Pump (RHP) in cooling mode operation represented as a state space model. The process begins by utilizing equations 3.17 and 3.18, with inputs ODT (Outdoor Temperature), ω_{CMP} (Compressor Speed), and the Cooling Load (CL) as shown by the grey dotted lines. The states of these equations are the Cooling Capacity (CC) and the Temperature of water return (T_{wr}) as depicted by the blue botted lines. Both CC and T_{wr} serve as inputs to eqn. 3.4, facilitating the computation of T_{ws}, as outlined in the figure above. Subsequently, T_{ws} is redefined according to equation 3.4 and employed as the controlling variable in a variable speed control (VSC) during its Cooling mode operation.

3.9.2 VSD Heating Mode

Lets rewrite eqn. 3.5.a with dynamics, by taking $HC = u$, where $u = L_1\omega_{CMP}(\mathrm{k}) + L_2 ODT(k) + L_3 T_{wr}(k)$. This gives the definition of:

$$\dot{HC}(\mathrm{k}) = -\alpha HC(k) + u \tag{3.21.a}$$

Expanding the term:

$$\dot{HC}(\mathrm{k}) = -\alpha HC\ (k) + L_1\omega_{CMP}(\mathrm{k}) + L_2 ODT(k) + L_3 T_{wr}(k) \tag{3.21.b}$$

Using Euler's backward difference discretization to eqn. 3.21.b:

$$HC(\mathrm{k}+1) = (1 - \alpha T_s)HC(k) + T_s L_1\omega_{CMP}(\mathrm{k}) + T_s L_2 ODT(k) + T_s L_3 T_{wr}(k) \tag{3.22}$$

Let's take the Euler difference discretization for eqn. 3.6:

$$T_{wr}(\mathrm{k}+1) = T_{wr}(\mathrm{k}) + \frac{T_s}{C_s}(\mathrm{HC(k)} - \mathrm{HL(k)}) \tag{3.23}$$

Taking eqn. 3.22 and eqn. 3.23 the state space equation for RHP is cooling mode as a chiller is obtained:

$$\begin{bmatrix} HC(\mathrm{k}+1) \\ T_{wr}(\mathrm{k}+1) \end{bmatrix} = \begin{bmatrix} 1 - \alpha T_s & T_s L_3 \\ \dfrac{T_s}{C_s} & 1 \end{bmatrix} \begin{bmatrix} HC(k) \\ T_{wr}(k) \end{bmatrix} + \begin{bmatrix} T_s L_1 & T_s L_2 & 0 \\ 0 & 0 & -\dfrac{T_s}{C_s} \end{bmatrix} \begin{bmatrix} \omega_{CMP}(\mathrm{k}) \\ ODT(k) \\ \mathrm{HL(k)} \end{bmatrix} \tag{3.24}$$

The states of the RHP in cooling mode are $\begin{bmatrix} HC(k) \\ T_{wr}(k) \end{bmatrix}$ and system inputs are $\begin{bmatrix} \omega_{CMP}(\mathrm{k}) \\ ODT(k) \\ \mathrm{HL(k)} \end{bmatrix}$. it is note worthy that the control variables is T_{ws} and it is obtained using eqn. 3.4 in discrete form as shown in eqn. 3.25:

$$T_{ws}(\mathrm{k}) = T_{wr}(\mathrm{k}) - \frac{\mathrm{HC\ (k)}}{\dot{m}_w c_{p,w}} \tag{3.25}$$

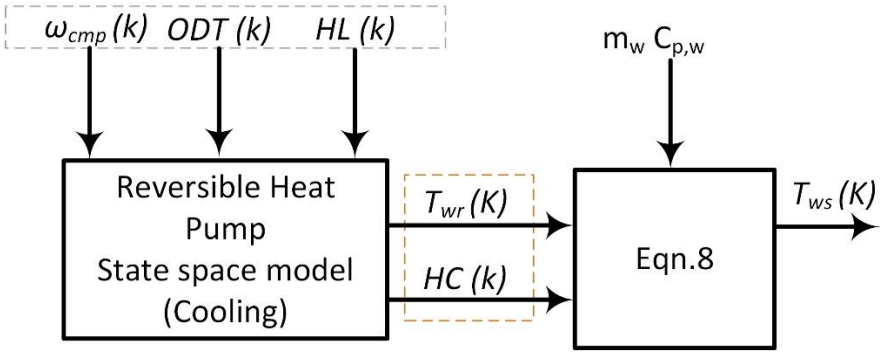

Figure 15 RHP State-space model for VSD in heating operation

Figure 15 illustrates the Reversible Heat Pump (RHP) in cooling mode operation represented as a state space model. The process begins by utilizing equations 3.22 and 3.23, with inputs ODT (Outdoor Temperature), ω_{CMP} (Compressor Speed), and the heating Load (HL) as shown by the grey dotted lines. The states of these equations are the Heating Capacity (HC) and the Temperature of water return (T_{wr}) as depicted by the blue botted lines. Both HC and T_{wr} serve as inputs to eqn. 3.25, facilitating the computation of T_{ws}, as outlined in the figure above. Subsequently, T_{ws} is redefined according to equation 3.4 and employed as the controlling variable in a variable speed control (VSC) during its Cooling mode operation.

3.9.3 Constant Speed RHP Cooling

Lets rewrite eqn. 3.9.a with dynamics, by taking $CC = u$, where $u = L_1 ODT(k) + L_2 T_{wr}(k)$. This gives the definition of:

$$\dot{CC}(\mathrm{k}) = -\alpha CC(k) + u \tag{3.26.a}$$

Expanding the term:

$$\dot{CC}(\mathrm{k}) = -\alpha CC\ (k) + L_1 ODT(k) + L_2 T_{wr}(k) \tag{3.26.b}$$

Using Euler's backward difference discretization to eqn. 3.26.b:

$$CC(\mathrm{k}+1) = (1 - \alpha T_s) CC(k) + T_s L_1 ODT(k) + T_s L_2 T_{wr}(k) \tag{3.27}$$

Taking eqn. 3.27 and eqn. 3.18 the state space equation for RHP is cooling mode as a chiller is obtained:

$$\begin{bmatrix} CC(\mathrm{k}+1) \\ T_{wr}(\mathrm{k}+1) \end{bmatrix} = \begin{bmatrix} 1-\alpha T_s & T_s L_2 \\ \dfrac{T_s}{C_s} & 1 \end{bmatrix} \begin{bmatrix} CC(k) \\ T_{wr}(k) \end{bmatrix} + \begin{bmatrix} T_s L_1 & 0 \\ 0 & -\dfrac{T_s}{C_s} \end{bmatrix} \begin{bmatrix} ODT(k) \\ CL(k) \end{bmatrix} \quad (3.28)$$

The states of the RHP in cooling mode are $\begin{bmatrix} CC(k) \\ T_{wr}(k) \end{bmatrix}$ and system inputs are $\begin{bmatrix} ODT(k) \\ CL(k) \end{bmatrix}$. it is note worthy that the control variable is T_{ws} and it is obtained using eqn. 3.4 in discrete form as shown in eqn. 3.20:

$$T_{ws}(\mathrm{k}) = T_{wr}(\mathrm{k}) - \frac{\mathrm{CC\ (k)}}{\dot{m}_w c_{p,w}} \quad (3.29)$$

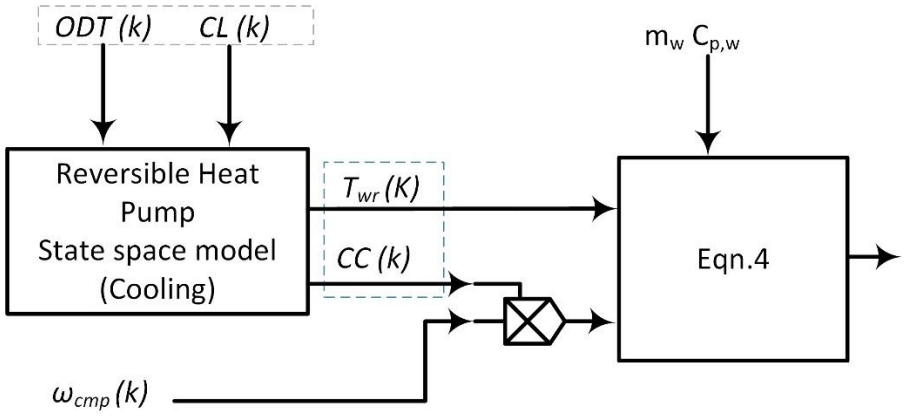

Figure 16 RHP State-space model for CSC in cooling operation

Figure 16 illustrates the Reversible Heat Pump (RHP) in cooling mode operation represented as a state space model. The process begins by utilizing equations 3.27 and 3.18, with inputs ODT (Outdoor Temperature), and the Cooling Load (CL) as shown by the grey dotted lines. The states of these equations are the Cooling Capacity (CC) and the Temperature of water return (T_{wr}) as depicted by the blue dotted lines. Both CC and T_{wr} serve as inputs to eqn. 3.4, facilitating the computation of T_{ws}, as outlined in the figure above. Subsequently, T_{ws} is redefined according to equation 3.4 and employed as the controlling variable in a constant speed control (CSC) during its Cooling mode operation.

3.9.4 Constant Speed RHP Heating

Lets rewrite eqn. 3.5.a with dynamics, by taking $HC = u$, where $u = L_1 ODT(k) + L_2 T_{wr}(k)$. This gives the definition of:

$$\dot{HC}(\mathrm{k}) = -\alpha HC(k) + u \tag{3.30.a}$$

Expanding the term:

$$\dot{HC}(\mathrm{k}) = -\alpha HC\ (k) + L_1 ODT(k) + L_2 T_{wr}(k) \tag{3.30.b}$$

Using Euler's backward difference discretization to eqn. 3.30.b:

$$HC(\mathrm{k}+1) = (1 - \alpha T_s) HC(k) + T_s L_1 ODT(k) + T_s L_2 T_{wr}(k) \tag{3.31}$$

Let's take the Euler difference discretization for eqn. 3.2:

$$T_{wr}(\mathrm{k}+1) = T_{wr}(\mathrm{k}) + \frac{T_s}{C_s}(\mathrm{HC(k)} - \mathrm{HL(k)}) \tag{3.32}$$

Taking eqn. 3.31 and eqn. 3.32 the state space equation for RHP is cooling mode as a chiller is obtained:

$$\begin{bmatrix} HC(\mathrm{k}+1) \\ T_{wr}(\mathrm{k}+1) \end{bmatrix} = \begin{bmatrix} 1 - \alpha T_s & T_s L_2 \\ \frac{T_s}{C_s} & 1 \end{bmatrix} \begin{bmatrix} HC(k) \\ T_{wr}(k) \end{bmatrix} + \begin{bmatrix} T_s L_1 & 0 \\ 0 & -\frac{T_s}{C_s} \end{bmatrix} \begin{bmatrix} ODT(k) \\ HL(k) \end{bmatrix} \tag{3.33}$$

The states of the RHP in Heating mode are $\begin{bmatrix} HC(k) \\ T_{wr}(k) \end{bmatrix}$ and system inputs are $\begin{bmatrix} ODT(k) \\ HL(k) \end{bmatrix}$. it is note worthy that the control variables is T_{ws} and it is obtained using eqn. 3.4 in discrete form as shown in eqn. 3.25.

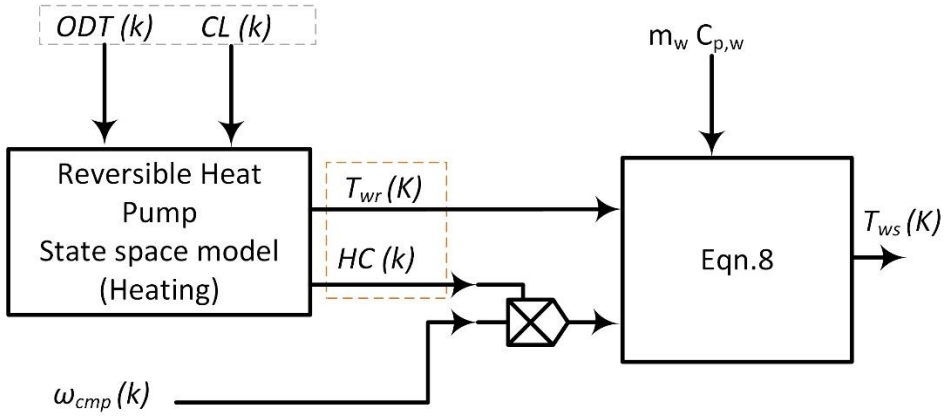

Figure 17 RHP State-space model for CSC in heating operation

Fig. 17 illustrates the Reversible Heat Pump (RHP) in cooling mode operation represented as a state space model. The process begins by utilizing equations 3.31 and 3.32, with inputs ODT (Outdoor Temperature), and the Heating Load (HL) as shown by the grey dotted lines. The states

of these equations are the Heating Capacity (HC) and the Temperature of water return (T_{wr}) as depicted by the blue botted lines. Both HC and T_{wr} serve as inputs to eqn. 3.4, facilitating the computation of T_{ws}, as outlined in the figure above. Subsequently, T_{ws} is redefined according to equation 3.4 and employed as the controlling variable in a constant speed control (CSC) during its Heating mode operation.

Summary:

Chapter 3, gives an insight into the basic concepts covers in a thermodynamic heating and cooling system. A brief description of vapor compression cycle, compressor types, and reversible heat pump compoenents are given. Electrical drives contribution is given to RHP technology and two basic control techniques (variable speed and constant speed) are discussed. Modeling of a RHP using physical model is presented with multi-variable models. A state-space model for variable and constant speed is developed for heating and cooling applications. The 3D plot for cooling and heating mode operation are presented in appendix 1 and 2 respectively. The RLS approximation of the plant is presented in appendix 4.

Chapter 4

Control techniques

Objectives:

- Provide an insight into motor control techniques
- To present heat pump control techniques
- Present variable set-point temperature control

4.1 Induction Motor Control

Control techniques of induction machines (IMs) can be divided into two main categories: scalar and vector controls. Scalar control is based on the steady-state model of the IM and therefore permits regulating at steady-state only the magnitudes and frequency of the stator voltages, currents, flux linkages, and electromagnetic torque. Since it does not act on the angular position of the space vectors of the control variables, it does not permit the best dynamic performance to be achieved. On the contrary, vector controls are based on the dynamic model of the machine; they permit the drive to achieve its best dynamic performance in terms of electromagnetic torque control, thanks to their feature to take into consideration the instantaneous angular position of the stator voltages, currents as well as of the flux linkages.

Although vector control can provide higher dynamic performance, some kinds of mechanical loads exist which do not require a high dynamic performance. Typical examples are fans and pumps where it is sufficient to regulate the speed of the IM with adequate efficiency over a wide speed range. This implies that it is sufficient to use the steady-state model of the IM instead of the dynamic one, as far as the control system design is concerned. The machine is supposed to be supplied by a pulse width modulation (PWM) voltage source inverter (VSI), able to generate a set of three-phase voltages whose fundamental component is characterized by the desired amplitude and frequency. Scalar control of IMs was born with the idea to use as a simple control method for regulating the speed of an AC machine.

4.2 Open-Loop Scalar Control

Since it is impossible to control the air gap voltage (E_g)directly with a voltage-fed inverter, the practical way to control the speed of the IM is to regulate its supply frequency in open-loop while simultaneously keeping constant the (supply voltage/frequency)U_s/f ratio. So long as E_g is high enough, it is acceptable to ignore the voltage drop in the stator resistance and leakage inductance, and then to consider$U_s \approx E_g$: this happens for sufficiently high speeds.

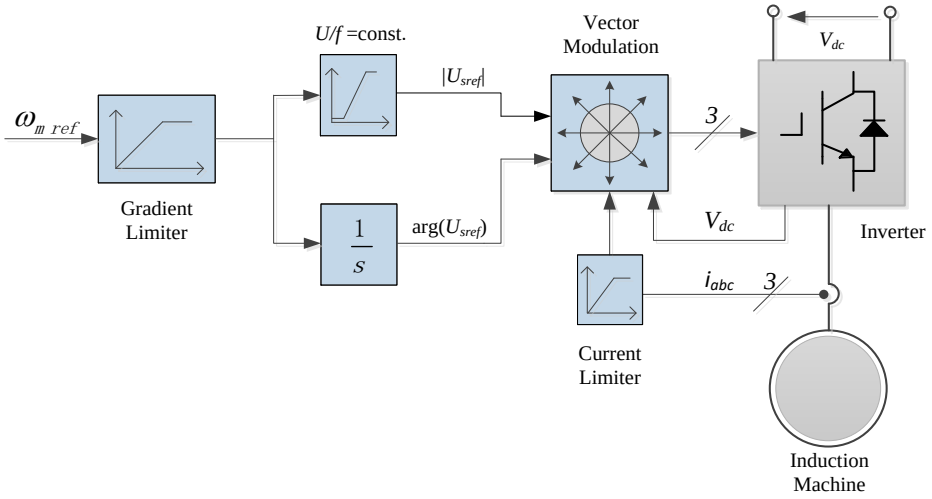

Figure 18 Block diagram of the open-loop scalar control

Fig 18 shows the block diagram of an open-loop scalar control scheme [96]. In this scheme, the gradient limiter reduces the bandwidth of the stator frequency reference. The band-limited stator frequency reference then generates the stator voltage reference magnitude while its integral determines the phase angle. The amplitude and phase of the reference stator voltage space-vector constitute the input of the space vector PWM system that, in turn, establishes the switching pattern of the inverter synthesizing the reference voltages.

The $|\mathbf{U}_s|/\omega_1$ ratio defines the rate of change of the linear function in Fig 5.1 and is usually set equal to the rated stator flux amplitude of the machine, $|\mathbf{U}_s|/\omega_1 = |\Psi_{srat}|$, when the motor speed remains below the rated one. Above the rated speed, field weakening can be simply achieved by limiting the voltage amplitude to the rated voltage of the machine, $|\mathbf{U}_s| = |\mathbf{U}_{srat}|$. At very low stator frequency, there is a preset minimum value of the supply stator voltage so as to account for the resistive stator voltage drop, $|\mathbf{U}_s| = |\mathbf{U}_{s\,min}|$. This is due to the fact that, because of a non-null value

of the stator resistance, as long as the supply frequency reduces, the stator flux amplitude decreases too. A compensator can be deployed to take account of this voltage deeply as explained in 3.3.2.

Even if theoretically no stator current sensor is needed, since no direct current control is performed, in practical terms, it is frequently mounted to inhibit the switching of the inverter power devices for overload protection in the presence of over currents.

4.3 Closed-Loop Scalar Control

This section corresponds to varying only the synchronous speed of the drive, while maintaining U_s/ω ratio constant, without the need of measuring the machine speed on the one hand, but without the possibility to compensate any variation of the speed caused by the load torque on the other hand. Thus, when more speed accuracy is required, the closed-loop control strategy should be adopted. The closed-loop control of the rotor speed can be achieved with the scheme in Fig. 19, where the speed PI controller employs the speed error signal to compensate the slip frequency.

In Fig. 19 to compensate for the slip frequency, the speed signal should be detected. The reference speed ω_{mref} is compared with the measured one ω_m, and the error is then processed by a PI controller. The output of such a controller is the reference slip speed ω_{2ref} which, added to the measured speed, provides the stator pulsation reference ω_{1ref}. The reference slip speed must be properly limited to the range where the speed/torque relationship is almost linear, to avoid pull-out phenomena. Then the same structure explained in 3.2.2 is adopted.

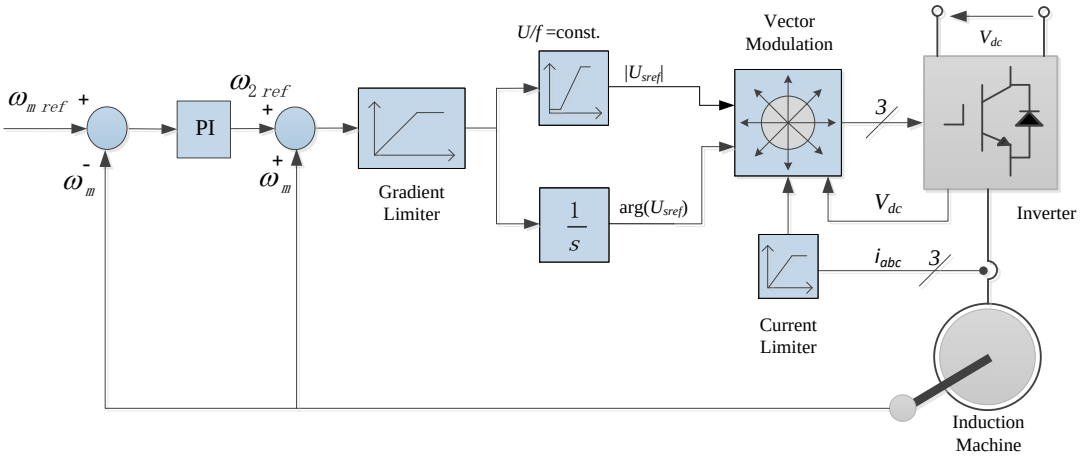

Figure 19 Block diagram of the closed-loop scalar control with impressed voltages

4.4 Improved Closed-Loop Scalar Control

As explained, the presumption that $U_s=E_g$ is not always true especially at low speed range, where E_g is not high enough, the voltage drop in the stator windings should also be considered. As a comparison, Fig 21 shows the torque-speed characteristics of the same 2.2 kW machine with constant U_s/ω.

From fig. 20, for a given supply frequency, it is clear that the breakdown slip is smaller than those in constant E_g/ω condition and moreover the maximum torque cannot be kept constant; finally, the slip range corresponding to linear torque-slip characteristic becomes narrower. This becomes even worse at low speeds.

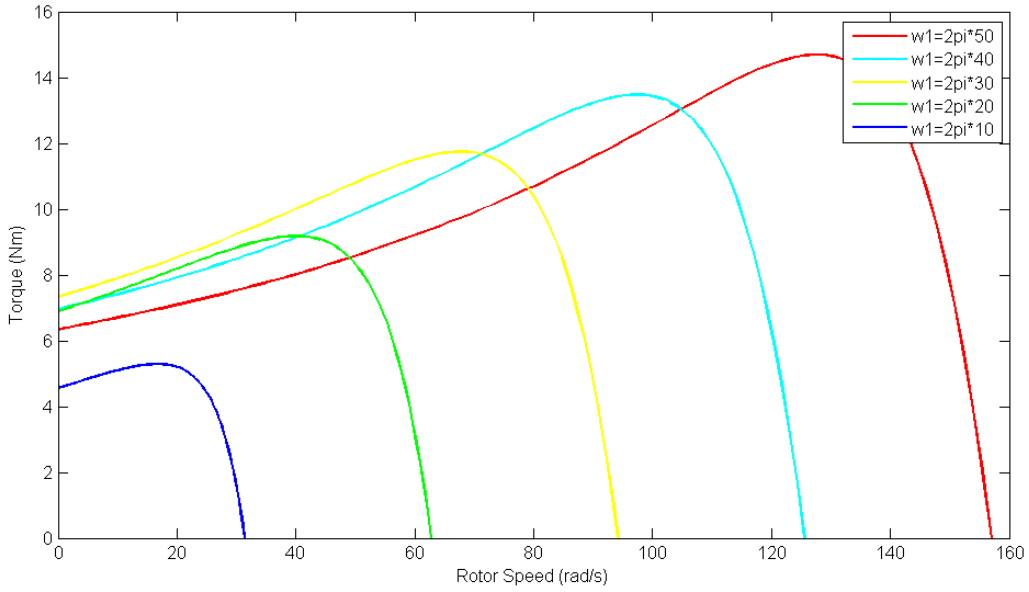

Figure 20 que-speed characteristic of an IM under constant Ug/f

A boost voltage is necessary at low frequencies to compensate for the voltage drop. However, if this voltage is set high enough to achieve rated torque when the excitation frequency equals the slip frequency, it will be too excessive for the motor to operate under no-load conditions at the same excitation frequency for extended periods, leading to excessive heating. To address this issue, many drives employ a special 'starting' procedure. This procedure applies a high boost voltage for only a few seconds, enough to initiate motor startup, after which the running boost voltage is reduced. A more advanced approach involves adjusting the stator voltage reference based on the relationship with the stator resistance ohmic drop, thus compensating for it.

$$\mathbf{U}_s \cong \mathbf{\Psi}_m \left[\omega_1 + \frac{R_s}{R_r} \omega_2 \right] \tag{4.1}$$

where $\mathbf{\Psi}_m$ is the space-vector of the steady-state magnetizing flux, ω_2 is the slip pulsation, R_s and R_r are the stator and rotor resistances. On the basis of eqn.4.1, the following simple stator resistance voltage drop compensation method has been adopted, to maintain the magnetizing flux amplitude constant, even under heavy load:

$$\begin{aligned} |\mathbf{U}_s| &= \frac{\left[\omega_1 + \frac{R_s}{R_r} \omega_2 \right]}{\left[\omega_{1rat} + \frac{R_s}{R_r} \omega_2 \right]} |\mathbf{U}_{srat}| \cong \\ &\cong \frac{|\mathbf{U}_{srat}|}{\omega_{1rat}} \omega_1 + \frac{|\mathbf{U}_{srat}| R_s}{\omega_{1rat} R_r} \omega_2 = \\ &= \mathbf{U}_{s1} + \mathbf{U}_{scomp} = \mathbf{U}_{stot} \end{aligned} \tag{4.2}$$

This method relies on the realistic assumption that the rated pulsation in the denominator of the second term is much higher than the component dependant on the slip pulsation. The third term indicates that for low speeds the voltage component dependent of the slip pulsation is added.

Fig. 21 shows the block diagram of the proposed improved scalar controlled induction motor drive. The main difference here is that the voltage compensation part is introduced into the scheme.

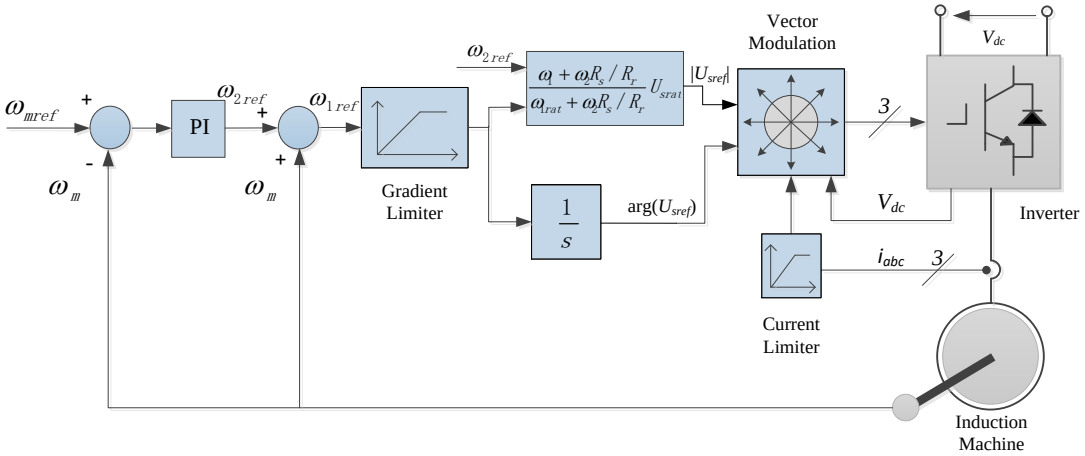

Figure 21 Block diagram of the improved scalar drive

4.5 Controller Design

The closed loop scalar control refers to the scheme of controlling the motor torque and speed by proportionally varying the voltage with supply frequency to keep the air-gap flux constant and achieve up to rated torque at any speed by controlling the slip pulsation. Equation (4.2) clearly shows that T_e is in proportional to the slip pulsation $s\omega_1 = \omega_2$, if $|V_s|/\omega$ is kept constant. Thus, the torque developed by the machine could be controlled by acting on the slip pulsation ω_2. The closed-loop scalar control using a PI regulator can be modeled as in fig.22:

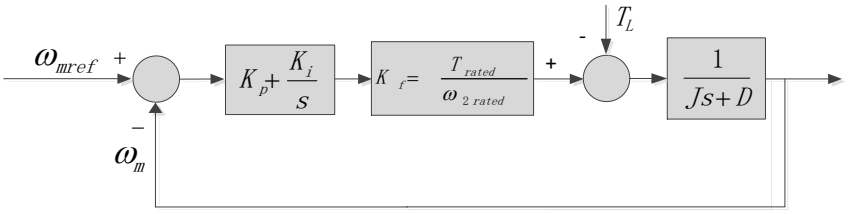

Figure 22 Block diagram of the improved scalar drive

where *J* is the inertia of the motor and *D* is the friction coefficient The open loop transfer function of the machine under constant $|E_s|/\omega$, assuming load torque $T_L=0$, is then given by the transfer function of the mechanic equation of the motor

$$G(s) = \frac{K_f}{Js + D} \qquad (4.3)$$

Where $K_f = \frac{T_{rated}}{\omega_{2rated}}$.

The design of the PI is therefore a simple exercise of compensation for linear system and any traditional compensator design technique can be used.

4.6 Reversible Heat Pump Control: Variable-Speed Control:

Cooling Mode

For the simplicity in implementation and the nature of the overall system, a scaler control is used to control the IM. The scaler control used a simple “voltage over frequency V/F” technique to control an IM at variable speeds. As shown in Fig.23, a Proportional and Integral (PI) temperature controller provides a reference value of speed for the V/F control based on the difference between the measured supply water temperature and the desired value. Due to simplicity of this control

technique, large operational window can be considered without problems of computational efforts. Indeed, the complexity greatly reduced only a speed loop PI is sufficient. Space vector modulation (SVM) [109] is used to acquire the Duty cycles for each of the inverter switching devices. Then, the Voltage Source Inverter (VSI) provides the three-phase voltage input to the IM.

In the HP block, the thermodynamic model of an HP that is discussed in the method section is implemented in conjunction with V/F control to realise a Variable-Speed Drive (VFD) for an HP. This scheme can be implemented in software, such as in MATLAB Simulink, to efficiently control the water supply temperature of the HP. The proposed control architecture assumes a reference water supply temperature $T_{ws,ref}$ whose values varies according to the HP operating mode is met by modulating CMP speed. In heating, $T_{ws,ref}$ is typically equal to 45-50 °C, and in cooling mode it is usually set to 7°C.

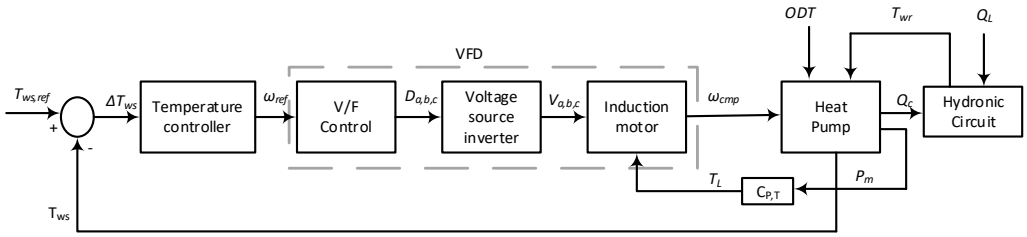

Figure 23 Control Architecture for a variable-speed RHP

In Figure 24, the control architecture for a variable-speed air-cooled chiller is shown. In this case, the CMP rotating speed (provided by the IM) is modulated through the action of the VFD (indicated by the grey black box in Fig. 23). For the simplicity in implementation and nature of the overall system, a scaler control is used inside the VFD. More specifically, the scaler control uses a simple "voltage over frequency V/F" technique to control an IM at variable speeds. More details on scaler control are provided in Appendix E. As shown in Fig. 23, a Proportional and Integral (PI) temperature controller provides a reference value of speed for the V/F control (i.e., ω_{ref}) based on the difference between the measured supply water temperature and the desired value (i.e., ΔT_{ws}). Then, based on ω_{ref} value, the V/F control provides the duty cycles, $D_{\mathrm{a,b,c}}$ for each of the inverter switching devices. Space vector modulation (SVM)[109] is used to acquire the duty cycles for each of the inverter switching devices. Finally, the Voltage Source Inverter (VSI) provides the three-phase voltage $V_{\mathrm{a,b,c}}$ input to the IM. In the "air-cooled chiller" block, the

aforementioned thermodynamic model of the chiller (see chapter 3) is implemented. The overall architecture can be solved in software, such as in MATLAB Simulink. Due to the simplicity of this control technique, large operational window can be considered without problems of computational efforts. The proposed control architecture assumes a $T_{ws,ref}$ equal to 7 °C.

Heating Mode:

Figure 23 depicts the main components of the control scheme for the case of variable-speed HPs. The CMP rotating speed (which is an output of the IM) is modulated thanks to the action of VFD. More specifically, a scaler control is used inside the VFD, where a simple "voltage over frequency V/F" technique is used to control an IM at variable speed. More insights into the scaler control are provided in [110]. A Proportional and Integral (PI) temperature controller provides the reference value of the speed to the V/F control (i.e., ω_{ref}). Such value is quantified based on the difference between the measured supply water temperature and the desired value (i.e., ΔT_{ws}). Then, as shown in the figure, the V/F control gives as output the duty cycles, $D_{a,b,c}$ to the Voltage Source Inverter (VSI). In this component, then, space vector modulation (SVM) is used to acquire the duty cycles, and the three-phase voltage $V_{a,b,c}$ are provided by the VSI to the IM [110].

4.7 Sequential control

Cooling Mode:

A control approach frequently used to modulate the delivered capacity of chillers is to cycle CMPs "ON" and "OFF" to maintain the water supply temperature (T_{ws}) around a desired value, as shown in Figure 3. In this case, CMP rotating speed has a unique nominal value, and it is not modulated as in the case of VFD. If more than one CMP is available, that is a very common practice to guarantee more flexible modulation of cooling capacity, a logic must be used to coordinate the ON-OFF cycle of each of them. Typically, a sequential approach (or sequential control SC) is adopted. For the sake of clarity, Figure 24 show a typical SC in the case of a chiller equipped with two CMPs. The black line represents the measured value of the water supply temperature.

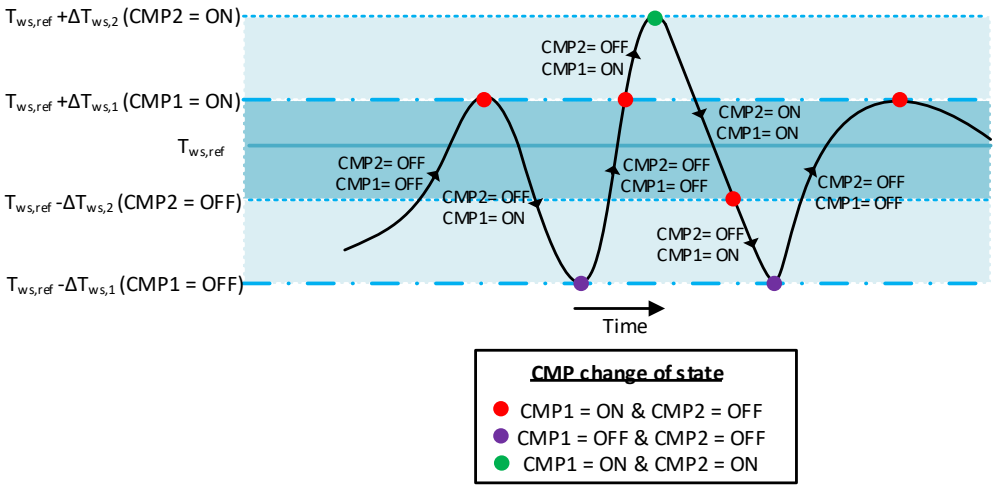

Figure 24 Sequential control for an air-cooled chillers equipped with two constant-speed CMPs.

The horizontal blue lines indicated by $T_{ws} \pm \Delta T_{ws,n}$ values represent the temperature threshold values for activating or deactivating each CMP. Low values for $\pm\Delta T_{ws,n}$ could lead to many ON-OFF cycles of each CMPs. Conversely, large values could lead to excessively high T_{ws} fluctuations. Hence, the values of $\pm\Delta T_{ws,n}$ are selected to assure a maximum number of "on-off" cycle in an hour, thus increasing the CMPs lifetime.

Figure 25 presents the architecture scheme for sequential control. A simple hysteresis controller can be used to implement the on-off sequence of each compressor, which is assigned to work in a range of $\pm\Delta T_{ws,n}$. Worth noting that the hysteresis controller for each compressor can be simulated by using the built-in block named "hysteresis comparator" available in MATLAB Simulink.

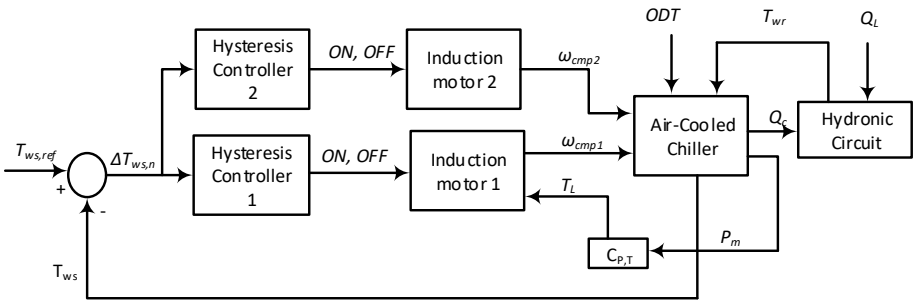

Figure 25 Architecture control for the sequential control strategy

Heating Mode:

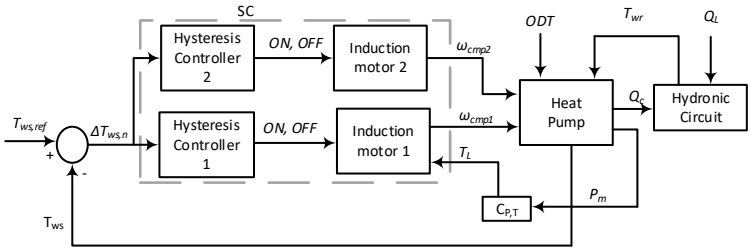

(a)

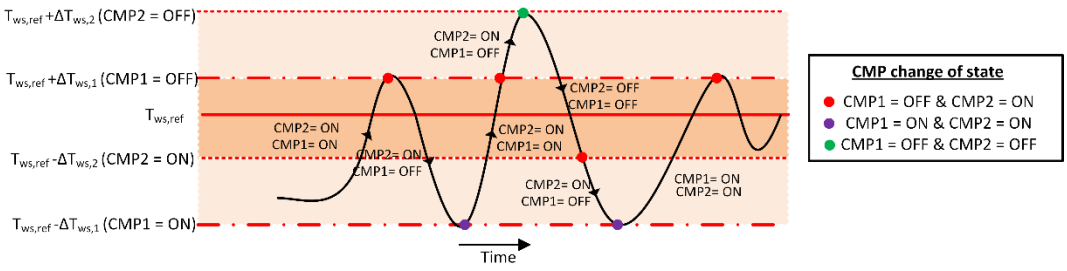

(b)

Figure 26 Figure 26 (a) Schematic of the control for a variable-speed air-to-water HP; (b) Activation control for an HP equipped with two constant-speed CMPs.

Details on the control scheme for HPs with constant-speed compressors. Figure26.a shows the scheme for the control of a constant speed HP equipped with multiple CMPs. More specifically, CMPs are "sequentially" activated or deactivated based on the difference between the measured water supply temperature and the desired value $\Delta T_{ws,n} = T_{ws} - T_{ws,ref}$. To better understand the sequential control logic (SC), it is worth referring to Figure 26.b. This figure depicts an SC in the case of an HP with two CMPs. The black line represents the time evolution of the measured value of the hot water supply temperature. The horizontal red lines indicated by $T_{ws} \pm \Delta T_{ws,n}$ values represent the temperature threshold values for cycling "ON" and "OFF" each CMP. It is apparent that the narrow band for $\pm\Delta T_{ws,n}$ could lead to many cycles of each CMPs. Conversely, a large band could be responsible for high T_{ws} variation, thus leading to occupants' discomfort. The values of $\pm\Delta T_{ws,n}$ are typically selected to assure a maximum number of "on-off" cycles in an hour below the limit recommended for CMP safety. As shown in Fig. 26.a, a hysteresis controller can be used for solving the ON-OFF cycle of each CMP.

4.8 Variable water-supply-temperature control strategy

Cooling Mode:

According to the declared goals of this work, the developed model is supposed to enable an assessment of the benefits that could be achieved when operating the HP with a variable water supply temperature, $T_{ws,ref}$, instead of a constant temperature. The use of a water supply temperature to the building variable with the *ODT* is typical in both HPs and gas boilers. In this respect, the possibility for the HP to operate with lower condensing pressures during "moderately" cold periods could lead to lower energy consumption and significantly higher COP values. In addition, the use of variable temperature setpoint is identified as a strategy for implementing DR programs in the building sector via HPs [111]. The variation of $T_{ws,ref}$ with *ODT* is usually presented in the form of a so-called "heating curve". These curves are supplied by manufacturers in the HPs' embedded control.

Before developing a heating curve for the considered HP, a preliminary assessment of the effects of a reduction in the hot water supply temperature on the sensible heating capacity of the fan coil was performed. This analysis relied on the model implemented in TRNSYS v. 17 [112] through Type 600a and validated, in the framework of this work, using data from different fan coil manufacturers [113]. Figure 27.a plots the fan coil's sensible capacity vs. the hot water temperature supplied. As shown, the T_{ws} varied in the range of 35.0-50.0 °C. Note that when the temperature of the supplied water decreases from 50°C to 35 °C, about a 50% reduction in the heating capacity of the fan coil is observed. Although a heavy reduction of fan coil capacity is consequent, the assumption of a variable supply water temperature of hot water over the 35.0-50.0 °C range with increasing ODT sounds reasonable. Indeed, in the case of higher ODT values, a reduction of the user's heating demand is expected due to lower heat loss from the indoor to the outdoor environment. Then the fan coils should satisfy a lower demand. In Fig. 27.b, a heating curve of the HP is shown. A linear change in $T_{ws,ref}$ vs ODT is assumed. In particular, a $T_{ws,ref}$ is always maintained at 50 °C for ODT values lower than 30 °C. A linear decrease down to 35 °C is assumed as ODT gradually increases up to 15 °C; for ODT value greater than 15 °C, $T_{ws,ref}$ is equal to 35 °C.

Before ending, it is worth stressing that, for the sake of brevity, this strategy will be applied only for the variable-speed HP.

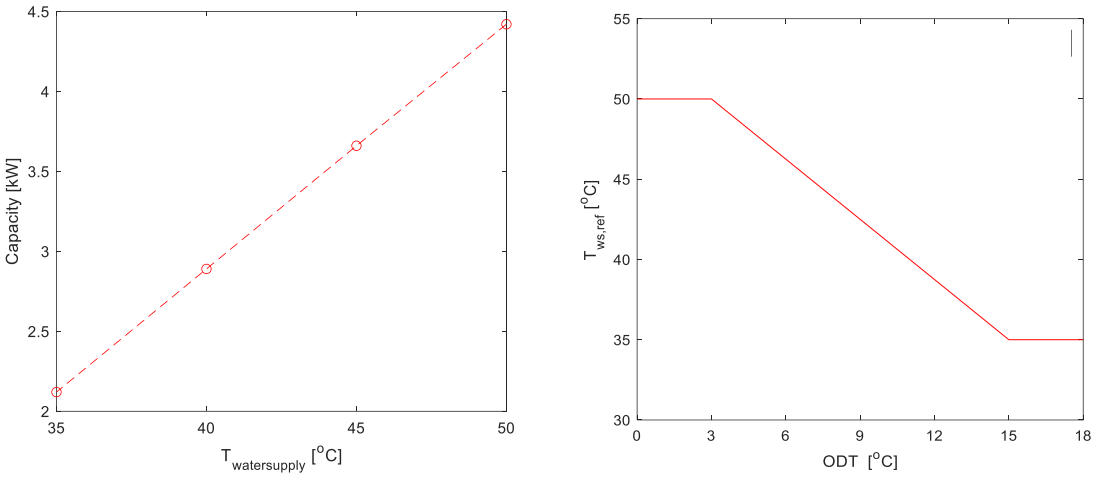

(A) *(B)*

Figure 27 (a) Sensitivity of fan coil's heating capacity to the supplied water temperature and (b) supply hot water temperature set point vs. ODT.

Heating mode:

In order to simulate the effect of a control strategies aimed at increasing the energy efficiency of the chiller or providing ancillary services to the grid (under the current scenarios of growing interest for smart grids, where active role in grid-balancing is often played by customers), the possibility to operate the chiller not at a constant Tws,ref, but rather at a sliding Tws,ref (this temperature depending on the ODT value) was investigated. Worth noting that Tws,ref is usually set to 7 °C regardless of the ODT value. The use of sliding water supply temperatures (variable with the ODT) is very common in hydronic heating, but rarely adopted in space cooling despite its significant energy saving potential, related to the possibility for the chiller to operate with higher evaporation pressures during moderately warm periods, finally resulting in a higher EER. The reason for this scarce use of sliding water supply temperatures in hydronic cooling obviously lies in the risk to lose control of indoor relative humidity. Depending on the type of HVAC equipment supplied (e.g., fan coils, cooling coils in air handling units, etc.), in fact, the water inlet temperature is the crucial parameter to guarantee the required moisture removal from the treated air. Then, a preliminary assessment of the effects of chilled water supply temperature on the dehumidification capacity of coils was developed, based on the model proposed by Braun[114] and designed for a

reference cooling coil consisting of three rows, eight tubes per row (typical configuration for commercial fan-coils). The analysis was aimed at assessing the changes in the Sensible Heat Ratio (SHR) of the coil when it is supplied by a chilled water at different temperatures and constant flow rate. The results are shown in Fig. 28, with the cooling capacity and the SHR plotted vs. the chilled water temperature at coil inlet; the resulting trends were also validated against detailed performance data drawn from catalogs of commercial fan-coil systems. The Tws was varied in the range 7.0-12.0 °C and significant reductions in both the sensible and latent capacity at higher water temperatures were observed, as expected. However, since the latent capacity of the coil for Tws values above 10 °C is almost less than 50% compared to the value found at 7 °C, it is preferable to limit the supplied water temperature fluctuations to the 7.0-9.5 °C range (also indicated by the area in Fig. 29 not covered by the light blue rectangle) so that the dehumidification capacity of the coil is only moderately affected. In quantitative terms, when Tws increases from 7.0 to 9.5 °C, the sensible cooling capacity slightly decreases from 2.86 down to 2.55 kW (-10.8%) while the latent capacity decreases from 1.04 kW down to 0.81 kW (-22.12%). Consequently, the SHR passes from 0.73 at 7 °C up to 0.8 at 9.5 °C, with a moderate 8.75% increase that sounds acceptable for most of space cooling applications, whenever very strict control of indoor relative humidity is not required.

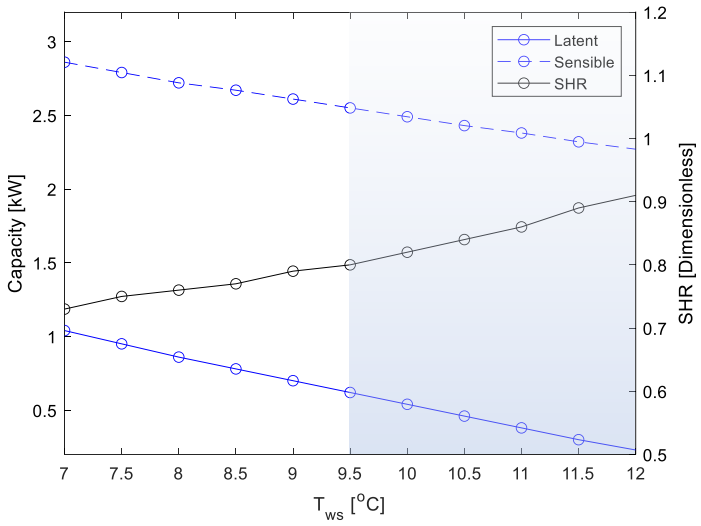

Figure 28 Sensitivity of coil capacity and SHR to the inlet temperature of chilled water.

Based on the above results, the assumption of a sliding supply temperature of chilled water over the 7.0-9.5°C range sounds technically feasible, and the performance of the chiller at such conditions is worth of investigation to assess the potential benefits in terms of energy saving.

Below in the paper, a linear change in the temperature of the supplied chilled water vs. the outdoor temperature is assumed, as shown in Fig. 29. In particular, while a 7 °C Tws,ref was maintained constant for ODT higher than 30°C, a linear increase up to 9.5°C was assumed for ODTs gradually decreasing down to 24°C; below this outdoor temperature, Tws,ref was maintained constant.

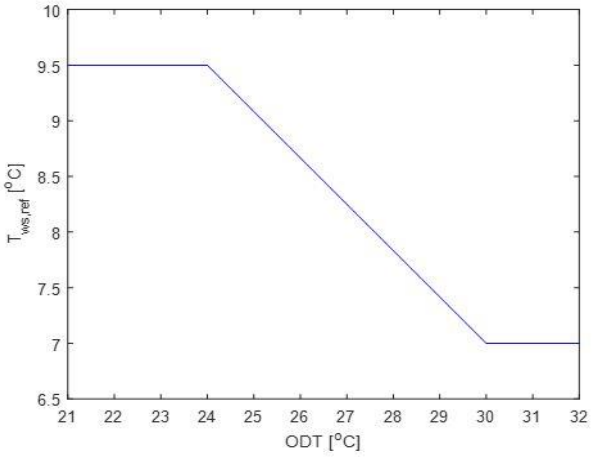

Figure 29 Variable set-point for the supply temperature of chilled water vs. ODT.

Summary:

Chapter 4, gives a detailed overview on control techniques that have been applied to control of motor drives. For simplicity and reduced complexity, scalar open loop and closed loop are developed instead of FOC. The basics of controller design are presented, and the variable speed and constant speed techniques are highlighted with overall RHP control techniques. Finally, RHP variable set-point temperature control methodology is also presented. Appendix 5 presents the scalar control scheme that has been implemented.

Chapter 5

Fault Diagnosis

Objective:

- Implement fault model of RVSD for fouling.
- Implement fault model of RVSD for charge capacity failure.
- Implement a control technique to improve performance.

5.1 Overview

Air-to-Water Reversible Heat Pump (RHP) is now widely diffused into the commercial and residential sectors, due to its easy installation and relatively low cost compared to available counterparts, much attention in recent years has been devoted to this technology[115]. The implementation of new policies for resorting to renewable energy to reduce greenhouse emissions and achieve the ever-increasing heating and cooling demand [81], [116]. Over the decades, immense research has been directed towards improving the energy efficiency of air source heat pumps [115], [117], [118]. Immense focus is shown towards advanced control techniques to aid in control and management of chiller technologies. Control techniques that have been deployed in recent studies to heat-pumps include; constant-speed and Variable speed drive with variable water supply temperature[81], [82], Constant-speed is the traditional control technique used to control a heat-pump for cooling and heating applications. Initially, the heat-pump was made-up of only constant speed motors. i.e. the compressor for heat-pump, water-pump and the outdoor fans. Operation at a constant speed is accompanied by an ON-OFF architecture to attain capacity control[119]. Variable-speed drives upon introduction into the local market acclaimed much credit simply due to its higher energy saving at partial loading and save up to 18% compared to constant-speed drives[49], [120], [121]. Both the control techniques are deployed to control a single heat pump, however when the number of heat pumps are increased and depending on the configuration additional control action is required to effectively achieve capacity control.

Immense research work is dedicated to individual components of the heat-pump. i.e. condensation heat recovery for domestic hot water[115], Artificial neural networks (ANN) for optimization of condenser water temperature set-point in a chilled water system[122], [123], Predictive control for optimization of chiller efficiency[124] and plant water-side economizer[125]. Numerous research

articles are available on ways to improve the RHP in the premanufacturing stage, by means of improved control techniques[49], [121], [126] and enhancements or redesigning at component level[127], [128], [129], [130], [131]. Although there is still room for improvements in the RHP technology, it is important to highlight the fact that as of this year, thousands of plants are already installed in various parts of the globe. To improve or maintain the energy efficiency of an installed RHP, the key indicator is to ensure that daily operation is performed effectively. During the life time of a RHP the internal parameters and external factors that govern the Coefficient of Performance (COP) tend to deteriorate and could eventually result into poor efficiency. As a matter of fact, it is vital to understand the types of faults and the nature of faults encountered by a RHP system.

In most cases the energy efficiency is compromised during various fault conditions resulting in slightly or negligible occupant discomfort. The faults that occur in a vapour compression VHP are classified as: a) hard faults, also referred to as catastrophic failures- the nature of such faults is largely undetermined and result in overall stoppage of RHP and component replacement might be a solution to resume operations [132], [133]; b) soft faults, also known as evolutionary faults- such faults affects the performance of system and degrades over time resulting from initial parameter variations or external factors[133], [134]. Due to the evolutionary nature of soft faults it important to study and understand the known faults. The soft faults are further divided into system and component faults. In Literature system faults has also been revered to as service faults[135]. The most common type of system faults for heat pumps are non-condensable gases (NCG) in the refrigerant, refrigerant over (RO) and undercharge (RU).

5.2 Modelling: Fouling

Soft faults related to mechanical components of an RHP are collectively known as component faults (CF). CFs comprises of Heat exchanger faults, liquid line restriction, compressor faults, 4 way valve leakage in RHPs and check value leakage in RHPs. Firstly, heat exchanger faults accounts for both the evaporator and condenser due to the reversible nature of the HP. Heat exchangers are subjected to fouling or mechanical problems in fans or pumps depending on heat transfer fluid (air or water)[136], [137], [138]. Fouling on a heat exchanger with water source is caused by particulates and fibres that obstruct circulation internally. On the contrary, for air source heat exchanger fouling the phenomenon that accounts for undesirable accumulation of dirt, debris

on the external heat transfer surface [107]. Only in 14% of the cases it affects the indoor comfort levels, on the contrary it significantly affects the thermal capacity and COP of the plant [139], [140]. Compressor faults is regarded as one of the major faults in a RHP, most faults are either liquid slugging or overheating. Overheating directly affects the electrical motor connected to the compressor by gradually deteriorating the performance and finally resulting in failure. Liquid slugging is the major reason of leakage of the compressor valve. Both the faults are a consequence of other related faults in a RHP, hence it can be detected and mitigated. As a consequence the compressor faults and electrical motor failures in general can be prevented, provided contributing faults are identified and rectified in a given time frame[134], [141]. Other related component faults are not in the scope of study for this research article due to the nature of the faults and simulation constraints on inducing such faults. Soft faults compared to catastrophic faults are hard to detect due to the evolutionary nature of the faults. Although the system efficiency and consumption are compromised it can be undetected at times. Henceforth, it is important to understand and implement techniques to detect such faults in order to be mitigated. Techniques to detect various types of faults based on parameter estimation is vital in understanding the overall behaviour and functionality of the RHP. Since, it is exposed to various outdoor conditions degradation and faults are imminent. As a result of induced faults, the plant parameters are bound to change and devising an approach to detect these parameter variations is vital.

5.3 Refrigerant charge

RU occurs due to leakages or improper installations or maintenance [142]. Impacts of RU significantly affect the compressor power and thermal capacity and it is evident in steady state operations of RHP[143]. Refrigerant leakage in a chiller plant reduces the mass and depending on the intensity of the lost refrigerant action will be needed. A loss of charge that is less than 20% the resulting effect is regarded as negligible[144]. It affects largely the thermal capacity by reducing the range of outdoor operating conditions[145]. RO befalls once mass of refrigerant is higher than the manufacturers' specification, lead cause of RO is improper commissioning practices[143], it increases the liquid refrigerant and reduced the lifespan of the compressor. For both the cases a thermostatic expansion valve is used to reduce the sensitivity to low charge and liquid slugging[108], [146], [147]. NCG consists mostly of air and nitrogen affect significantly the performance of the RHP, however, such a fault arises either from incompetence in during servicing

or initial installations[148], [149]. Hence, system faults can be largely avoided provided the servicing and installation procedures are carried out appropriately.

5.4 Control architecture for variable-speed air-cooled chillers

In Figure 30, the control architecture for a variable-speed air-cooled chiller is shown. In this case, the CMP rotating speed (provided by the IM) is modulated through the action of the VFD (indicated by the grey-dotted box in Fig. 30). For the simplicity in implementation and nature of the overall system, a scaler control is used inside the VFD. More specifically, the scaler control uses a simple "voltage over frequency V/F" technique to control an IM at variable speeds. As shown in Fig. 30, a Proportional and Integral (PI) temperature controller provides a reference value of speed for the V/F control (i.e., ω_{ref}) based on the difference between the measured supply water temperature and the desired value (i.e., ΔT_{ws}). Then, based on ω_{ref} value, the V/F control provides the duty cycles, $D_{\text{a,b,c}}$ for each of the inverter switching devices. Space vector modulation (SVM) is used to acquire the duty cycles for each of the inverter switching devices. Finally, the Voltage Source Inverter (VSI) provides the three-phase voltage $V_{\text{a,b,c}}$ input to the IM.

In the "air-cooled chiller" block, the thermodynamic model of the chiller (see chapter 3) is implemented. The overall architecture can be solved in software, such as MATLAB Simulink. Due to the simplicity of this control technique, a large operational window can be considered without the problems of computational efforts. The proposed control architecture assumes a $T_{\text{ws,ref}}$ equal to 7 °C.

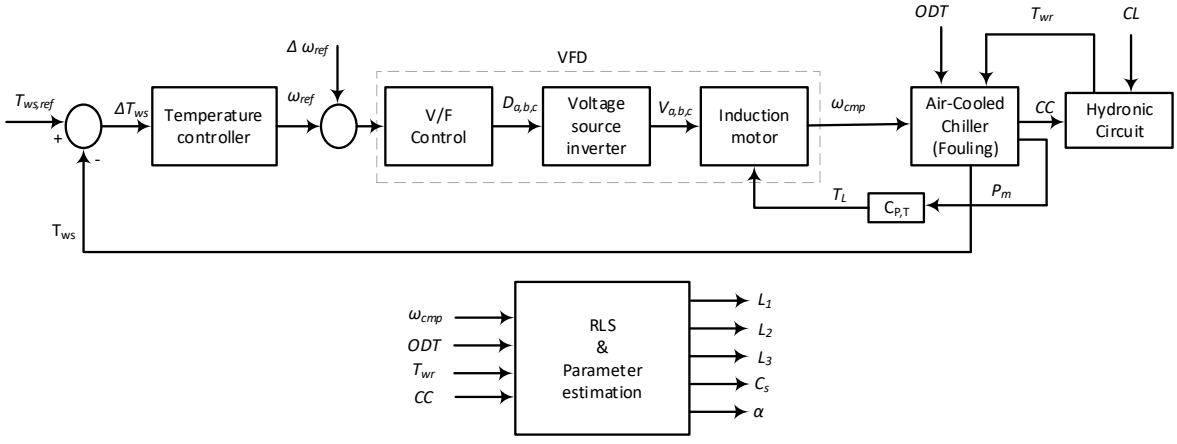

Figure 30RLS Scheme

5.5 Online Estimation of Cooling Capacity and Hydraulic loop Parameters using Recursive-Least Squares (RLS):

This section will present the implementation of RLS techniques to a RHP for Parameter estimation purposes. Considering the Eqn.3.17 and Eqn.3.18 of the air-to-water HP, the expression of the T_{ws} at any instance can be written in discrete form:

$$CC(\mathrm{k}+1) = \alpha_1 CC(k) + \alpha_2 \omega_{CMP}(\mathrm{k}) + \alpha_3 ODT(k) + \alpha_4 T_{wr}(k) \tag{5.1}$$

Taking the Euler difference discretization for eqn3.2, note $\frac{dT_{wr}}{dt} = \dot{T_{wr}}(k)$:

$$T_{wr}(\mathrm{k}+1) = \beta_1 T_{wr}(\mathrm{k}) + \beta_2(\mathrm{CC(k)} - \mathrm{CL(k)}) \tag{5.2}$$

From Eqn.5.1 and 5.2 we obtain:

$$\alpha_1 = (1 - \alpha T_s) \tag{5.3}$$
$$\alpha_2 = T_s L_1 \tag{5.4}$$
$$\alpha_3 = T_s L_2 \tag{5.5}$$
$$\alpha_4 = T_s L_3 \tag{5.6}$$
$$\beta_1 = 1 \tag{5.7}$$
$$\beta_2 = \frac{T_s}{C_s} \tag{5.8}$$

Given a time window of length N, this gives rise to a regressor of the form:

$$Ax \approx b \tag{5.9}$$

$$\begin{bmatrix} CC(\mathrm{k}-1) & \omega_{CMP}(k-1) & ODT(k-1) & T_{wr}(k-1) \\ CC(\mathrm{k}-2) & \omega_{CMP}(k-2) & ODT(k-2) & T_{wr}(k-2) \\ \vdots & \vdots & \vdots & \vdots \\ CC(\mathrm{k}-\mathrm{N}) & \omega_{CMP}(k-N) & ODT(k-N) & T_{wr}(k-N) \end{bmatrix} \begin{bmatrix} \alpha_1 \\ \alpha_2 \\ \alpha_3 \\ \alpha_4 \end{bmatrix} \approx \begin{bmatrix} CC(k) \\ \vdots \\ \mathrm{CC}(k-N-1) \end{bmatrix} \tag{5.10}$$

$$\begin{bmatrix} T_{wr}(k-1) & (\mathrm{CC(k-1)} - \mathrm{CL(k-1)}) \\ T_{wr}(k-2) & (\mathrm{CC(k-2)} - \mathrm{CL(k-2)}) \\ \vdots & \vdots \\ T_{wr}(k-N) & (\mathrm{CC(k-N)} - \mathrm{CL(k-N)}) \end{bmatrix} \begin{bmatrix} \beta_1 \\ \beta_2 \end{bmatrix} \approx \begin{bmatrix} T_{wr}(k) \\ \vdots \\ T_{wr}(k-N-1) \end{bmatrix} \tag{5.11}$$

with b being the actual value (measured) water supply temperature, x the unknown regressor value (weights of the network) and A is the known vector of measure speed, water return temperature and outdoor temperature over the N sample time window [150], [151]. With this information, a Recursive Least Square based estimator is used to calculate the unknown values for α_1,α_2, α_3, α_4, β_1, and β_2 as depicted in fig.31. Once the system is operation and a change in parameters are

estimated using the unknow vales and new unknown parameters are estimated or reconstructed using the parameter estimation block..

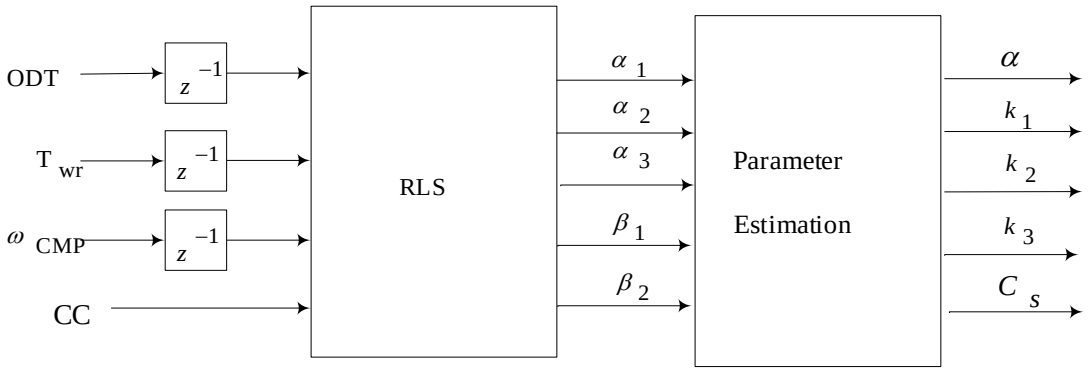

Figure 31 Weights estimation using RLS and Feed-forward controller

Since there are no poles, the controller is stable. The parameter estimation quantities are then created by using the corresponding unknown reference coefficient parameter α_1,α_2, α_3, α_4, β_1, and β_2 for the system model.

$$\alpha = \frac{1-\alpha_1}{T_s} \tag{5.12}$$

$$L_1 = \frac{\alpha_2}{T_s} \tag{5.13}$$

$$L_2 = \frac{\alpha_3}{T_s} \tag{5.14}$$

$$L_3 = \frac{\alpha_4}{T_s} \tag{5.15}$$

$$\beta_1 = 1 \tag{5.16}$$

$$C_s = \frac{T_s}{\beta_2} \tag{5.17}$$

Once the parameters of the RHP are obtained, any change in parameter due to condenser fouling, hydronic loop fluid loss and refrigerant charge loss are easy denoted. For cooling model operation eqn.19 is used to model the RHP for cooling mode operation, IMSTart software is used to generate the 20% fouling dataset. Upon which the new parameters are computed using appendix 4. A feedforward control technique is proposed to add a control action to compensate the overall plant performance during fault conditions. A generic expression can be diced from eqn.5.1 and a speed compensation technique is proposed.

$$\Delta\omega_{CMP}(\mathrm{k}) = \frac{1}{\alpha_2} CC(\mathrm{k}) - \frac{\alpha_1}{\alpha_2} CC(k) - \frac{\alpha_3}{\alpha_2} ODT(k) - \frac{\alpha_4}{\alpha_2} T_{wr}(k) \quad (5.18)$$

Upon implementing eqn.5.18 as a speed compensation technique it was noted the overall performance of the system can be enhanced to improve the EER of the overall system. As presented in fig.31 the $\Delta\omega_{CMP}$ is the additional control attraction in term of the speed response. Results for this section are presented in chapter 6.

Summary:

Chapter 5 is dedicated to parameter estimation and fault diagnosis. Initially, the RLS methodology is implemented to acquire the RHP parameters. In this chapter fault model of RHP for 20% condenser fouling and 10% charge capacity fault in cooling mode. Finally, an adaptive feedforward compensation on the compressor speed is added to improve performance during fault conditions.

Chapter 6

Results and Discussion

Overview:

Firstly, a brief introduction of the case study is presented. The system parameters are presented. Followed by the cooling mode and heating mode results

6.1 Case study: Cooling mode

An office building located in Palermo (Italy) was selected as a case study. Demand profiles were estimated using data available from energy audits performed in a previous study[152]. More specifically, two working days in the cooling period are here examined. One is characterized by a high cooling load day (i.e., around the end of July) and the other one by low cooling load day (i.e., around the half of June). In Figure 32.a-b, the values of ODT and cooling load are presented. Worth noting that, the dashed line is used for the profile in low-cooling load day, and the continuous line for the high-cooling load day. Focusing on the building load, it was assumed an operation for 9-hours during a day, (more specifically, from 8 am to 5 pm) with a variation of the load at 15 minutes. In addition, the ODT values in Figure 32.a varied on hourly basis and they came from meteorological dataset.

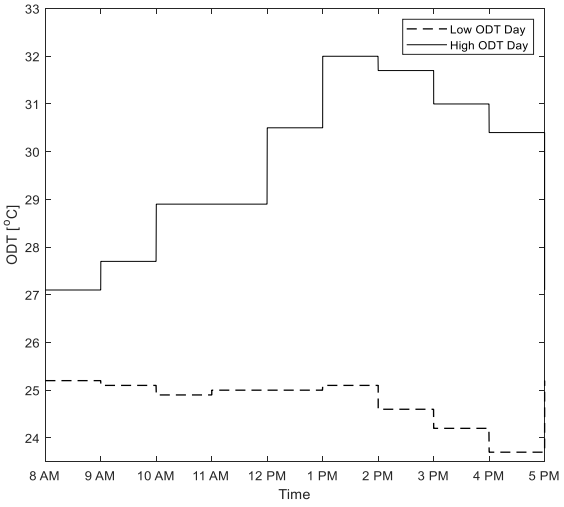

(a)

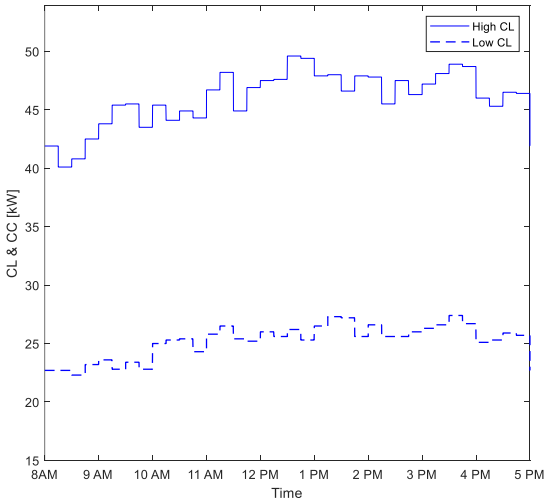

(b)

Figure 32 Daily profiles of low- and high-cooling load days: (a) ODT values, (b) cooling demand.

To evaluate the energy performance achieved by different control strategies of the chiller, the Energy Efficiency Ratio (EER) averaged on an hourly basis was used, defined in Eq. 6.1.

$$\mathrm{EER} = \frac{\int_0^{3600} CL(\tau)d\tau}{\int_0^{3600} P_e\,(\tau)d\tau} \tag{6.1}$$

The nominal capacity of the chiller was selected based on the peak value of the cooling demand, equal to around 50 kWc. In Table 6.1, the technical data of the refrigerant circuit and IM are shown. Note that these data were derived from commercial catalogues.

As shown in Table 6.1, the chiller is equipped with two scroll compressors. For the scope of this thesis of equal capacity, two control strategies for CMPs were considered:

- Variable-speed CMP (in the following indicated also as variable-speed chiller) according to which the speed of both CMPs is continuously varied between a minimum and a maximum value by the VFDs. More specifically, from a survey on commercially available scroll CMPs, the rotating speed ωCMP was assumed to vary between 1000 and 6200 rpm.
- ON-OFF CMPs with sequential control (in the following briefly indicated as constant-speed chiller) according to which CMPs speed is kept constant (typically, 2900 rpm) once switched ON, and the cooling load is satisfied by cycling ON-OFF the CMPs according to the sequential approach. Details on the performed simulations and preliminary modeling results.

The thermodynamic models of the air-cooled chillers were developed by using the IMST-Art software[153]. The tool implements 1-D thermohydraulic modeling of heat exchangers, refrigerant lines, and accessories, and its reliability has been proven by accurate validation against wide sets of experimental results [154]. To map the chiller's performance, different simulations were developed for both variable-speed and constant-speed chiller, based on the matrix test shown in Table 6.2. As it can be observed, ODT was varied over a wide range (from 22 up to 38 °C) to account for possible application of the same model in different climatic condition. More specifically, a step variation equal to "+2 °C" was assumed, leading to nine values to be simulated.

Table 6. 1Technical details on a 50 kWc reversible variable-speed air-to-water HP and electrical parameters of the induction motor.

With respect to the temperature of the water returning from the hydronic circuit, Twr, the range

Refrigerant Circuit		Induction Motor	
Refrigerant	R410a	Pn(kW)	10
Condenser Type	Fin and Tube	Rs (Ω)	0.8
Number of Condenser	1	Rr(Ω)	2.91
Condenser Fan Power [kW]	1.5	Ls(H)	0.21
Metering Device	Electronic Expansion Valve	Lr(H)	0.21
Evaporator Water Flowrate [m3/h]	7.0	Lm(H)	0.2
Evaporator Pump Power [kW]	2	J(kg.m2)	0.1
Compressor Type (and Number)	Scroll (2)	Σ	0.03
Compressor Power (each) [kW]	9.0	f(Hz)	50
Refrigerant Charge [kg]	14.3	P	2

8-14 °C was selected to account for different heating/cooling demands. For this variable, a variation step of "+2 °C" was assumed as well, leading to four Twr values to be simulated.

In the case of the variable-speed chiller, the rotating speed of each compressor was varied (both operating simultaneously) among 1000 and 6200 rpm, with a step equal to "+400 rpm" and fourteen ωCMP values had to be simulated). The number of simulation tests to be performed in IMST-Art were then obtained by combining the nine ODT values, the four Twr values and fourteen compressor speeds. It is easy to find that to fully characterize the variable-speed chiller operation 504 simulations test were needed.

Regarding the constant-speed chiller, the rotating speed of each compressor was set to 2900 rpm, as suggested by commercial catalogues. Simulations were first performed considering that only one CMP was operating. More specifically, by combining the nine ODT values and the four Twr values, 36 simulations were carried out. Then, the 36 tests were repeated considering both CMPs

activated. To fully characterize the operation of the constant speed-chiller, 72 simulations were needed.

Table 6. 2 Matrix test for the air-cooled chiller thermodynamic modelling.

Mode	Variable		Range	Change Step	
Cooling	ODT	[°C]	22-38	+2 °C	Variable-Speed CMPs ωCMP [rpm] 1000-6200 (+400 rpm)
	Tw,r	[°C]	8-14	+2 °C	ON-OFF CMPs ωCMP [rpm] 2900 (-)

Once simulations were performed, the linear coefficients of Eqs 3.1. a-b were obtained by using the Least-Square technique as detailed in Appendix 4. In Table 6.3, the coefficients for the mechanical power (Pm) and delivered capacity are shown for the variable-speed chiller. In Table 6.4, results for the constant-speed chiller are shown.

Table 6. 3 Preliminary modelling results: variable-speed chiller.

	Delivered Capacity			Absorbed Power		
VS-Cooling	L1	0.0086	RMSE [kW]: 2.26 NRMSE [%]: 3.91	K1	0.0037	RMSE [kW]: 1.41 NRMSE [%]: 5.91
	L2	-0.32		K2	0.05	
	L3	1.55		K3	-0.26	

Worth noting that to evaluate the error-index of the realized model in comparison to the thermodynamic data, the Normalized Root Mean Square Error Index (NRMSE) was used. Since

the NRMSE values in Table 6.4 is always less than 5% a good approximation of simulation data is achieved by the proposed model.

Table 6. 4 Preliminary modelling results: constant-speed chiller.

	Delivered Capacity One CMP-ON			Absorbed Power One CMP- ON		
CS-Cooling	L1 L2 L3	0.012 0.97 -0.38	RMSE [kW]: 0.15 NRMSE [%]: 1.15	K1 K2 K3	0.00075 0.16 0.018	RMSE [kW]: 0.03 NRMSE [%]: 0.98
	Delivered Capacity Two CMPs-ON			Absorbed Power Two CMPs- ON		
	L1 L2 L3	0.01956 1.5811 -0.6194	RMSE [kW]: 0.30 NRMSE [%]: 1.16	K1 K2 K3	0.001785 0.3808 0.04284	RMSE [kW]: 0.30 NRMSE [%]: 1.17

Implementation of the integrated control scheme and main assumptions for the analysis

The overall schemes for sequential control and variable speed drive were implemented in MATLAB Simulink. Since the simulation considered the full day operation of the HP (operated in chiller mode), a sample time equal to 0.01 s (quite large, compared to the typical values adopted for VFDs' modeling) is used to reduce the data-point.

The variable-speed chiller was controlled by assuming a 7 °C setpoint value for the supply water temperature. The tuning on the PI parameters in the Temperature Controller (see Fig. 23) was performed via MATLAB Sisotool command[109]. By fixing a settling time of 10 minutes, the command provides the values of the proportional and integral gains to the users.

Regarding the constant-speed chiller with sequential control, a 7 °C value for the Tws, ref. was assumed. However, as previously explained, appropriate temperature bands are required to avoid rapid cycling (i.e., too many cycling) of CMPs. For this case, the selected temperature bands are detailed in Table 6.5.

Table 6. 5 Bands definitions for CMPs cycling in sequential control.

Changes in CMP State	Threshold values
CMP 1: ON, CMP 2: ON	$T_{ws,CMP2\_ON} = 8.0\,°C$ (ΔT_{ws}= +1.0 °C)
CMP 1: ON, CMP 2: OFF	$T_{ws,CMP1\_ON} = 7.5\,°C$ (ΔT_{ws}= +0.5 °C)
CMP 1: ON, CMP 2: OFF	$T_{ws,CMP2\_OFF} = 6.5\,°C$ ($\Delta T_{ws} = -0.5\,°C$)
CMP 1: OFF, CMP 2: OFF	$T_{ws,CMP1\_OFF} = 6.0\,°C$ ($\Delta T_{ws} = -1.0\,°C$)

6.2 Results and Discussion for cooling mode

Simulation results for the variable-speed and constant-speed chiller are first shown. Results from sensitivity analysis to account for the effect of the hydronic circuit are shown. In the last subsection, results for the flexible operation of the chiller are presented.

Variable-speed air-cooled chiller

Figures 33.a-e show results for the variable-speed chiller operation in the high cooling load day. Note that, for the sake of brevity, in this case high cooling load day results are shown. However, the considerations here made could be extended to the low cooling day as well. In Fig. 33.a, the delivered cooling capacity (blue dashed line) is presented along with the cooling load profile (blue continuous line). Looking at the cooling capacity profile, it is worth noting that the chiller is constantly trying to match the cooling load. As it can be observed from the zooming at 11-12 am in Figure 33.a, the cooling capacity has as an oscillating trend at each change in the load due to the action of the PI controller. Figure 33.b shows the temperature of the water supplied to the building. Worth noting that Tws is maintained almost at 7 °C (the assumed setpoint) thanks to the

controller. Some oscillations are present each 15 minutes due to the changes in cooling load. In Fig. 33.b, the rotating speed of the CMPs is also shown. This variable is continuously manipulated by the controller to meet the water supply temperature setpoint. In, Fig. 33.c the electromagnetic torque produced by the IM and the air-cooled chiller load torque are plotted. Since both curves are perfectly overlapped, it follows that a dynamic equilibrium is achieved between the CMP and the IM during chiller's operation. Fig. 33.d shows the sum of the mechanical power supplied by both the IMs to the CMP. In Fig. 33.e, the absorbed RMS current by the IMs is plotted. Minimal fluctuations on rms currents during daily operation on the IM. As a result, the measured value is always close to 8.2 A. The initial spike accounts for the inrush current to magnetize the IM. Fig. 33.f shows the average EER values calculated according to Eq. 6.1. The EER ranges between 3.43 and 3.08 during the operation due to combined effect of part-load operation and ODT values.

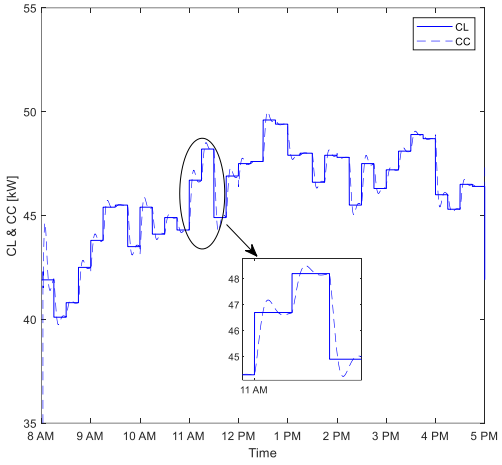

(a)

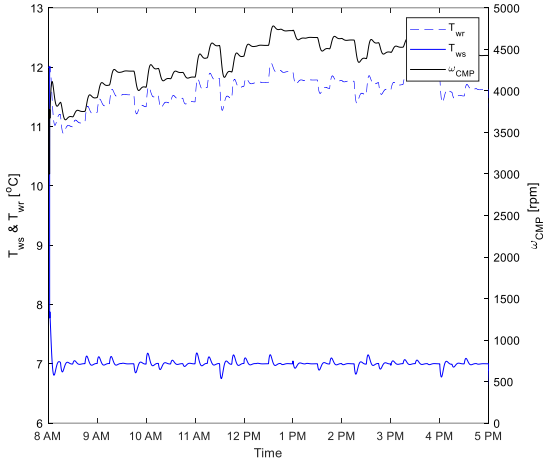

(b)

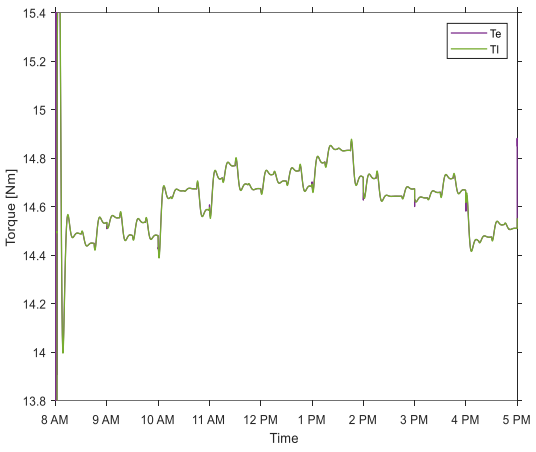

(c)

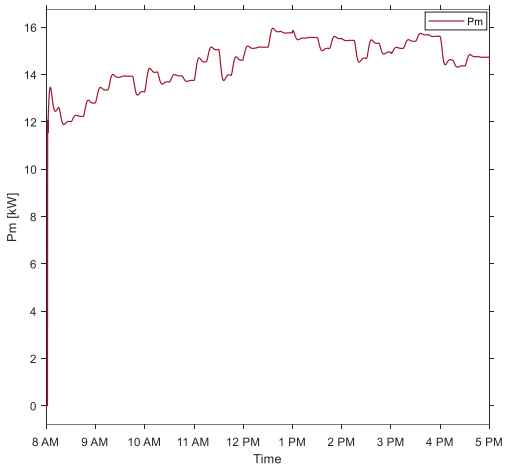

(d)

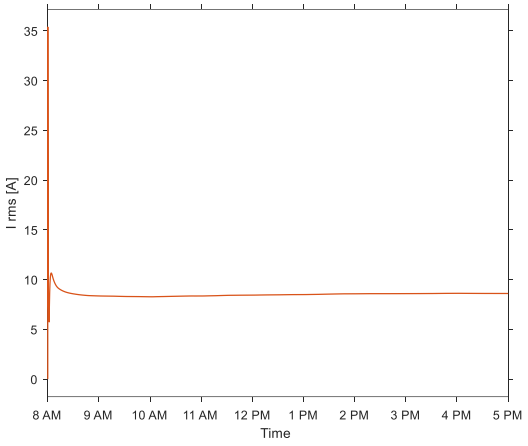

(e)

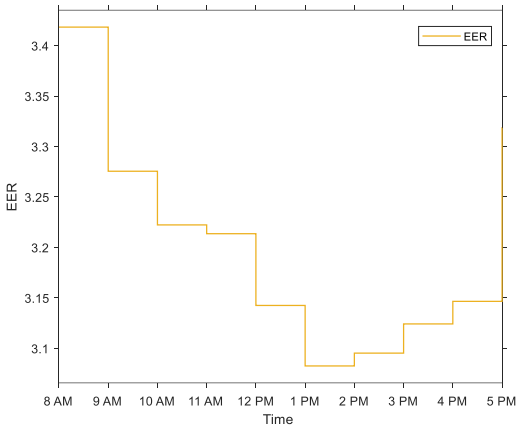

(f)

Figure 33 Variable-speed results: (a) Cooling Load and Cooling Capacity (b) Water supply temperature, Water return temperature, and Compressor speed, (c) Mechanic and electromagnetic torque, (d) Mechanical Power, (e) Absorbed Current, (f) EER values.

Constant-speed air-cooled chiller

Figures 34.a-d show the results obtained from simulations for constant-speed air-cooled chiller for the high cooling load day in Palermo. In Fig. 34.a the cooling demand profile (blue continuous line) is shown together with the capacity delivered by the chiller. Moreover, the minimum CC is never zero, since one compressor (more specifically CMP1) is always operating. In this respect, as shown in Fig 34.b, the value of ωCMP1 is always 2900 rpm (red line), conversely ωCMP2

changes from 0 or 2900 rpm, according to the cycling (black line). Moreover, the temperature of the water supplied to the building is oscillating around the value of 7.25 °C value (black dashed line). In Fig. 34.c-d a zooming on two hours in the high cooling load day day is shown. More specifically, Fig. 34.c plots the CMPs operation from 8 to 9 am, when the lowest cooling demand is observed during the day. Fig. 34.d focus from 11 to 12 am. CMP 1 is always operating, since in this day the minimum cooling load value (which is observed from 8 am to 9 am) is higher than the minimum capacity provided by the chiller with only one CMP operating. Conversely, CMP2 is continuously cycling ON-OFF to match the cooling load. More specifically, from 8 to 9 am CMP2 is cycling ON-OFF almost 17 times, which is higher than the maximum threshold value equal to 12 suggested by the manufacturer. From 11 to 12 am, CMP2 is cycling 19 times. In Figure 34.e, the mechanical power required by the CMPs is plotted. As expected, it is never equal to zero since CMP 1 is always ON. Fig. 34.f shows the average hourly EER values. The EER ranges between 3.29 and 2.85 during the operation due to combined effect of part-load operation and different ODT values.

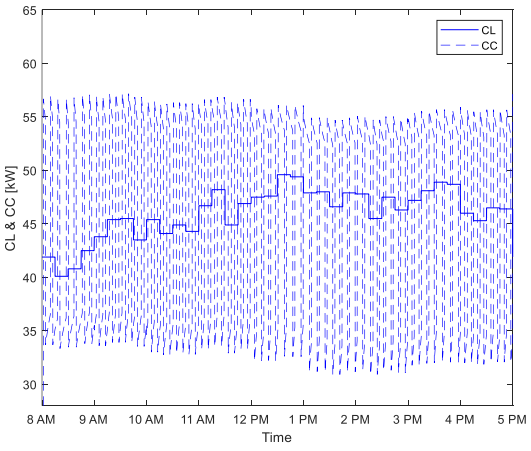

(a)

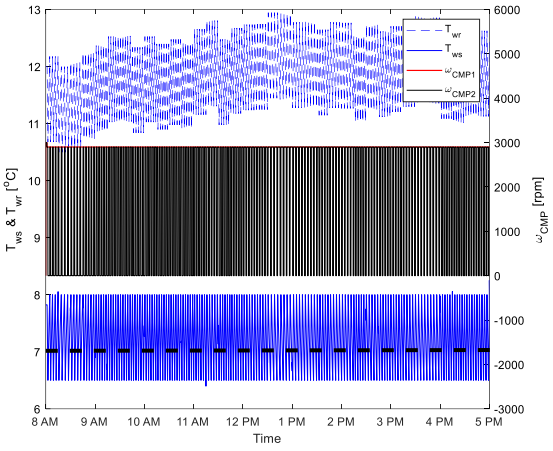

(b)

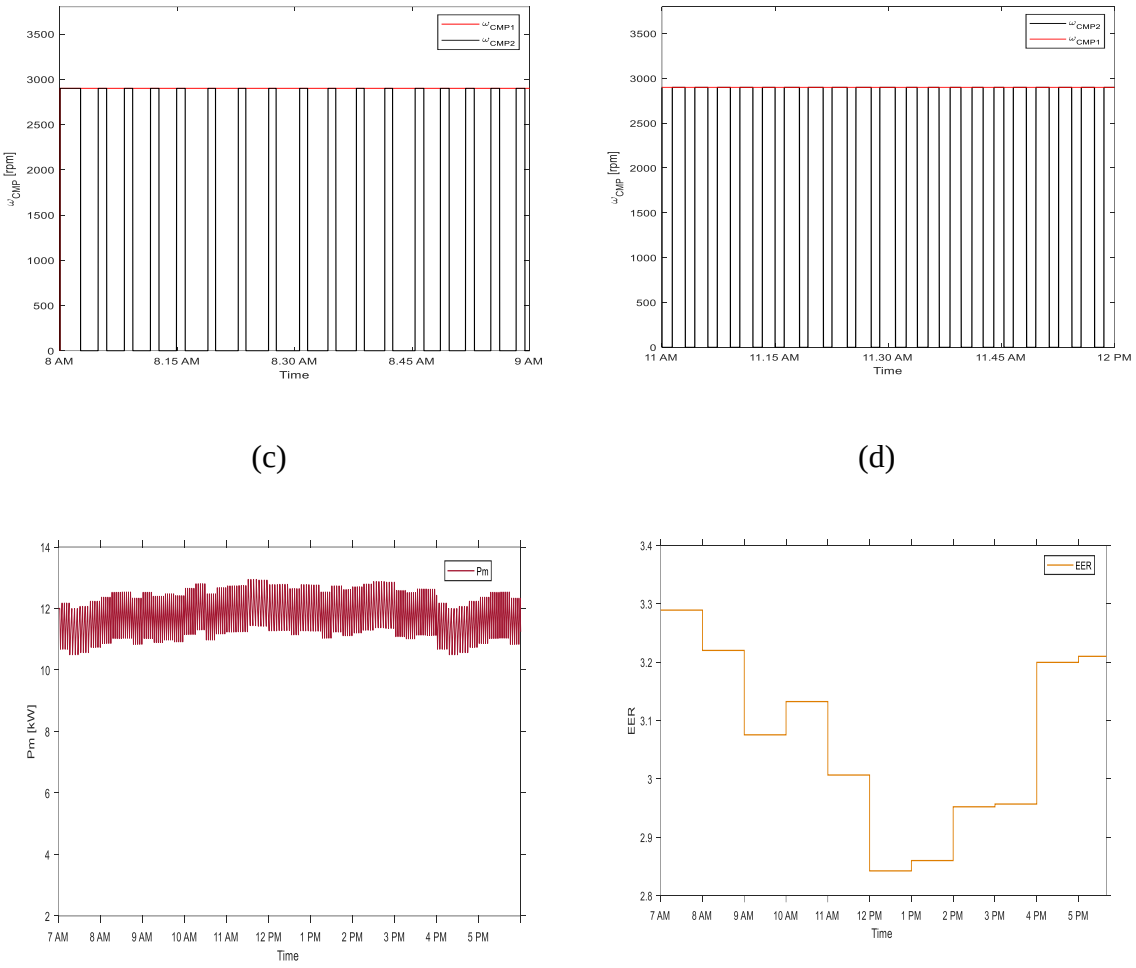

Figure 34 Sequential Control results for high-cooling load day: (a) Cooling Load and Cooling Capacity (b) Water supply, Water return temperature and CMPs speed, (c) CMPs speed from 8-9 am, (d) CMPs speed from 11-12 am, (e)Mechanical Power, and (d) EER.

Figures 35.a-d show the results obtained from simulations for a constant-speed air-cooled chiller in the low-cooling day in Palermo. As shown in Fig. 35.a, compared to Fig. 35.a, the minimum delivered CC is zero, meaning that the unit is completely OFF during the day. As shown in Fig 35.b, the value of ωCMP2 is always zero (black line), conversely ωCMP1 changes from 0 to 2900 rpm, according to the cycling (red line). Moreover, the temperature of the water supplied to the building is oscillating around the value of 6.75 °C value (black dashed line). In Fig. 35-c-d a zooming on the low load (8-9 am) and high (11-12 am) hours of this day is shown. More

specifically, Fig. 35.c plots the CMPs operation from 8 to 9 am. CMP 2 is ON only for some minutes at the very beginning of the selected hours due to the start-up of the plant. Then, CMP 2 is OFF for all the remaining working hours in the day, since the maximum cooling load value (observed from 1 to 2 pm) is lower than the minimum capacity provided by the chiller with two CMPs operating. Conversely, CMP1 is continuously cycling ON-OFF to match the cooling load. More specifically, as shown in Fig. 35.d, from 8 to 9 am CMP 1 is cycling ON-OFF almost 25 times, which is higher than the maximum threshold value equal to 12. From 11 to 12 am, CMP1 is cycling 21 times. In Figure 35.e the mechanical power required by the CMPs is plotted. As expected, its minimum value is zero in those moments where the unit is OFF. Fig. 35.f shows the average hourly EER values. The EER ranges between 2.96 and 3.27 during the operation due to combined effect of part-load operation and different ODT values.

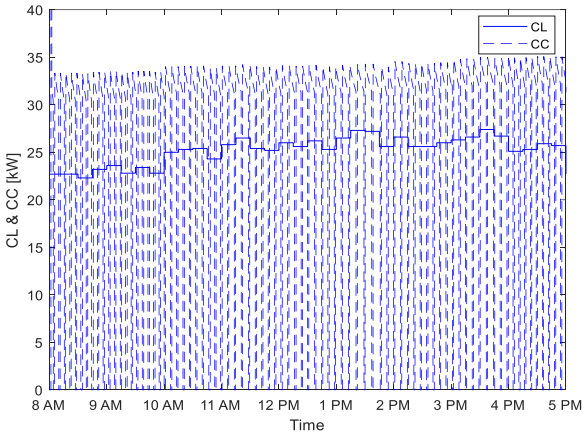

(a)

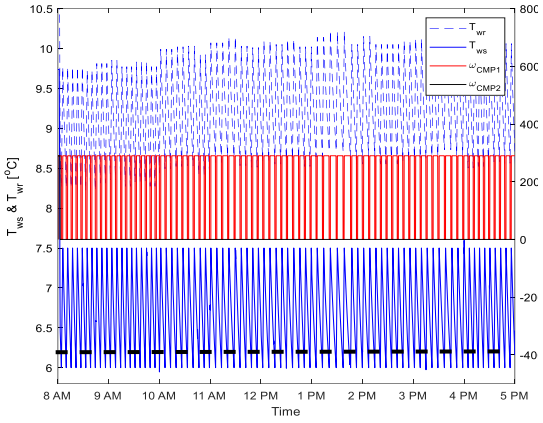

(b)

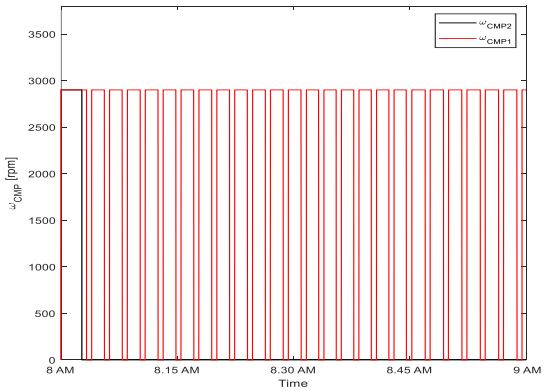

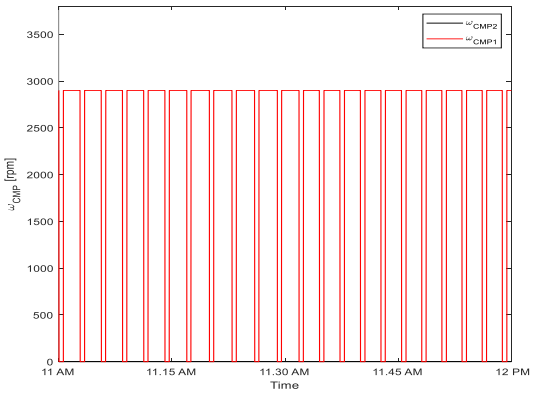

(c) (d)

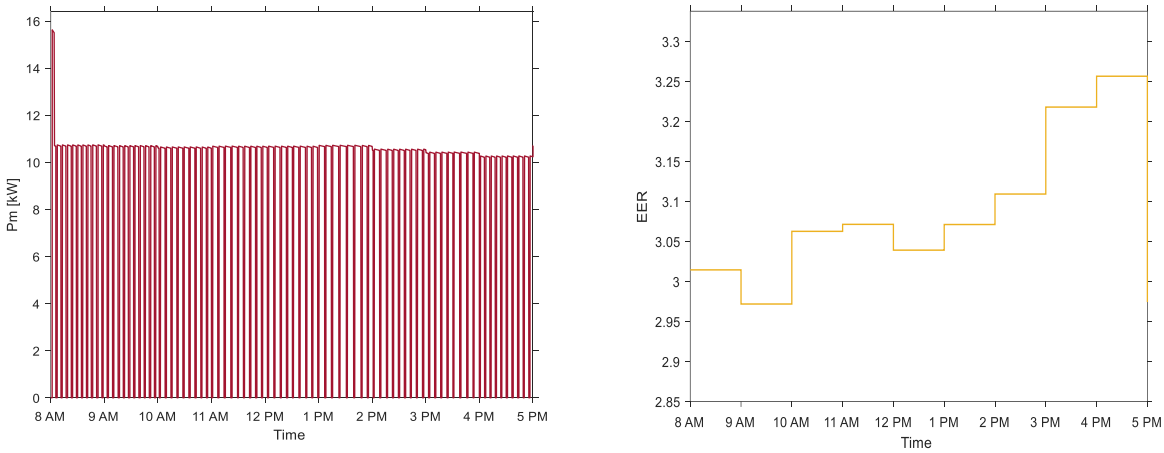

(e) (f)

Figure 35 Sequential Control results for low-cooling load day: (a) Cooling Load and Cooling Capacity (b) Water supply, Water return temperature and CMPs speed, (c) CMPs speed from 8-9 am, (d) CMPs speed from 11-12 am, (e) Mechanical Power, and (d) EER.

Sensitivity analysis with the design of the hydraulic loop

In the previous section, simulations were performed assuming a C_s value equal to 600 kJ/°C. It is worth investigating the effect of different Cs values on the controller actions and overall energy performance. As explained, this parameter accounts for the water content in the hydronic loop (i.e., the thermal inertia). However, it is worth investigating the effects of different Cs values which could arise either from a need to have higher inertia for assuring safe CMP operation, or due to a wrong design of the hydraulic loop. Then, simulations were performed considering the following Cs values: C_s=500 -1000-1500 -2000 kJ/°C

Results for the case of variable speed HP are presented in Figure 36. Fig.36.a-b presents the water supply temperature for all the Cs values at 8-9 am. Note that for the sake of clarity, only data for two hours, i.e., 8-9 am and 11-12 am are here presented for the high-cooling load (Fig 36.a-b). In both figures, moving from the smallest value (i.e., 500 kJ/°C, blue line) to the highest one (i.e., 2000 kJ/°C, purple line), a reduction in the peak value of Tws is observed after changes in load occur (such peak is usually referred as “overshoot”). Moreover, when the Cs is increased, the increased inertia helps to reducing the oscillating behavior in Tws, leading to a more stable chiller’s

operation. Fig. 36.c presents the average hourly EER values. Worth noting that the variation of Cs has a minimal impact on hourly EER values.

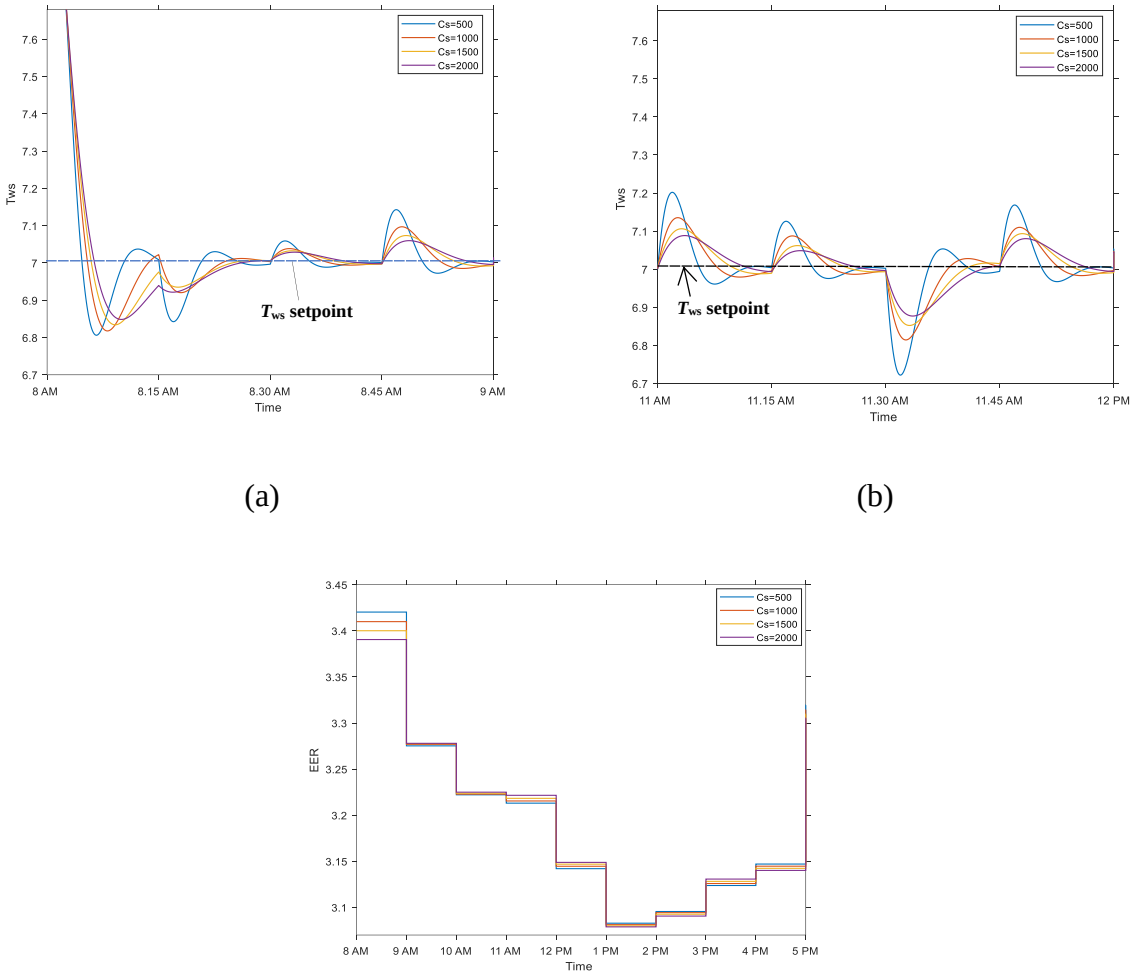

(a) (b)

(c)

Figure 36 Variable-speed chiller results with different Cs values: (a) Water supply temperature profile from 8-9 am in the high cooling load day, (b) Water supply temperature profile from 11-12 am in the low cooling load day, and (c) EER values in the high cooling load day.

The results of the sensitivity analysis for the case of constant-speed HP are presented in Figure 37. In this case, results for the same two hours (i.e., 8-9 am and 11-12 am) are presented not only for the high cooling day (Fig 37.a-b) but also in the case of low cooling day (Fig 37.c-d).

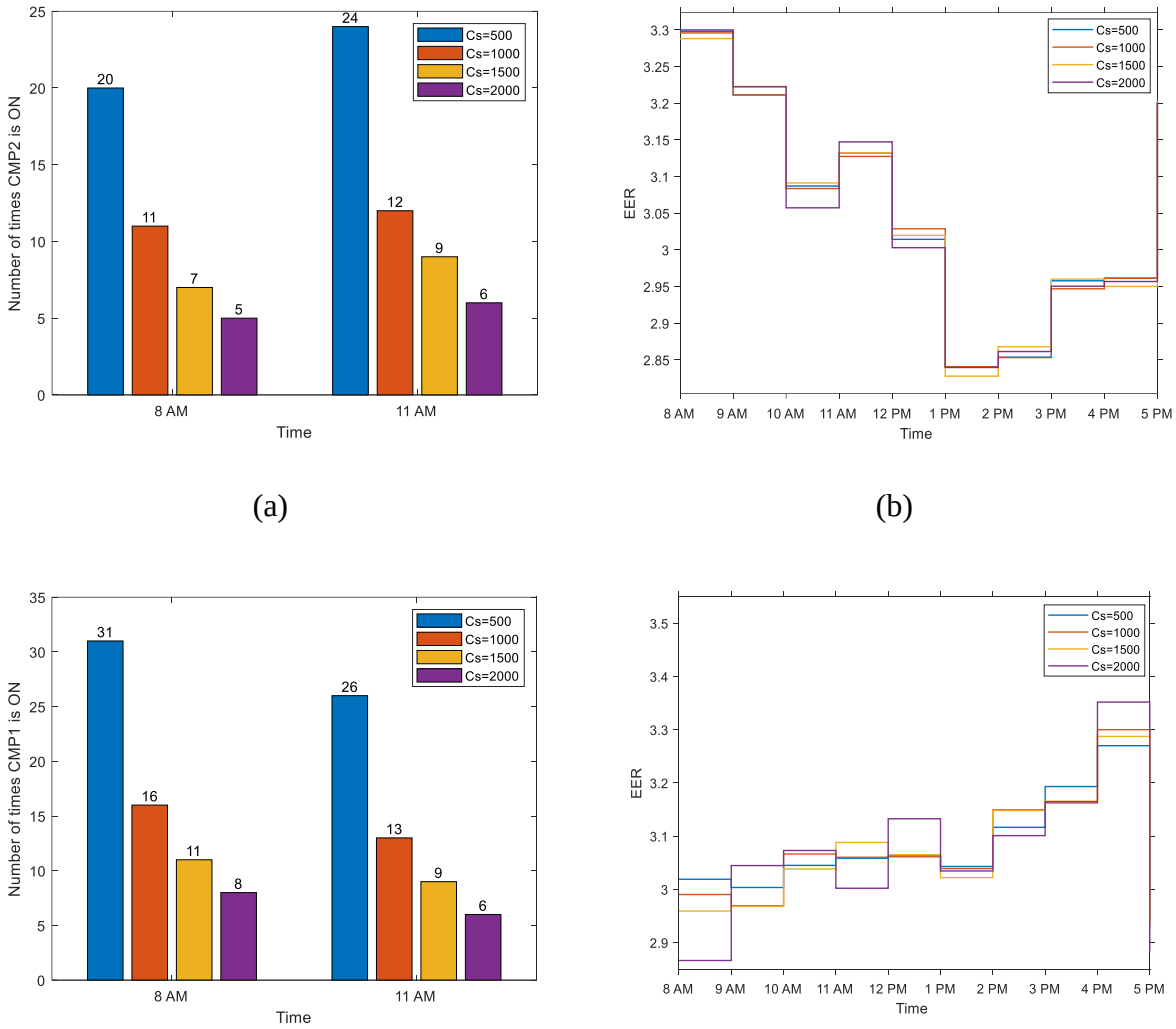

Figure 37 Constant-speed chiller results with different Cs values: (a) Number of CMP 2 cycling in the high cooling load day, (b) EER values in the high cooling load day, (c) Number of CMP 1 cycling in the low cooling load day, and (e) EER values in the low cooling load day.

As shown in Fig. 37.a, for the high cooling load day, only effects of CMP 2 are shown, since as previously observed, CMP 1 is always ON. Worth noting that, as the Cs increases (i.e., when the thermal inertia of the hydronic circuit increases) the number of cycling strongly reduces. More specifically, when passing from Cs= 500 kJ/°C to 1000 kJ/°C, the number of cycling ON-OFF for CMP 2 decrease, but it is almost near the threshold values in both hours (i.e., 12). However, if Cs is increase up to 1500 kJ/°C the number of cycling below the threshold value. Regarding the low-load cooling day (Fig 37.c-d), only effects of CMP 1 are shown, since as previously observed,

CMP 2 is always OFF. Also in this case, Cs should be increased up to 1500 kJ/°C to maintain the number of cycling below the threshold value. By looking at the EER values in Figs 37.b and 37.d, it can be noted that the variation of Cs has minimal impact on it.

Flexible operation of the air-cooled chiller

In the proposed scenario, the chiller was operated by setting a variable setpoint for the temperature of the water supplied to the building, as shown in Figure 29. Results for the high cooling load day are shown in Figure 38.a-b. As shown in Fig. 38.a, the Tws is not more kept at 7 °C like before (see Fig. 33-b). The values of Tws varies from 8 °C in the early morning to around 7.4 °C from 10 to 12 am, since the ODT values is less than 30 °C till 12 am (see Fig. 32.a). As shown in Fig. 38.b, an increase in the average value in some hours is achieved by this new strategy (orange line) compared to the previous one (yellow line).

Results for the low-cooling load day are shown in Figure 38.c-d. In this case, since ODT is always less than 30 °C (as shown in Fig. 32.a.). Therefore, the water is supplied to a Tws value higher than 7 °C (more specifically, Tws ranges among 9 and 9.5 °C), with a substantial increase in the average EER value through the whole day (Fig. 38.d).

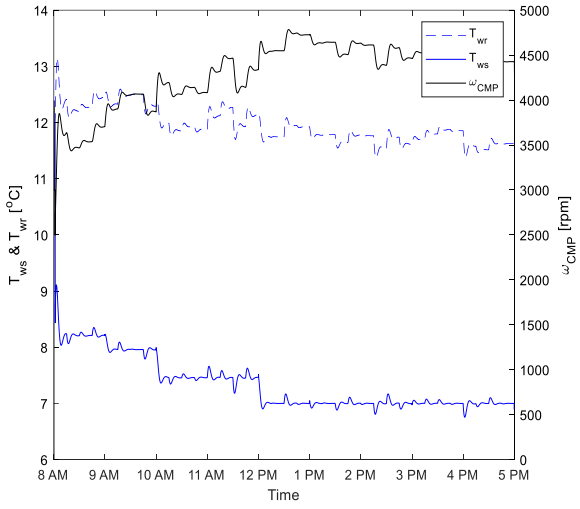

(a)

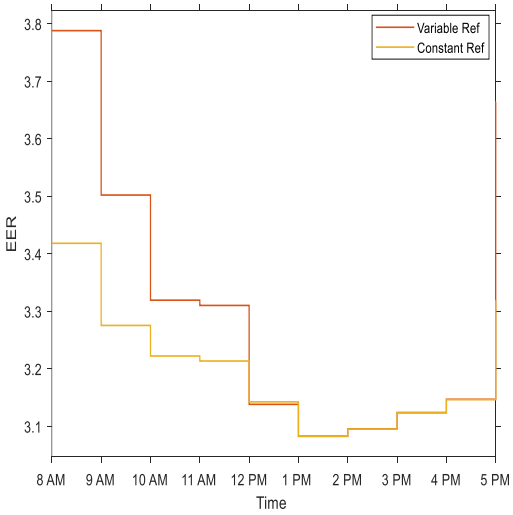

(b)

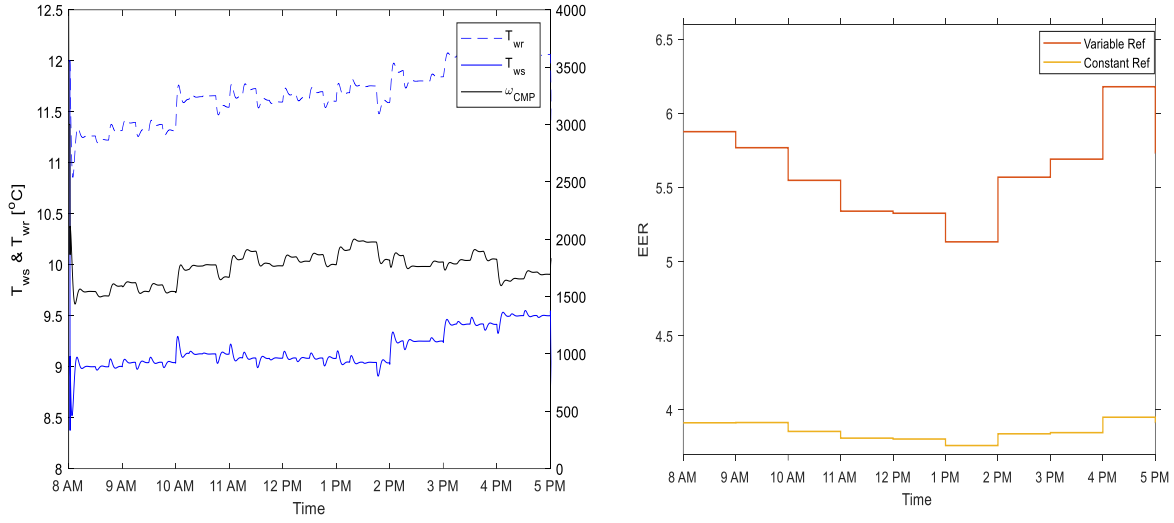

(c) (d)

Figure 38 Results: (a) Cooling Load and Cooling Capacity (b) Water supply, Water return temperature, and Compressor

6.3 Case study: Heating mode

An office building located in Palermo (Italy) was selected as a case study. In Figure 39.a, the values of ODT and RH for a typical cold day in winter (more specifically, January) in the selected area are shown. In figure 39.b the heating demand for the same day is shown. Focusing on the building load, it was assumed an operational for 11-hour during a day (more specifically, from 7am to 6pm) with a variation of the load at 15 minutes. In addition, the ODT value in Figure 39.a was at every one-hour interval.

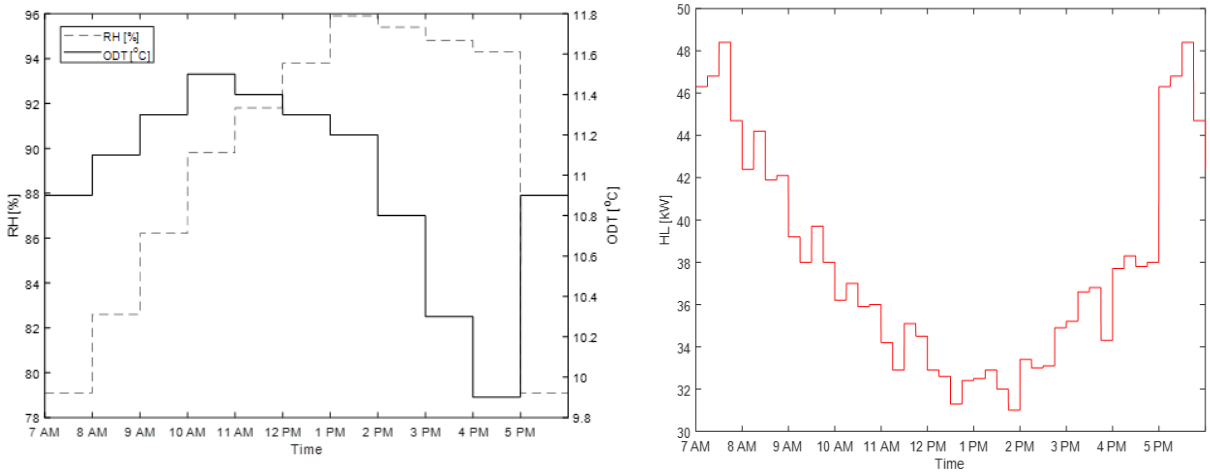

(a) (b)

Figure 39 (a) Heating mode ODT and RH (b) Heating Load

Variable-speed compressors: 62 kW nominal heating capacity was selected as the reference unit. Technical details on the refrigerant circuit are provided in Table 6.6. Besides, two induction motors (IM) with a 10-kW each were used in this unit, whose main parameters are obtained from datasheets and parameter estimation tests [21] and detailed in Table 6.6 as well.

Table 6. 6 Technical details on a 50-kW reversible variable-speed air-to-water HP and electrical parameters of the induction motor.

Refrigerant Circuit		Induction Motor	
Refrigerant	R410a	Pn(kW)	10
Condenser Type	Fin and Tube	Rs (Ω)	0.8
Number of Condenser	1	Rr(Ω)	2.91
Condenser Fan Power [kW]	1.5	Ls(H)	0.21
Metering Device	Electronic Expansion Valve	Lr(H)	0.21
Evaporator Water Flowrate [m3/h]	7.0	Lm(H)	0.2
Evaporator Pump Power [kW]	2	J(kg.m2)	0.1
Compressor Type	Scroll	Σ	0.03
Compressor Power (each) [kW]	9.0	f(Hz)	50
Refrigerant Charge [kg]	7.3	P	2

The thermodynamic models of the considered air-to-water HPs were developed by using the IMST-Art software[153]. The tool implements 1-D thermohydraulic modelling of heat exchangers, refrigerant lines, and accessories, and its reliability has been proven by accurate validation against wide sets of experimental results[154].

Table 6. 7 Matrix test for variable speed-mode

Mode	Variable		Range	Interval
Compressor mode	Costant speed		1CMP:ON (2900 rpm)	
	Variable-speed			
Cooling	ODT	[°C]	22-38	2
	ωCMP	[rpm]	1000-6000	400
	Tw,r	[°C]	8-14	2
Heating	ODT	[°C]	5-17	4
	RH	[%]	45-96	17
	ω_{CMP}	[rpm]	1000-6000	400
	Tw,r	[°C]	25-55	10

To map HP operation, different matrix tests were here developed, for the variable-speed HP and for the constant-speed respectively. The IMST-Art software data range and intervals with constraints for input temperatures (Evaporator and Condenser), output speed and RH for heating purposes are shown in Table 6.6. Note that the rotating speed of the EVP pump was kept constant throughout the simulation. Regarding the constant-speed HP a different procedure is followed. The same range were assumed here

Table 6. 8 Matrix test for constant-speed HP

Mode	Variable		Range	Interval
Cooling	ODT	[°C]	22-38	2
	ωCMP	[rpm]	2900	400
	Tw,r	[°C]	8-14	2
Heating	ODT	[°C]	5-17	4

	RH	[%]	45-96	17
	ω_{CMP}	[rpm]	2900	400
	Tw,r	[°C]	25-55	10

By using the approach presented in the Appendix 4, the linear coefficients are obtained using Least-square technique for the air-to-water HP. The Normalized Root Mean Square Error Index (NRMSE) is computed to understand the error-index of the realized model in comparison to the thermodynamic data were obtained using the IMST-Art software. The NRMSE is shown in Table 6.11 and Table 6.10 with the different linear coefficients for both the mechanical power ($\dot{P}_m$) and cooling capacity ($\dot{Q}_C$); Heating mode.

Table 6. 9 Preliminary modelling results: variable-speed HP

	Delivered Capacity			Absorbed Power		
VS-Cooling	L1	0.0086	RMSE [kW]: 2.26	K1	0.0037	RMSE [kW]: 1.41
	L2	-0.32		K2	0.05	
	L3	1.55	NRMSE [%]: 3.91	K3	-0.26	NRMSE [%]: 5.91

In a similar way, for a SC the linear coefficients are obtained using Least-square technique for the air-to-water heat pump. The Normalised Root Mean Square Error Index (NRMSE) is computed to understand the error-index of the realized model in comparison to the thermodynamic data were obtained using the IMST-Art software. The NRMSE is shown in Table 6.9 with the different linear coefficients for both the mechanical power (P_m) and cooling capacity (CC). The computed error index is less and 4% as shown in Table 6.10

Table 6. 10 Preliminary modelling results: constant speed HP

	Delivered Capacity			**Absorbed Power**		
CS-Heating	L_1	0.0107	RMSE [kW]: 0.704	K_1	0.0004	RMSE [kW]: 0.102
	L_2	0.9572		K_2	-0.0002	
	L_3	-0.207	NRMSE [%]: 3.66	K_3	0.1698	NRMSE [%]: 1.87

The overall scheme for sequential control and variable speed drive were implemented in MATLAB Simulink with knowledge on IM state-space model[4, 5], FOC[4, 5], hysteresis, Air-to-water RHP model [1, 2] and parameters of each of the components. All data used in the implementation of this simulation are presented in the results section. For this study overall control architecture is with a sample time equal to 0.01 seconds.

Since the simulation considered the full day operation (10 hours) of the HP, a large sample time is used to reduce the data-point and save space in memory and prevent the system from crashing. As previously mentioned, it was assumed an operational for 11-hour during a day (more specifically, from 7am to 6pm), which in simulation time it corresponds from 0 seconds to 39600 seconds. At every 900 seconds i.e. 15 minutes the cooling and heating load is recorded.

6.4 Results and Discussion Heating mode

Simulation results for the variable speed HP are first shown. Then results for the main findings for speed HP are first shown. The findings and their implications should be discussed in the broadest context possible. Future research directions may also be highlighted.

Variable-speed operation

In Figure 40. a-e, results for the typical heating day are shown. In Fig. 40.a the heating capacity delivered by the HP (red dashed line) follows the heating load profile (red continuous line). Like the cooling mode operation, the spike observed at around 7:00 am accounts for the hydronic inertia met during the starting phase of plant operation. Fig. 40.b shows the temperature profile of the water supplied to (Tws) and returning from (Twr) the hydronic loop. Worth noting that, in this case, Tws is maintained almost at 50 °C (the assumed HP setpoint in heating mode) by the action of the controller. Some oscillations are present each 15 minutes due to the changes in the load. In this respect, as shown in Fig. 40.b, the rotating speed of the CMP is varied to meet the water supply temperature setpoint. Fig. 40.c shows the mechanical power supplied by both the IMs to the CMP during the 11-hour operational period. Fig. 40.d shows the average hourly COP values for the 11-hour period. The COP ranges between 3.89 in the early morning where low ODT values and higher load are observed up to 4.48 at around 12:00 am when higher ODT values and lower heating load are observed.

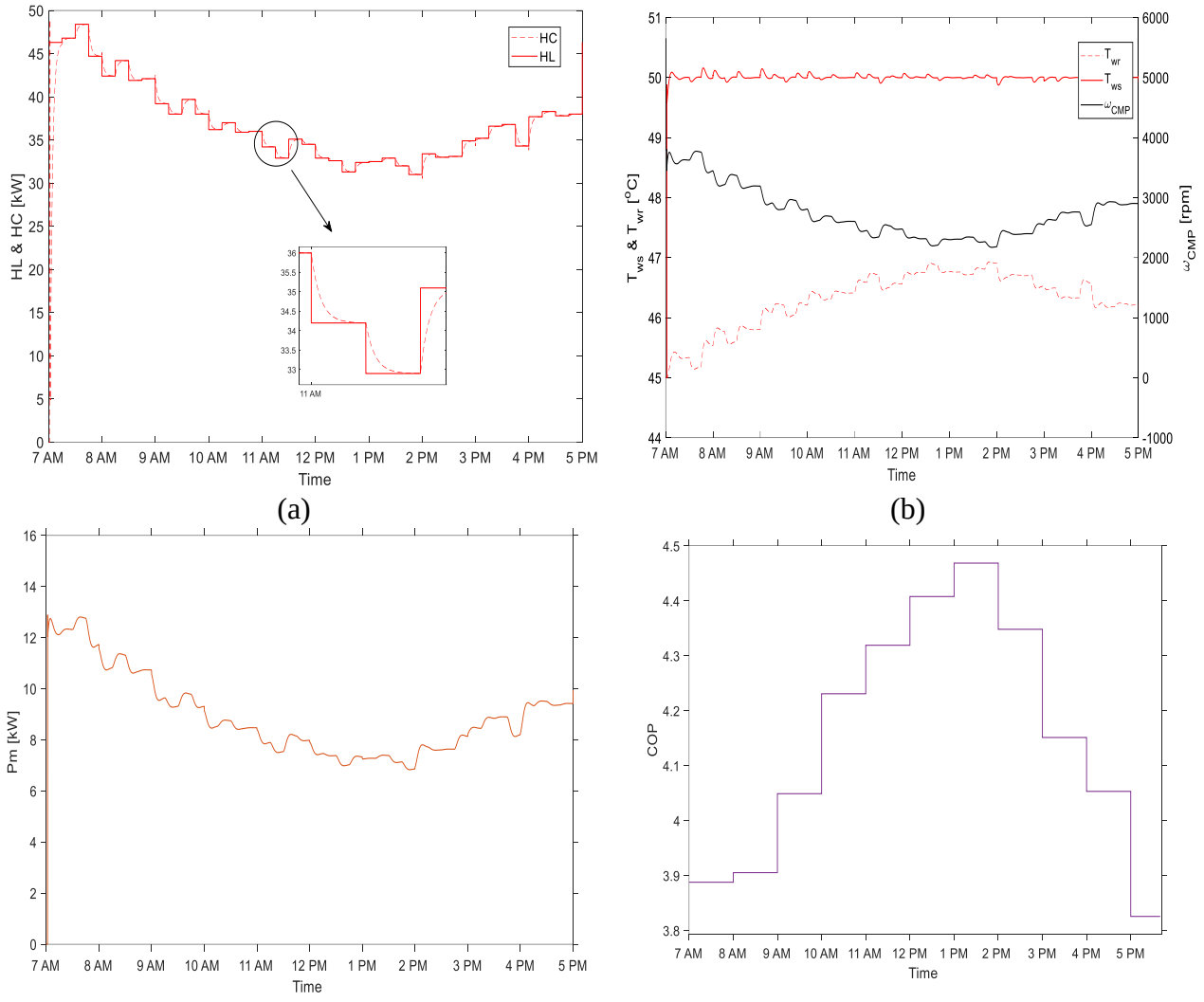

Figure 40 Heating mode. (a) Cooling Load and Cooling Capacity (b) Water supply, Water return temperature and Compressor speed, (c) Mechanical Power Schemes (d) COP

HP with sequential control

This section will results for the constant-speed HP in the high heating load day as shown in Figures 41.a-d. In Fig. 41.a, the heating demand profile (red continuous line) is again pre-sented together with the capacity delivered by the HP (dashed red line). The discon-tinuous pattern of the HC is due to the ON-OFF cycles of CMPs. In this respect, as shown in Fig. 41.b it is worth noting that CMP1 (black line) operates only from 7 to 10 am when the higher values of heating demand are observed. Then, after 10 am, CMP1 is always OFF, and CMP2 (blue line) is cycled to maintain the water supply tempera-ture in the desired range. In addition, Fig. 41.b shows that the temperature of the water supplied to the building is oscillating around the value of 44.75 °C value (black dashed line), from 7 to 10 am. After 10 am, the temperature of the water supplied to the

building is oscillating around the value of 45.25 °C values. This result is consequent to the band definitions for CMPs cycling shown in Table 6.

Figs. 41.c-d provides a focus on two hours in the high heating load day. More spe-cifically, Fig. 41.c plots the CMPs' operation from 7 to 8 am, when the highest demand is observed. Conversely, Fig. 41.d focuses on CMPs' operation from 1 pm to 2 pm when the lowest demand is observed. Looking at Fig. 41.c, CMP2 is ON for almost the whole hour, conversely, CMP1 cycles ON-OFF to meet the heating load. In addition, as indicated in Fig. 41.c, CMP1 is cycling ON-OFF almost 10 times, which is less than the maximum threshold value equal to "12 cycles per hour" required

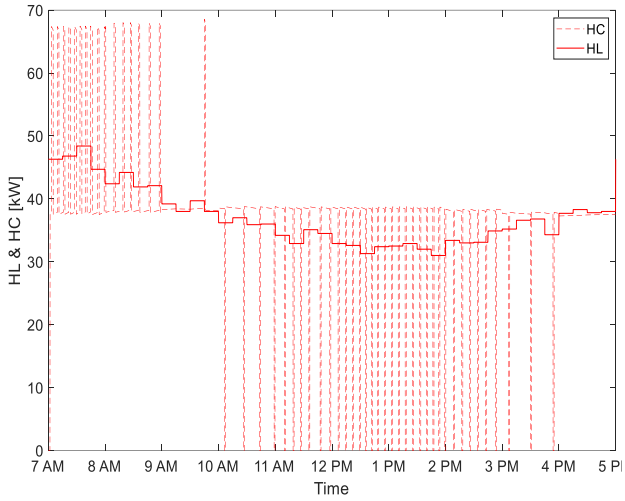
HC
HL
HL & HC [kW]
Time
7 AM
8 AM
9 AM
10 AM
11 AM
12 PM
1 PM
2 PM
3 PM
4 PM

(a)

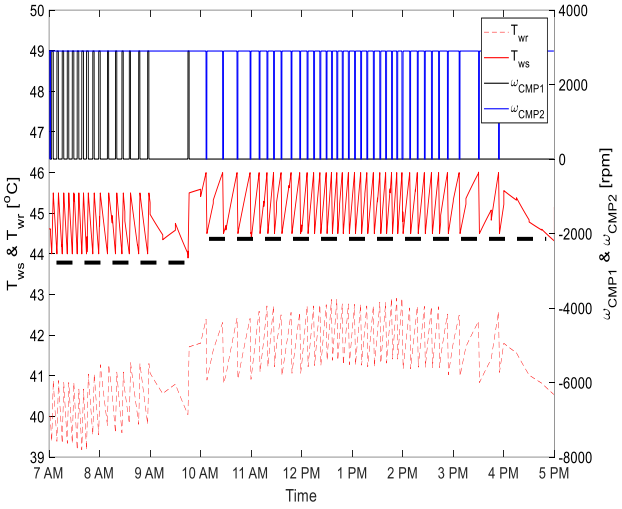
T_{wr}
T_{ws}
ω_{CMP1}
ω_{CMP2}
T_{ws} & T_{wr} [°C]
ω_{CMP1} & ω_{CMP2} [rpm]
Time
7 AM
8 AM
9 AM
10 AM
11 AM
12 PM
1 PM
2 PM
3 PM
4 PM
5 PM

(b)

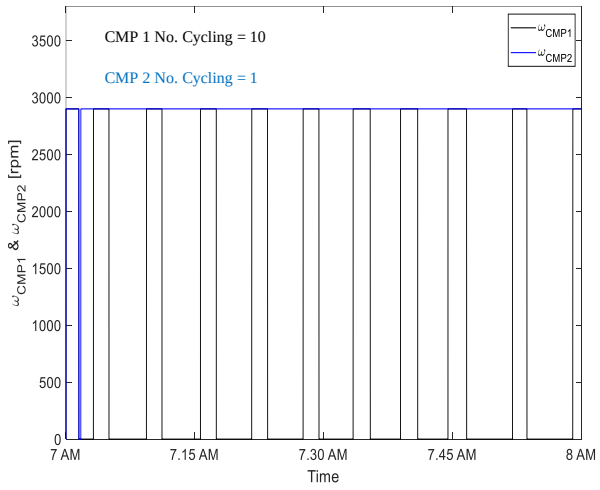
CMP 1 No. Cycling = 10
CMP 2 No. Cycling = 1
ω_{CMP1}
ω_{CMP2}
ω_{CMP1} & ω_{CMP2} [rpm]
Time
7 AM
7.15 AM
7.30 AM
7.45 AM
8 AM

(c)

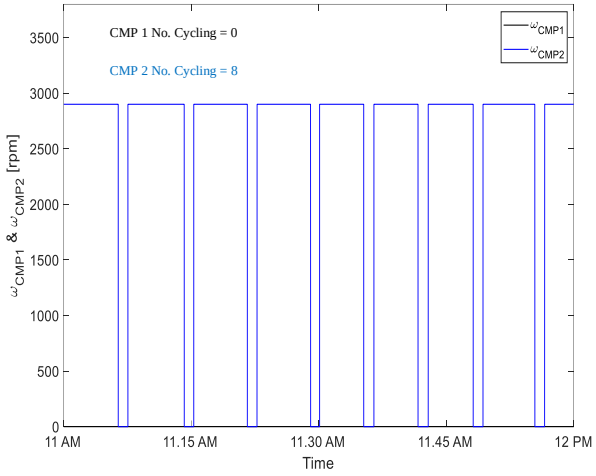
CMP 1 No. Cycling = 0
CMP 2 No. Cycling = 8
ω_{CMP1}
ω_{CMP2}
ω_{CMP1} & ω_{CMP2} [rpm]
Time
11 AM
11.15 AM
11.30 AM
11.45 AM
12 PM

(d)

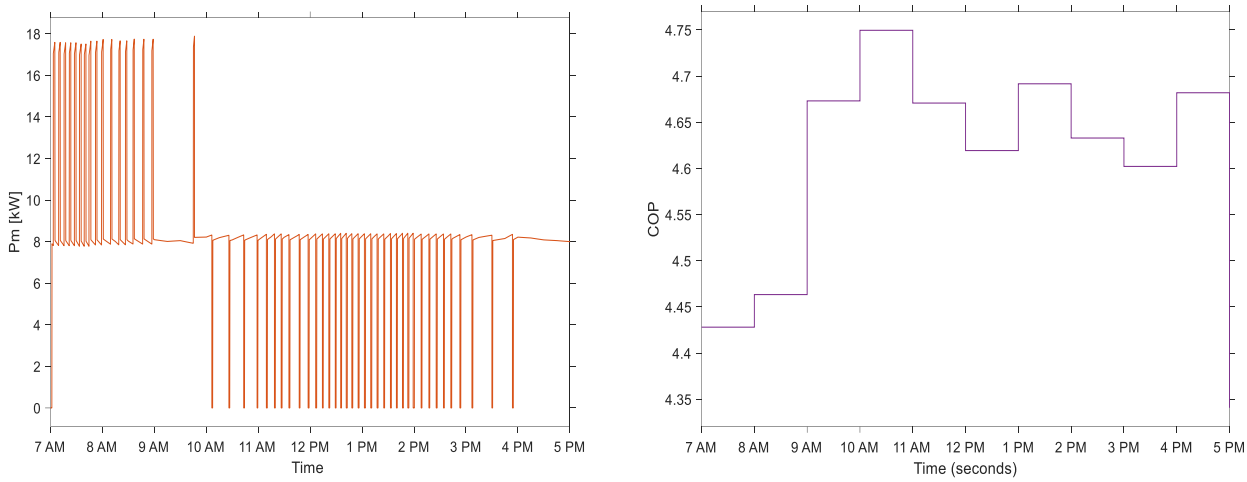

(e) (f)

Figure 41 Sequential Control(a) Heating Load and Heating Capacity (b) Water supply, Water return temperature, and CMPs cycles, (c) CMPs' operation from 7-8 am, (d) CMPs' operation from 1-2 pm, (e) Mechanical Power, and (f) COP

for assuring a safe CMP opera-tion. As shown in Fig. 41.d, from 1 pm to 2 pm, CMP1 is always OFF, and CMP2 is cy-cled to maintain the water supply temperature in the desired range. More specifically, CMP2 is cycling ON-OFF almost 8 times, which is less than the maximum threshold suggested by the manufacturer (i.e., 12). In Figure 41.e, the mechanical power required by the CMPs is plotted. Fig. 41.f shows the average hourly COP values. The COP ranges between 4.45 to 4.75 during the operation due to the time-varying ODT values.

For each operation mode, the variable speed control technique outperforms the constant speed control for an IM RHP drive, since the EEr values for 10-hour daily operation are always higher at each instant. For RHP capacity of 20% or lower, both the variable and constant speed RHP operate as a constant speed HP. However, this is not valid for this case study as the capacity is always higher than 50% of the rated capacity.

Sensitivity analysis of results with the design of the hydraulic loop

It is worth investigating results with variation of C_s are presented for VSD. Moreover, SC results are presented with C_s=1500 and variation of C_s for heating mode results with VSD are presented for C_s=1500. Results of variation of C_s for the peak cooling load window between 10 am to 3 pm are presented below.

Fig.42.a presents the water supply temperature for different values of hydronic inertia. It can be seen that a small value of C_s gives a higher initial peak and higher oscillations, however as the C_s is gradually increased the peak and oscillations are reduced as the plant serves a higher hydronic inertia.

Fig. 42.b shows the compressor speed for different values of C_s. The smaller value of C_s correspond to a smaller value of the hydronic inertia hence it is more susceptible to speed variations. However, as the C_s increases the plants operates with a higher value of inertia and result is a stable but slower speed response. Fig. 42.e presents the EER for the peak cooling load period. The EER values range between 3.22 and 3.08 while the variation of C_s has minimal impact on these values.

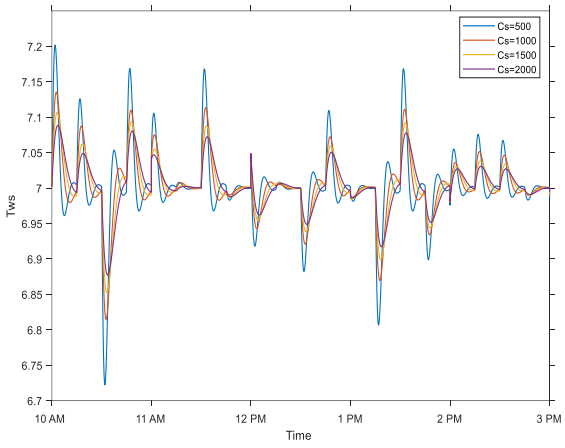

(a)

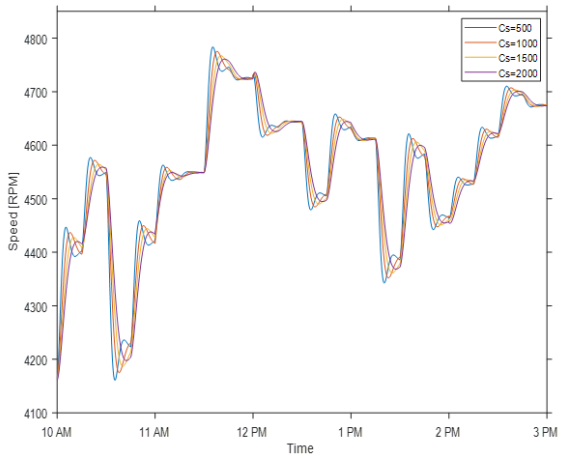

(b)

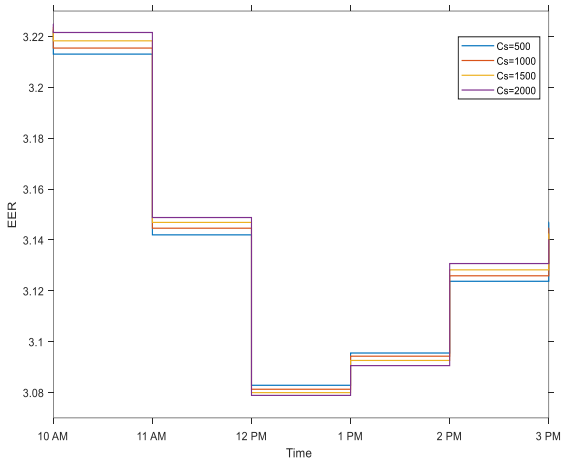

(c)

Figure 42 This is a figure. (a) Cooling Load and Cooling Capacity (b) Water supply, Water return temperature and Compressor speed, (c) EER

Results of variation of C_s for a 15 minute interval between 10 am and 10.15 am are presented. Fig. 43.a presents the water supply temperature for different values of hydronic inertia. It can be seen that a small value of C_s have more oscillations on T_{ws} compared to higher C_s values.

Fig. 43.b illustrates the compressor speed for different values of C_s. The smaller value of C_s represent a smaller value of the hydronic inertia hence T_{ws} is more susceptible to speed variations and numerous on-off are required. However, for larger values of C_s the value of inertia in increases and the resulting on-off modulation is reduced. Since this particular scenario has a high cooling load compressor 1 is always operational for the investigated period. Fig. 43.c presents the EER for the 15-minute period. The EER values range between 2.9 and 2.7 and its can be noted that the variation of C_s has minimal impact on it.

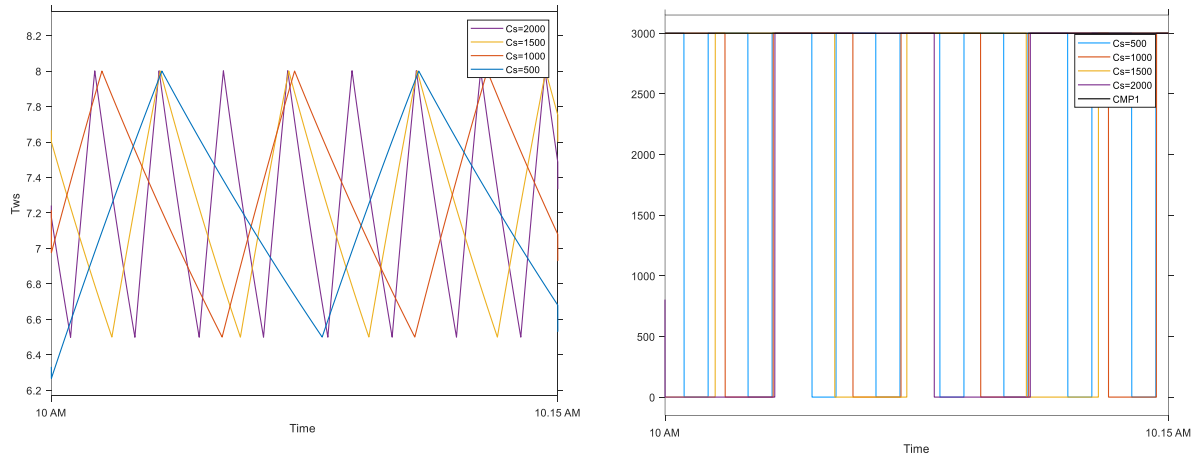

(a) (b)

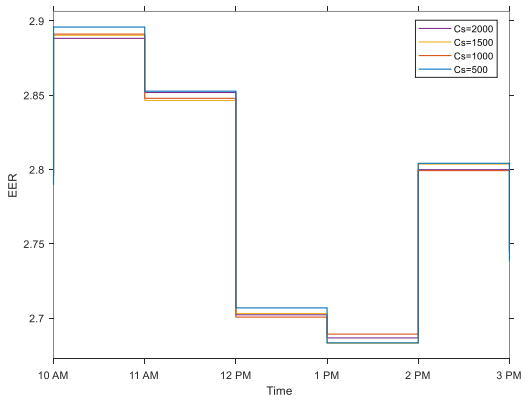

(c)

Figure 43 This is a figure. (a) Cooling Load and Cooling Capacity (b) Water supply, Water return temperature and Compressor speed, (c) EER

6.5 Results and Discussion for Fouling:

Results with the discussion is presented in this section of a RHP working in cooling model.

Estimation of Air-cooled chiller parameters

A scenario of fouling and no-fouling condition is tested in MAtlab Simulink to validate the parameter estimation technique. Fig. 44 presents the validation of the parameter estimation using RLS technique.

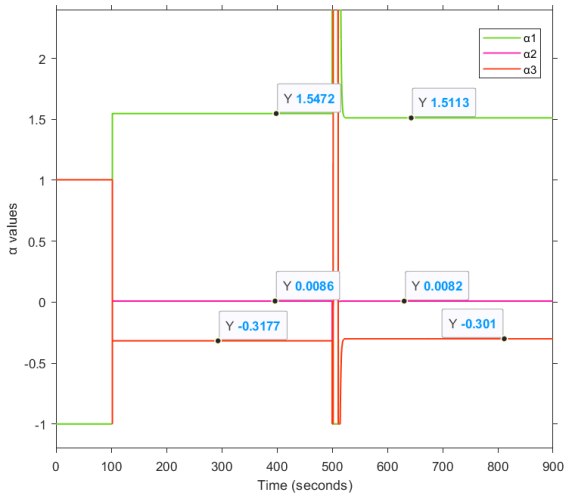

Figure 44 Estimation of Parameters usingRLS

At 500 seconds the 20% fouling condition is introduced into the existing model and the developed method is able to estimate the new model parameters. The fouling and no-fouling parameter of the air-cooled chiller can be observed in Table. 6.11 and Table. 6.12.

Thermodynamic data of a 50kW Air-to-water RHP in cooling mode are obtained using IMSTart software. Soon after the fitting coefficients are computed using Least square technique. For a healthy condition with 0% fouling the parameters are shown below:

Table 6. 11 Fitting coefficient parameters for Air-cooled chiller without fouling

	Delivered Capacity			**Absorbed Power**		
VS-Cooling	L_1	0.0086	RMSE [kW]: 2.26 NRMSE [%]: 3.91	K_1	0.0037	RMSE [kW]: 1.41 NRMSE [%]: 5.91
	L_2	-0.32		K_2	0.05	
	L_3	1.55		K_3	-0.26	

Using IMSTart to generate data of a 20% fouling condition on the condenser, new fitting coefficients are computed for the RHP under fault.

Table 6. 12 Fitting coefficient parameters for Air-cooled chiller with 20% fouling

Delivered Capacity				**Absorbed Power**		
	L_1	0.0082	RMSE [kW]: 2.32	K_1	0.0038	

	L_2	-0.30	NRMSE [%]: 4.18	K_2	0.041	RMSE [kW]: 1.47
VS-Cooling	L_3	1.51		K_3	-0.26	NRMSE [%]: 5.85

Comparison of Air-cooled chiller operation in fouling and no-fouling condition

At daily operation of a RHP during a hot summer day in Palermo is considered for this study with fouling and no-fouling at the condenser of a RHP. Fig. 45 shows the cooling load [kW] at 15-minute intervals and Outdoor temperature at 1-hour intervals for a building in Palermo, Sicily during a very hot day from 8 am to 5 pm. Fig. 46 and 49 present the cooling capacity provided by the air-cooled RHP and the cooling load of the building with no fouling and 20% fouling respectively. For both cases, the cooling demand of the building is supplied by the RHP. This part of the thesis will pay attention to the extent of the cost at which the cooling demand is met in fouling conditions.

Fig. 47 and 48 give the water return temperature, water supply temperature with a set-point of 7 ^{0} C, and compressor speed that is coupled to an IM drive at no fouling and 20% fouling respectively. For both cases, the water supply temperature is maintained at 7 ^{0} C in the building and the speed profile is shown accordingly. It can be observed that the compressor speed is slightly higher during a 20% fouling of the condenser fan in comparison to a no-fouling condition. Fig. 50 presents the energy efficiency ratio (EER) for a daily operation with the same cooling load and ODT with no fouling, 20% fouling, and adaptive control compensation. As hypothesized initially, EER of an air-cooled chiller with 20% fouling gives poor performance compared to no fouling conditions. Adaptive feed-forward techniques is utilized to provide a command action in terms of compressor speed. Fig. 51 shows speed response signal fault compensation. Fig.52 presents the speed response of the overall system with fault-free condition, 20% fouling fault, and feedforward compensation. As observed in fig.52, fouling of 20% results in increased overall compressor speed, feedforward technique gives an additional control signal $\Delta\omega_{cmp}$ to help compensate for the fault condition.

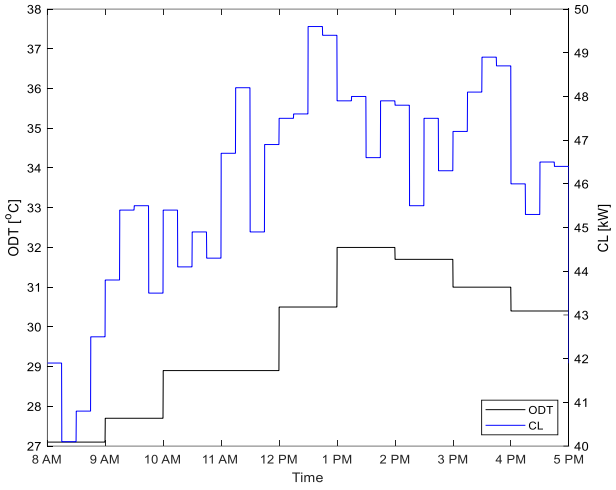

Figure 45 Cooling load and ODT for 10-hour period

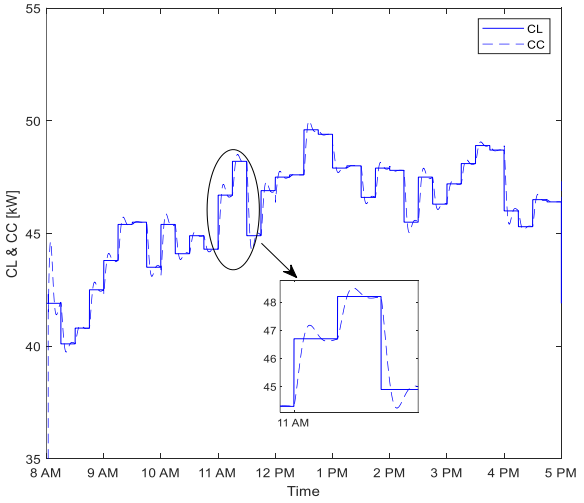

Figure 46 Cooling Capacity and cooling load

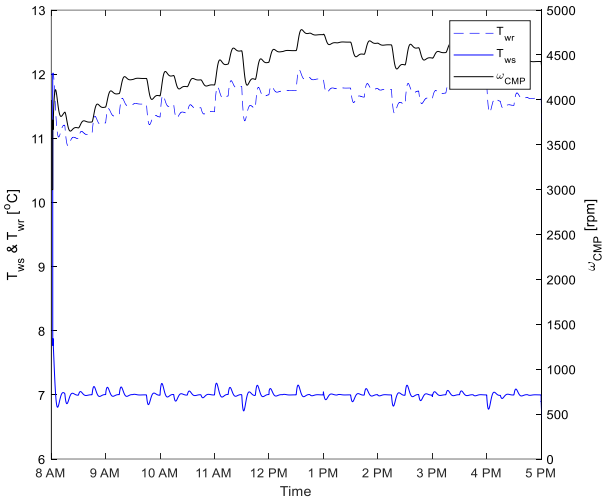

Figure 47 Water supply temperature, water return temperature and compressor speed.

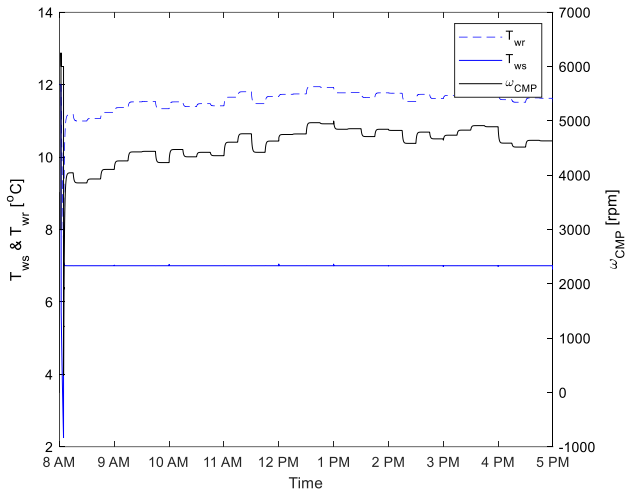

Figure 48 Water return temperature, water supply temperature and compressor speed for 20% fouling

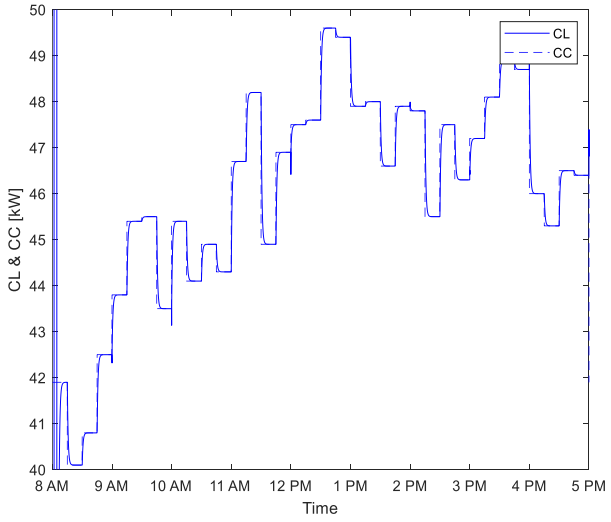

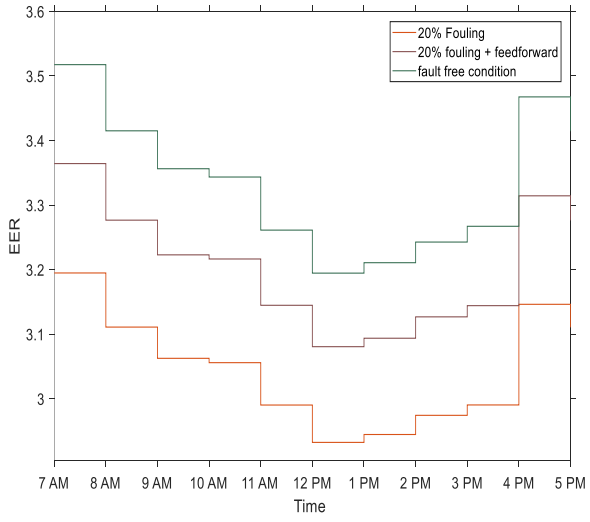

Figure 49 Cooling capacity and cooling load at 20% fouling

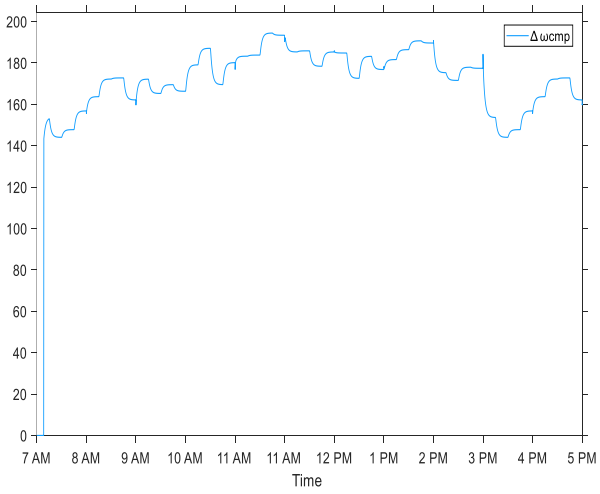

Figure 51 Δωcmp response during fouling operation

Figure 50 EER for normal case and 20% fouling

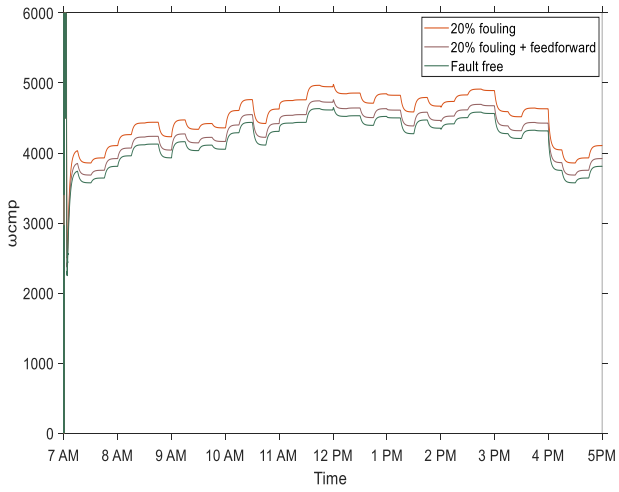

Figure 52 Speed response

6.6 Results and Discussion for Charge Variation:

Thermodynamic data of a 50kW Air-to-water RHP in cooling mode are obtained using IMSTart software. Soon after the fitting coefficients are computed using Least square technique. For a healthy condition with 10% refrigerant charge fault the parameters are shown below:

Table 6. 13 Fitting coefficient parameters for Air-cooled chiller without fault

	Delivered Capacity			Absorbed Power		
VS-Cooling	L_1	0.0082	RMSE [kW]: 2.26	K_1	0.004	RMSE [kW]: 1.41
	L_2	-0.29	NRMSE [%]: 3.91	K_2	0.039	NRMSE [%]: 5.91
	L_3	1.47		K_3	-0.27	

Using IMSTart to generate data of a 10% under refrigerant charge condition on the system, new fitting coefficients are computed for the RHP under fault.

Table 6. 14 Fitting coefficient parameters for Air-cooled chiller with 10% under refrigerant charge

	Delivered Capacity			Absorbed Power		
VS-Cooling	L_1	0.0079	RMSE [kW]: 2.32	K_1	0.0038	RMSE [kW]: 1.47
	L_2	-0.28	NRMSE [%]: 4.18	K_2	0.04	

L_3	1.42		K_3	-0.27	NRMSE [%]: 5.85

Comparison of Air-cooled chiller operation in fault free and 10% refrigerant under charge

At daily operation of a RHP during a hot summer day in Palermo is considered for this study with 10% charge fault and no-charge fault in the RHP. The cooling load and ODT values are similar to fouling test cases. Fig. 53 presents the cooling capacity provided by the air-cooled RHP and the cooling load of the building with 10% charge fault with feedforward compensation. Fig. 54 give the water return temperature, water supply temperature with a set-point of 7 ^{0} C, and compressor speed that is coupled to an IM drive at 10% charge fault with compensation. Fig. 55 presents the speed of the compressor during fault free, 10% charge fault, and 10% charge fault with compensation. It can be observed that the compressor speed is slightly higher during a 10% charge fault in comparison to a fault free condition. It can be observed that the feedforward action reduces the compressor speed compared to the fault condition, hence reducing the overall stress on the plant. Fig. 56 presents the energy efficiency ratio (EER) for a daily operation with the same cooling load and ODT during fault-free, 10% charge fault, and adaptive feedforward control compensation. As hypothesized initially, the EER of an air-cooled chiller with 10% charge fault gives poor performance compared to fault free conditions. Adaptive feed-forward techniques is utilized to provide a command action in terms of compressor speed. Fig. 57 shows the added speed response signal for fault compensation.

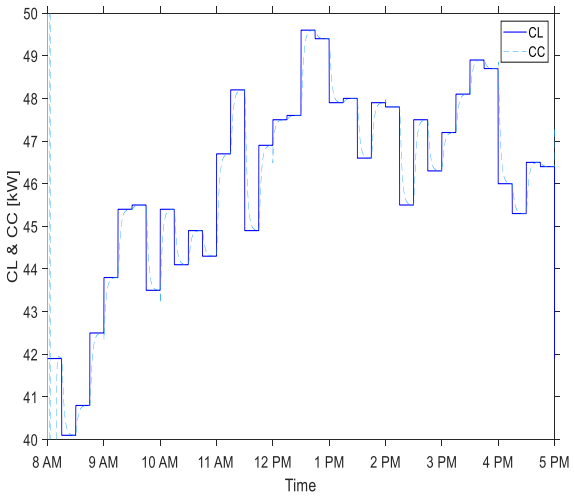

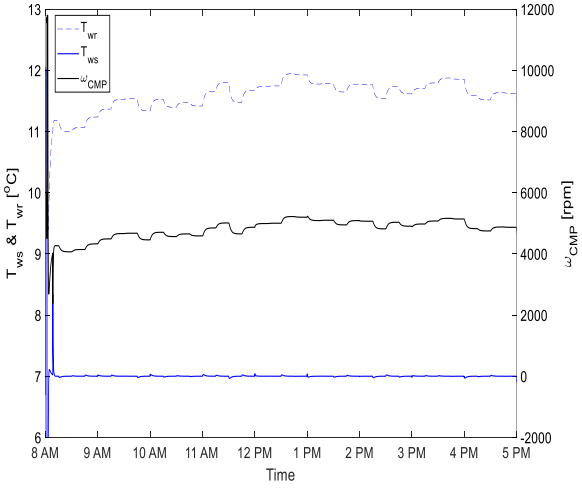

Figure 53 CC and CL for 10% charge fault

Figure 54 Water supply temperature, water return temperature and compressor speed.

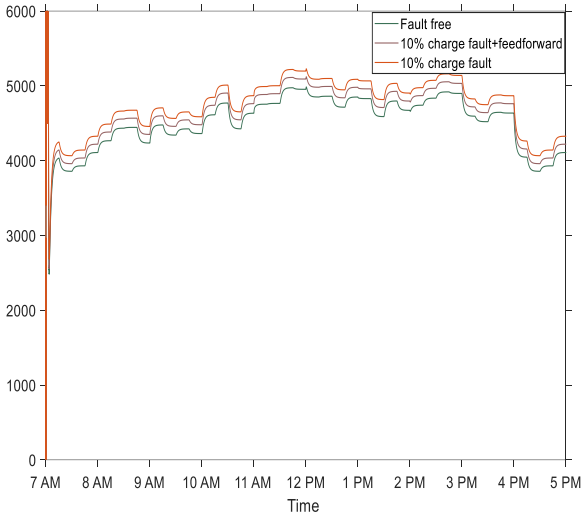

Figure 55 Speed response for 10% charge fault

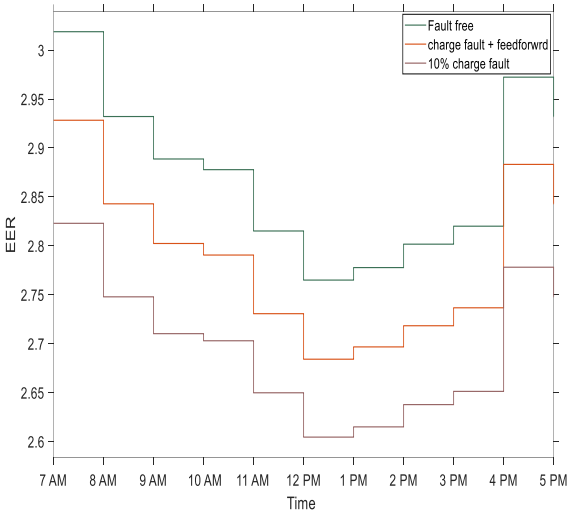

Figure 56 EER for normal case, 10% charge fault , and 10% charge fault with compensation.

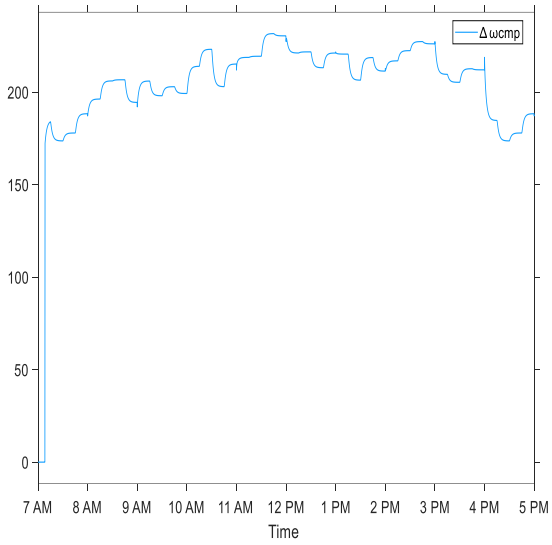

Figure 57 Δωcmp response during charge fault operation

It is important understand fouling and refrigerant charge faults in a RHP as shown in the above analysis that although the internal comfort the end-users are satisfied but the EER is compromised. As a result, the energy consumption of the building will increase gradually. This must not be mistaken for the fact that the increase is due to new installations or high occupancy which maybe the case at times. Hence, deploying an RLS technique with feedforward to estimate plant parameters and compensate for faults has substantial potential to improve EER.

Conclusion

In this framework, the provision of modeling on a detailed thermodynamic modeling and the embedded architecture control is of paramount importance to achieve reliable control and operation. More specifically, the developed models should provide insights into (i) the ability of the RHP to quickly respond to the variation in the cooling and heating demand of the users (e.g., building load); (ii) the capability to adapt to the variation in the local while accounting for limits of the electric motor and the embedded controller, and (iii) the possibility to compare new control strategies aimed at improving the overall energy performance. The thesis compared different controls (e.g., proportional-integral for variable speed, and hysteresis controller for sequential control.) and they demonstrated that the modeling complexity of the system control has a significant impact on the key performance indicators, proving that this aspect should not be overlooked. For instance, for short-term operation, the modeling of the heat pump controller and the transient effects of the heat pump, such as cycling losses during start-up, are important.

Chapter 3, gives an insight into the basic concepts covers in a thermodynamic heating and cooling system. A brief description of vapor compression cycle, compressor types, and reversible heat pump compoenents are given. Electrical drives contribution is given to RHP technology and two basic control techniques (variable speed and constant speed) are discussed. Modeling of a RHP using physical model is presented with multi-variable models. A state-space model for variable and constant speed is developed for heating and cooling applications. The 3D plot for cooling and heating mode operation are presented in appendix 1 and 2 respectively. Chapter 4, gives a detailed overview on control techniques that have been applied to control of motor drives. For simplicity and reduced complexity, scalar open loop and closed loop are developed instead of FOC. The basics of controller design are presented, and the variable speed and constant speed techniques are highlighted with overall RHP control techniques. Finally, RHP variable set-point temperature control methodology is also presented.

Chapter 5 is dedicated to parameter estimation and fault diagnosis. Initially, the RLS methodology is implemented to acquire the RHP parameters. In this chapter fault model of RHP for 20% condenser fouling and 10% charge capacity fault in cooling mode. Finally, an adaptive feedforward compensation on the compressor speed is added to improve performance during fault conditions. Finally, the chapter 6 presents the result of heating and cooling mode operation for a

50kW building in Palermo, Italy. Constant speed and variable speed control are implemented and the superiority of variable speed control is highlighted. For each operation mode, the variable speed control technique outperforms the constant speed control for an IM RHP drive, since the EEr values for 10-hour daily operation are always higher at each instant. For RHP capacity of 20% or lower, both the variable and constant speed RHP operate as a constant speed HP. However, this is not valid for this case study as the capacity is always higher than 50% of the rated capacity. It is important understand fouling and refrigerant charge faults in a RHP as shown in the above analysis that although the internal comfort the end-users are satisfied but the EER is compromised. As a result, the energy consumption of the building will increase gradually. This must not be mistaken for the fact that the increase is due to new installations or high occupancy which maybe the case at times. Hence, deploying an RLS technique with feedforward to estimate plant parameters and compensate for faults has substantial potential to improve EER.

Appendix 1

Representing the data of a 50kW chiller for Q_c and P_m. A 6 degree Celsius intervals for ODT is used i.e 24-30-36. A 3D surface with a function of T_{wr}, ODT, f are plotted where $Q_c = f(T_{wr}, ODT, f)$ and $P_m = f(T_{wr}, ODT, f)$.

Figure For Qc

At 36degrees ODT

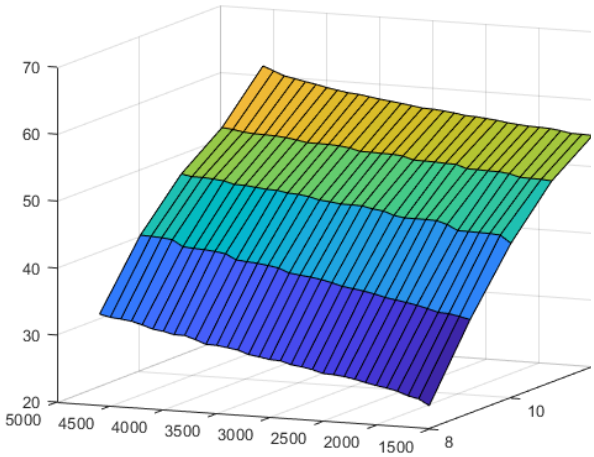

At 30degrees ODT

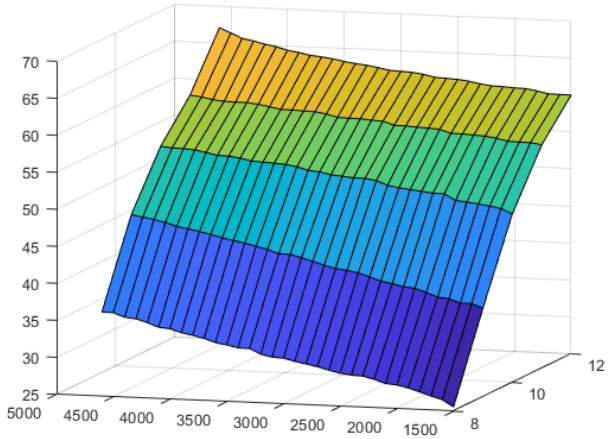

At 24degrees ODT

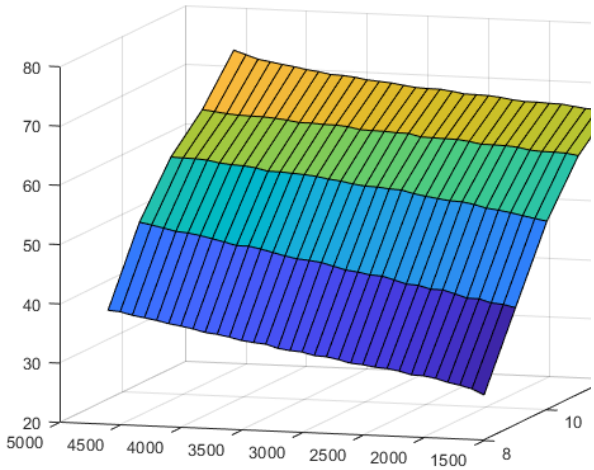

At 24/30/36 degrees ODT

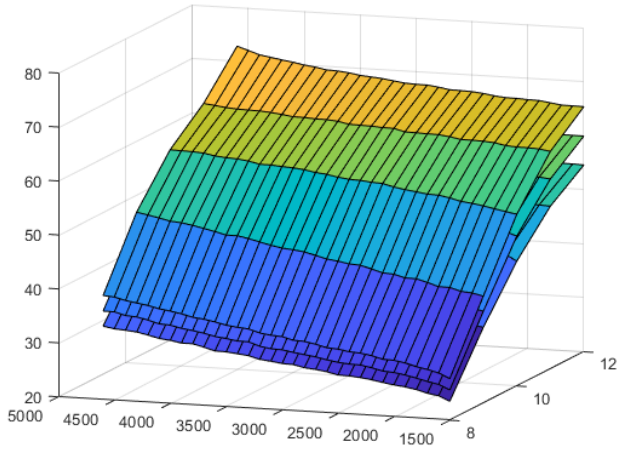

Figure for Pm

At 36degrees ODT

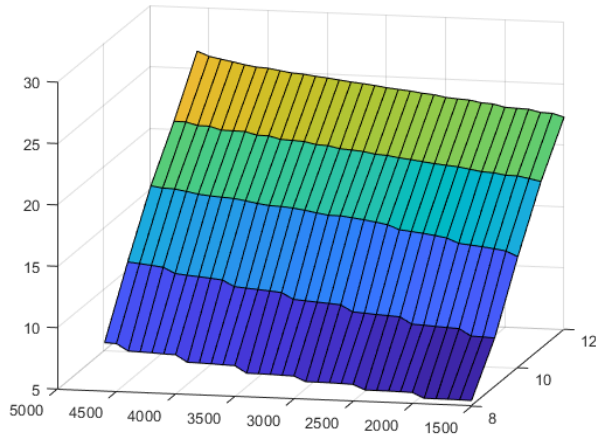

At30 degrees ODT

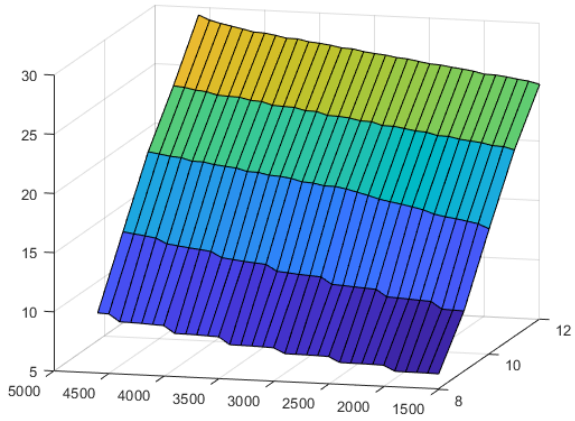

At 30 degrees ODT

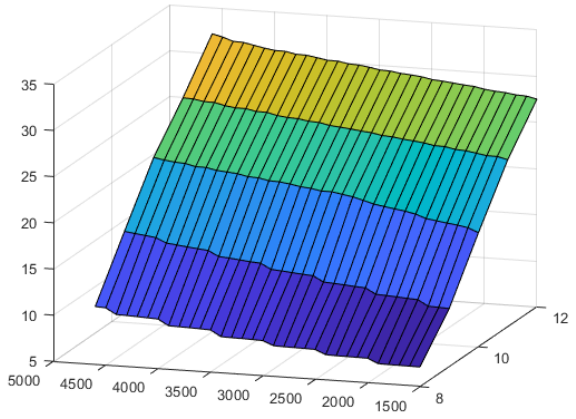

At 24/30/36 degrees ODT

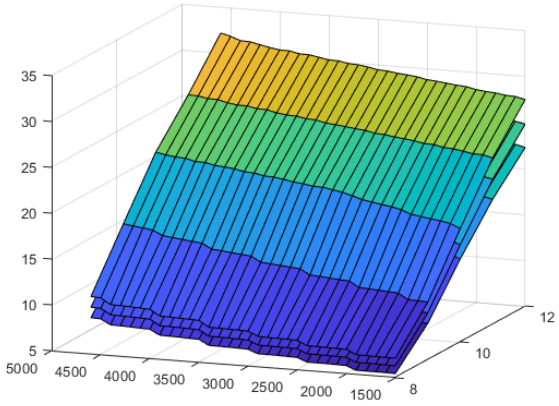

Considering the nature of the 3D surface a set of non-linear equation (1&2) and linear equations (3&4) are used to express the data using linear coefficients to match the data.

For the chiller investigated in the present study, data from the catalog were duly compared with the simulation results. In this regard, Fig. A3.a-b depicts the CC and the EER for the constant-speed chiller in some operating conditions that differ in terms of *ODT* and water flow rate through the evaporator, assuming a water return temperature from the hydronic loop equal to 12 °C. The figure reveals a good agreement between simulation results and catalog data, as shown in Fig. A3.c where the percentage errors for both CC and EER are always lower than 7%, thus confirming the good accuracy of the model.

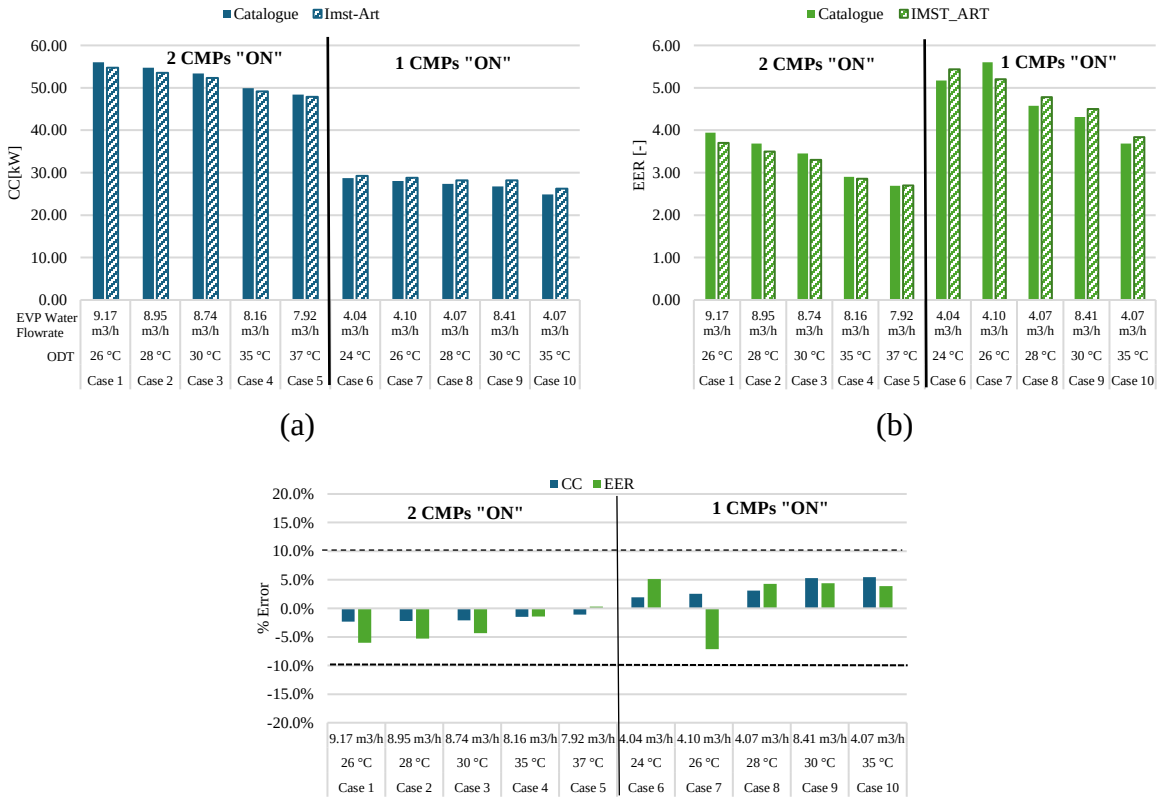

Figure A3. Comparison of IMST-Art results and data from the catalog of the chiller: (a) cooling capacity, (b) energy efficiency ratio, and (c) percentage errors.

Appendix 2

Representing the data of a 50kW heat pump for Q_H and P_m. A 4 degree Celsius intervals for ODT is used i.e 5-9-13-17. A 3D surface with a function of T_{wr}, ODT, f are plotted for RH at 45 where $Q_H = f(T_{wr}, ODT, f)$ and $P_m = f(T_{wr}, ODT, f)$.

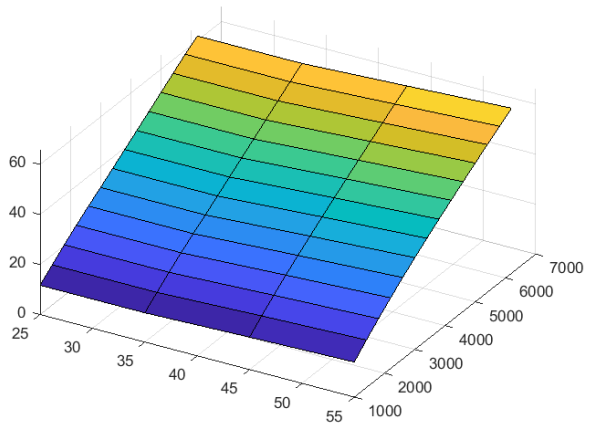

(a)

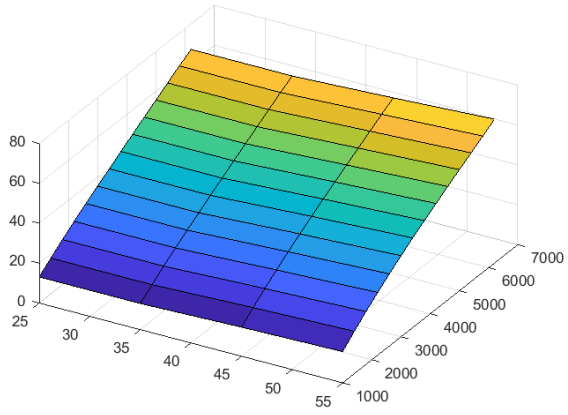

(b)

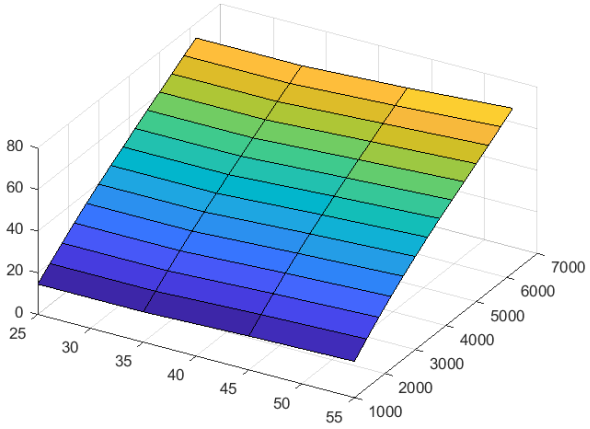

(c)

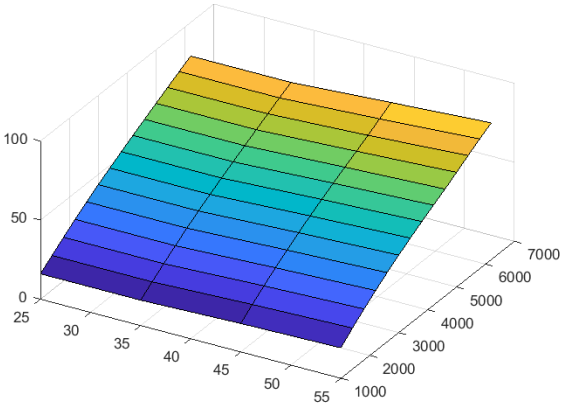

(d)

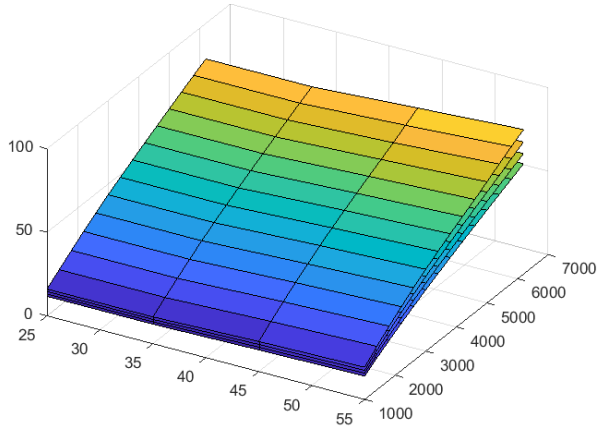
100
50
0
25
30
35
40
45
50
55
1000
2000
3000
4000
5000
6000
7000

(e)

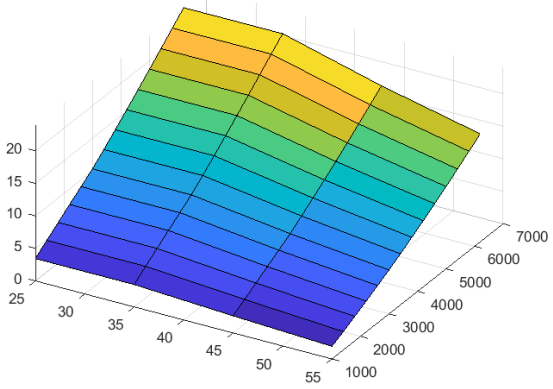
20
15
10
5
0
25
30
35
40
45
50
55
1000
2000
3000
4000
5000
6000
7000

(f)

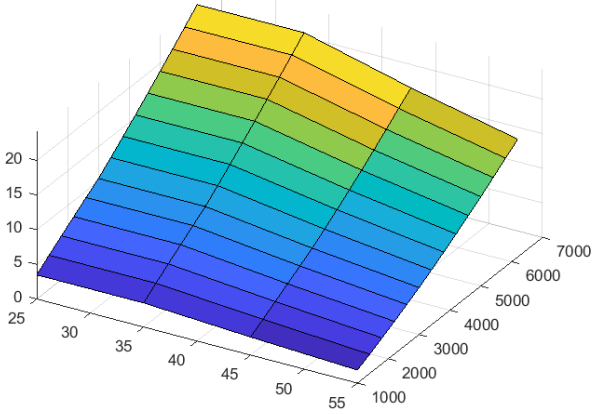
20
15
10
5
0
25
30
35
40
45
50
55
1000
2000
3000
4000
5000
6000
7000

(g)

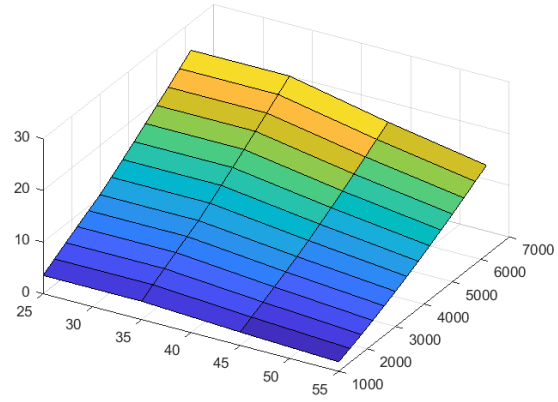
30
20
10
0
25
30
35
40
45
50
55
1000
2000
3000
4000
5000
6000
7000

(h)

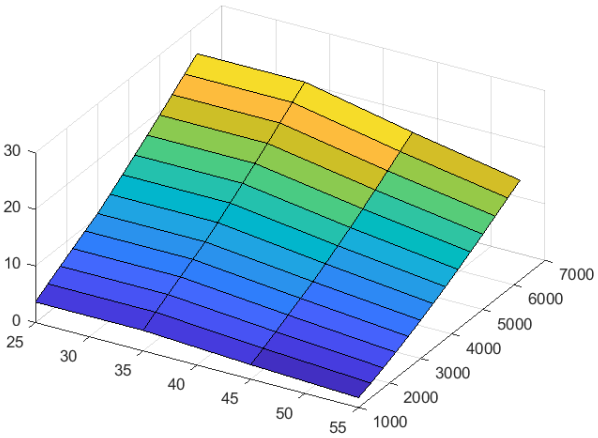
30
20
10
0
25
30
35
40
45
50
55
1000
2000
3000
4000
5000
6000
7000

(i)

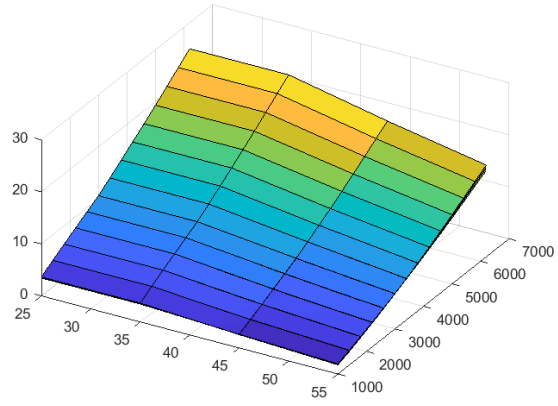
30
20
10
0
25
30
35
40
45
50
55
1000
2000
3000
4000
5000
6000
7000

(j)

Representing the data of a 50kW heat pump for Q_H and P_m. A 4 degree Celsius intervals for ODT is used i.e 5-9-13-17. A 3D surface with a function of T_{wr}, ODT, f are plotted for RH at 79 where $Q_H = f(T_{wr}, ODT, f)$ and $P_m = f(T_{wr}, ODT, f)$.

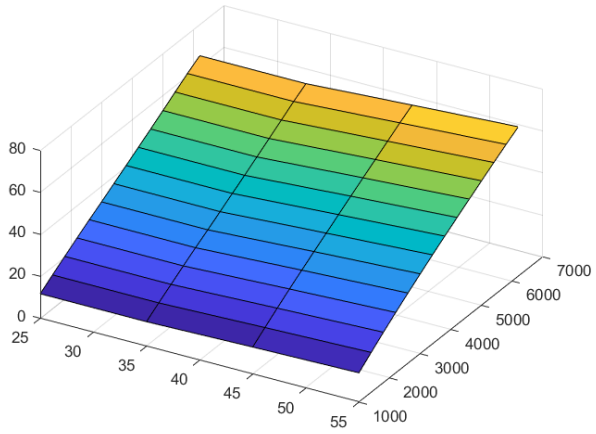

(a)

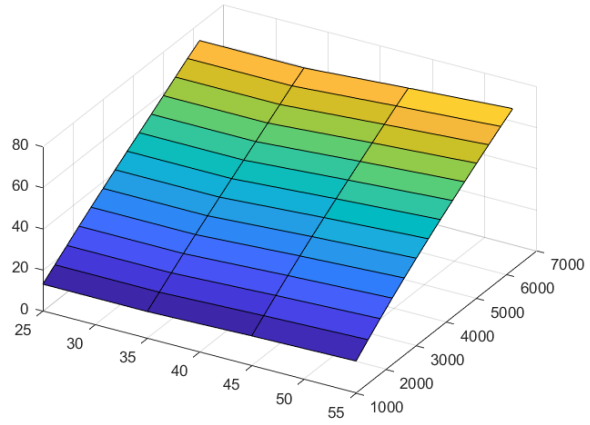

(b)

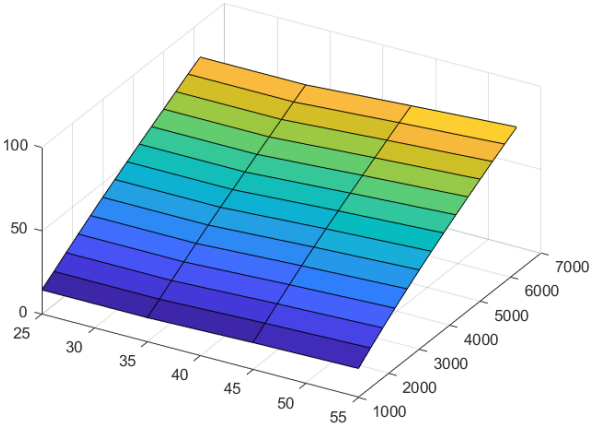

(c)

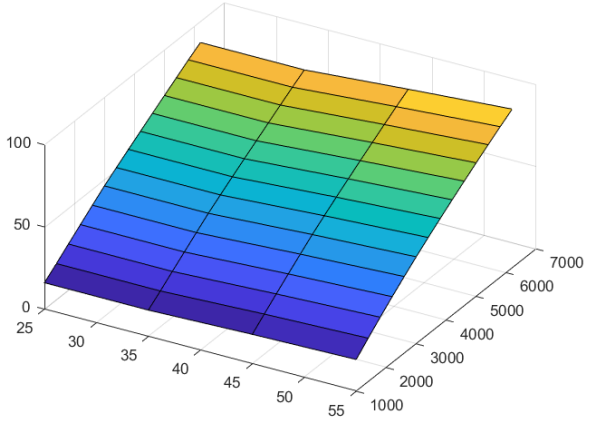

(d)

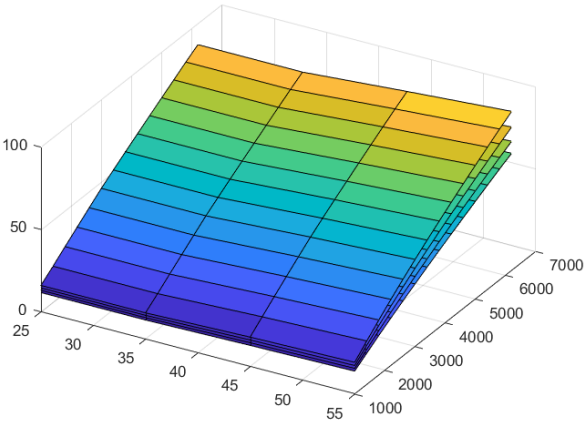
100
50
0
25
30
35
40
45
50
55
1000
2000
3000
4000
5000
6000
7000

(e)

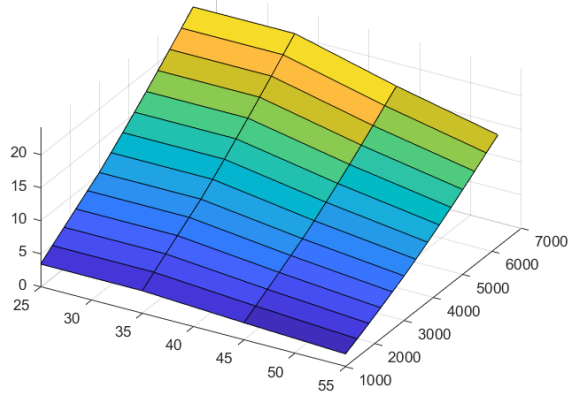
20
15
10
5
0
25
30
35
40
45
50
55
1000
2000
3000
4000
5000
6000
7000

(f)

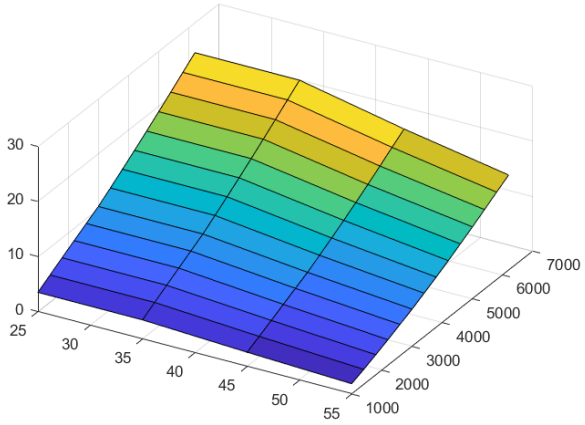
30
20
10
0
25
30
35
40
45
50
55
1000
2000
3000
4000
5000
6000
7000

(g)

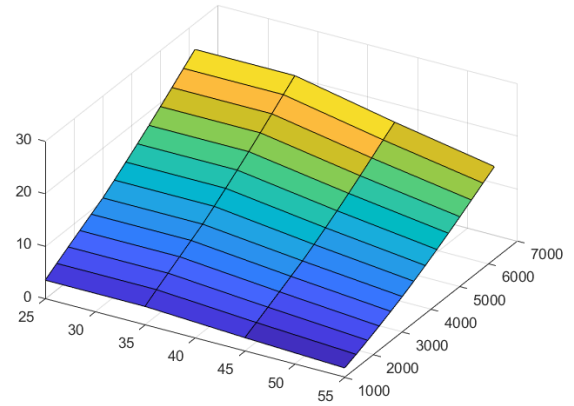
30
20
10
0
25
30
35
40
45
50
55
1000
2000
3000
4000
5000
6000
7000

(h)

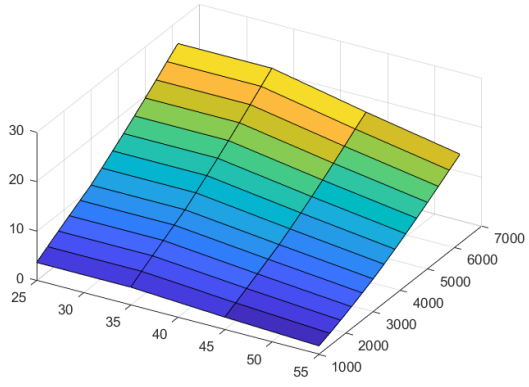
30
20
10
0
25
30
35
40
45
50
55
1000
2000
3000
4000
5000
6000
7000

(i)

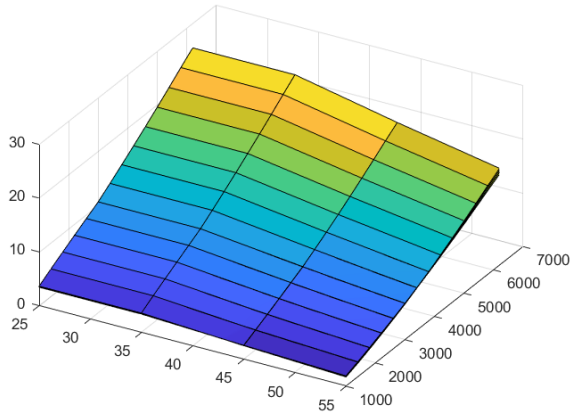
30
20
10
0
25
30
35
40
45
50
55
1000
2000
3000
4000
5000
6000
7000

(j)

Appendix 3 [155]

Nameplate Ratings

Table A1.1 Nameplate Ratings

Rated Voltage	415V
Rated Current	13.89A
Frequency	50Hz
Rated Speed	1500rpm
No. Poles	4
No. Rotor Slots	28
No. Stator Slots	36
Type	B

Blocked Rotor Test Results

Table A1.2 Blocked Rotor Test Results

	Trial 1	Trail 2	Average
U_1	154 V	153.44 V	154.92 V
I_{sc}	13.9 A	13.95 A	13.85 A
P_{in}	2140.5 W	2150.5 W	2145.6 W

Using the average values attained the calculation is done as follows:-
The input power for Y-connected induction machine is expressed as

$$P_{in} = 3I_{sc}^2 R_e = 3I_{sc}^2(R_s + R_r')$$

Where the effective equivalent resistance

$$R_e = R_s + R_r' = P_{in}/(3I_{sc}^2)$$

$$R_e = R_s + R_r' = 2150.43/(3 * 13.9^2)$$

$$\boldsymbol{R_e = 5.43\Omega}$$

The stator resistance can be easily acquired by doing a simple DC test across the windings

Table A1.3 Stator resistance test

	Trail 1	Trail 2	Average
V_{dc}	4.90 V	5 V	4.95 V
I_{dc}	6.12 A	6.25 A	6.17 A

Therefore

$$R_s = \frac{V_{dc}}{I_{dc}} = \frac{4.95}{6.17}$$

$$\boldsymbol{R_s = 0.8\,\Omega}$$

Once the stator resistance is obtained the referred rotor resistance can be computed

$$R_r' = R_e - R_s$$

$$R_r' = 3.71 - 0.8$$

$$\boldsymbol{R_r' = 2.91\Omega}$$

The short circuit impedance of the IM is obtained from

$$Z_{sc} = U_{SC}/I_{sc}$$

Where $U_{SC} = U_1/\sqrt{3}$

$$\boldsymbol{Z_{sc}} = \frac{\left(\frac{154}{\sqrt{3})}\right)}{13.9} = \boldsymbol{6.4\Omega}$$

The sum of the stator leakage reactance X_{s1} and the referred rotor reactance $X_{rl}'$is obtained from

$$X = X_{s1} + X_{r1}' = \sqrt{Z_{sc}^2 - R_e^2}$$

$$\boldsymbol{X} = \sqrt{6.4^2 - 3.71^2} = \boldsymbol{5.21\Omega}$$

For a class B induction motor the empirical proportions is given as

$$X_{s1} = 0.5\boldsymbol{X} \qquad X_{r1}' = 0.5\boldsymbol{X}$$
$$X_{s1} = 0.4 * 5.21 \qquad X_{r1}' = 0.6 * 5.21$$

$$\boldsymbol{X_{s1} = 2.6\Omega} \qquad \boldsymbol{X_{r1}' = 2.6\Omega}$$

NO LOAD test results

Table A1.4 NO LOAD test results

	Trial 1	Trail 2	Average
U_s	414.40 V	415.30 A	414.85 V
I_{nl}	3.72 A	3.67 V	3.69 A
P_{in}	1541.6 W	1524.2 W	1532.9W

The magnetizing current can be obtained as follows

$$U_m = U_s - I_{nl}X_{s1} = \frac{414.85}{\sqrt{3}} - 2.42 * 3.59$$

$$\boldsymbol{U_m = 231.8\,V}$$

Thus the current through the magnetizing branch is

$$I_i = P_{iron/}U_m$$

Taking into consideration the $P_{iron} = P_{in}$
Therefore

$$I_i = P_{in/}U_m = \frac{\frac{1532.9}{3}}{231.8}$$

$$\boldsymbol{I_i = 2.2\,A}$$

Thus the resistance of the iron losses can obtained

$$R_i = \frac{U_m}{I_i} = \frac{230.80}{2.2}$$

$$\boldsymbol{R_i = 105.16\,\Omega}$$

From the calculations done above the magnetizing reactance can be calculated.

$$X_m = \frac{U_m}{I_m}$$

Let $I_m = I_{nl}$
Therefore

$$\boldsymbol{X_m = \frac{231.8}{3.69} = 62.82\Omega}$$

Utilization of the measured parameters in the three-phase induction machines

The parameters $X_{s1}, X'_{r1}\ and\ X_m$ are known, therefore the $L_{s1}, L'_{r1}\ and\ L_m$is obtained by using the formula

The referred magnetizing inductance

$$L_m = \frac{X_m}{2\pi f} = \frac{62.82}{100\pi}$$

$$\boldsymbol{L_m = 0.203\,H}$$

The stator leakage inductance

$$L_{s1} = \frac{X_{s1}}{2\pi f} = \frac{2.6}{100\pi}$$

$$\boldsymbol{L_{s1} = 0.0033\ H}$$

The referred rotor leakage inductance

$$L'_{r1} = \frac{X'_{r1}}{2\pi f} = \frac{5.39}{100\pi}$$

$$\boldsymbol{L'_{r1} = 0.0033\ H}$$

The self-inductance of the stator

$$L_{ss} = L_{s1} + \frac{2}{3}L_m = 0.01 + \frac{2}{3}0.30$$

$$\boldsymbol{L_{ss} = 0.32\ H}$$

The referred self-inductance of the rotor

$$L'_{rr} = L'_{rr} + \frac{2}{3}L_m = 0.02 + \frac{2}{3}0.30$$

$$\boldsymbol{L'_{rr} = 0.22\ H}$$

Mutual inductance between stator windings

$$M_s = -\frac{1}{3}L_m = -\frac{1}{3}0.30$$

$$\boldsymbol{M_s = -0.10\ H}$$

Referred mutual inductance between rotor windings

$$M'_r = -\frac{1}{3}L_m = -\frac{1}{3}0.30$$

$$M'_r = \boldsymbol{-0.10\ H}$$

Maximal value of the referred value of the stator-rotor mutual inductance

$$M'_{sr} = \frac{2}{3}L_m = \frac{2}{3}0.30$$

$$\boldsymbol{M'_{sr} = 0.20\ H}$$

Now the stator and referred inductance can be found out by evaluating

$$L_s = L_{ss} - M_s = \boldsymbol{0.31 - -0.10}$$

$$\boldsymbol{L_s = 0.41H}$$

$$L'_r = L'_{rr} - M'_r = \mathbf{0.22} - -\mathbf{0.10}$$

$$\boldsymbol{L'_r = 0.21\ H}$$

By using the magnetizing, stator and rotor inductance the total leakage factor $\boldsymbol{\sigma}$ can be calculated

$$\sigma = 1 - \frac{L_m^2}{L_s L_r} = 1 - \frac{0.0032^2}{0.0032 * 0.0032}$$

$$\boldsymbol{\sigma = 0.0317}$$

The rotor time constant is formulated by

$$T_r = \frac{L_r^{'}}{R_r^{'}} = \frac{\mathbf{0.21}}{\mathbf{2.91}}$$

$$\boldsymbol{T_r = 0.0709}$$

Stator Transient inductance

$$\boldsymbol{L'_s = \sigma L_s}$$

$$\mathbf{0.41 * 0.14 = 0.0065}\boldsymbol{H}$$

Appendix 4

RLS parameter extraction of RHP

```
                        %%%%%%% Cooling mode %%%%%%%%%%

A=[Speed ODT Twr];
B=[CC];
C=[Pm];

                        %%%%%%% Heating mode %%%%%%%%%%

A=[Speed ODT Twr];
B=[HC];
C=[Pm];

                    %%%%%%%% Parameter for CC and HC %%%%%%%%%

X = (inv(A'*A))*A'*B

t= B-(A*X)

qc=sqrt(mean(t(:,1).^2))
nrmse=qc/(max(B(:,1))-min(B(:,1)))


                       %%%%%%%% Parameter for Pm %%%%%%%%%

Y = (inv(A'*A))*A'*C

u= C-(A*Y)

pm=sqrt(mean(u(:,1).^2))
nrmse1=pm/(max(C(:,1))-min(C(:,1)))
```

Note: Speed, ODT, Twr, CC, HC, and Pm are N sample of data that are acquired from IMSTart software for different mode of operation of the RHP and used to compute the the RHP parameters of each model in chapter 3.

Appendix 5

Scalar Control Scheme

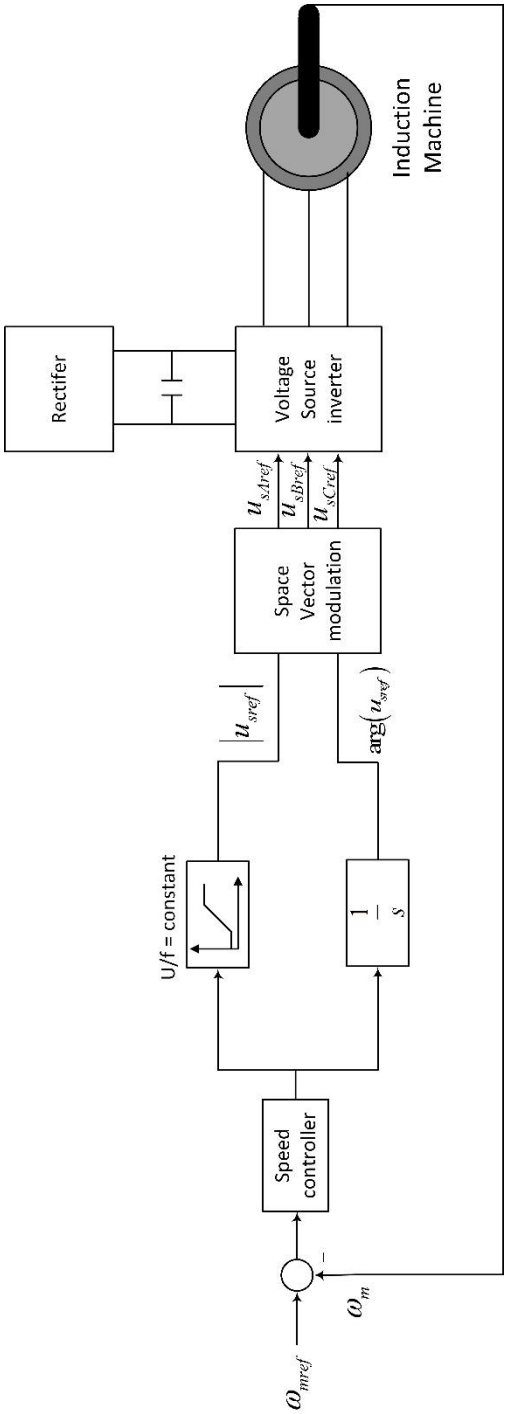

Reference

[1] "Global energy trends 2023 : consolidated energy statistics & world trends." Accessed: Mar. 30, 2024. [Online]. Available: https://www.enerdata.net/publications/reports-presentations/world-energy-trends.html

[2] X. Kang, J. An, and D. Yan, "A systematic review of building electricity use profile models," *Energy and Buildings*, vol. 281. Elsevier Ltd, Feb. 15, 2023. doi: 10.1016/j.enbuild.2022.112753.

[3] https://www.iea.org/energy-system/buildings, "Buildings."

[4] L. Pérez-Lombard, J. Ortiz, and C. Pout, "A review on buildings energy consumption information," *Energy Build*, vol. 40, no. 3, 2008, doi: 10.1016/j.enbuild.2007.03.007.

[5] M. Balbis-Morejón, J. J. Cabello-Eras, J. M. Rey-Hernández, and F. J. Rey-Martínez, "Energy evaluation and energy savings analysis with the 2 selection of ac systems in an educational building," *Sustainability (Switzerland)*, vol. 13, no. 14, 2021, doi: 10.3390/su13147527.

[6] M. de Gastines, É. Correa, and A. Pattini, "Heat transfer through window frames in EnergyPlus: model evaluation and improvement," *Advances in Building Energy Research*, vol. 13, no. 1, 2019, doi: 10.1080/17512549.2017.1421098.

[7] M. Shahrestani, R. Yao, and G. K. Cook, "A fuzzy multiple attribute decision making tool for HVAC&R systems selection with considering the future probabilistic climate changes and electricity decarbonisation plans in the UK," *Energy Build*, vol. 159, 2018, doi: 10.1016/j.enbuild.2017.10.089.

[8] S. Wang, C. Yan, and F. Xiao, "Quantitative energy performance assessment methods for existing buildings," *Energy and Buildings*, vol. 55. 2012. doi: 10.1016/j.enbuild.2012.08.037.

[9] M. González-Torres, L. Pérez-Lombard, J. F. Coronel, I. R. Maestre, and D. Yan, "A review on buildings energy information: Trends, end-uses, fuels and drivers," *Energy Reports*, vol. 8. Elsevier Ltd, pp. 626–637, Nov. 01, 2022. doi: 10.1016/j.egyr.2021.11.280.

[10] Hannah Ritchie, Max Roser, and Pablo Rosado, "Energy," 2023. Accessed: Dec. 04, 2023. [Online]. Available: https://ourworldindata.org/energy

[11] R. McDowall, *Fundamentals of HVAC Systems (IP)*. 2006.

[12] "Energy Performance of Buildings Directive."

[13] "Heat pumps."

[14] P. A. Østergaard, H. Lund, J. Z. Thellufsen, P. Sorknæs, and B. V Mathiesen, "Review and validation of EnergyPLAN," *Renewable and Sustainable Energy Reviews*, vol. 168, p. 112724, 2022, doi: https://doi.org/10.1016/j.rser.2022.112724.

[15] B. V Mathiesen *et al.*, "Smart Energy Systems for coherent 100% renewable energy and transport solutions," *Appl Energy*, vol. 145, pp. 139–154, 2015, doi: https://doi.org/10.1016/j.apenergy.2015.01.075.

[16] A. A. Bashir, A. Lund, M. Pourakbari-Kasmaei, and M. Lehtonen, "Optimizing Power and Heat Sector Coupling for the Implementation of Carbon-Free Communities," *Energies (Basel)*, vol. 14, no. 7, p. 1911, Mar. 2021, doi: 10.3390/en14071911.

[17] D. Fischer and H. Madani, "On heat pumps in smart grids: A review," *Renewable and Sustainable Energy Reviews*, vol. 70, pp. 342–357, 2017, doi: https://doi.org/10.1016/j.rser.2016.11.182.

[18] J. Posma, I. Lampropoulos, W. Schram, and W. van Sark, "Provision of Ancillary Services from an Aggregated Portfolio of Residential Heat Pumps on the Dutch Frequency Containment Reserve Market," *Applied Sciences*, vol. 9, no. 3, 2019, doi: 10.3390/app9030590.

[19] V. Z. Gjorgievski, N. Markovska, A. Abazi, and N. Duić, "The potential of power-to-heat demand response to improve the flexibility of the energy system: An empirical review," *Renewable and Sustainable Energy Reviews*, vol. 138, p. 110489, Mar. 2021, doi: 10.1016/J.RSER.2020.110489.

[20] E. Guelpa and V. Verda, "Demand response and other demand side management techniques for district heating: A review," *Energy*, vol. 219, p. 119440, 2021, doi: https://doi.org/10.1016/j.energy.2020.119440.

[21] J. Salpakari, J. Mikkola, and P. D. Lund, "Improved flexibility with large-scale variable renewable power in cities through optimal demand side management and power-to-heat conversion," *Energy Convers Manag*, vol. 126, pp. 649–661, 2016, doi: https://doi.org/10.1016/j.enconman.2016.08.041.

[22] H. Lund *et al.*, "Perspectives on fourth and fifth generation district heating," *Energy*, vol. 227, p. 120520, 2021, doi: https://doi.org/10.1016/j.energy.2021.120520.

[23] F. D'Ettorre, M. De Rosa, P. Conti, D. Testi, and D. Finn, "Mapping the energy flexibility potential of single buildings equipped with optimally-controlled heat pump, gas boilers and thermal storage," *Sustain Cities Soc*, vol. 50, p. 101689, 2019, doi: https://doi.org/10.1016/j.scs.2019.101689.

[24] Thibault Péan, *Heat Pump Controls to Exploit the Energy Flexibility of Building Thermal Loads*. Spinger, 2020.

[25] E. Sperber, U. Frey, and V. Bertsch, “Reduced-order models for assessing demand response with heat pumps – Insights from the German energy system,” *Energy Build*, vol. 223, p. 110144, 2020, doi: https://doi.org/10.1016/j.enbuild.2020.110144.

[26] L. Zhang, N. Good, and P. Mancarella, “Building-to-grid flexibility: Modelling and assessment metrics for residential demand response from heat pump aggregations,” *Appl Energy*, vol. 233–234, pp. 709–723, Jan. 2019, doi: 10.1016/J.APENERGY.2018.10.058.

[27] B. W. Olesen and O. B. Kazanci, “State of the Art of HVAC Technology in Europe and America,” in *Proceedings of the World Engineering Conference and Convention 2015 (wecc2015)*, 2015.

[28] R. Z. Homod, “Review on the HVAC System Modeling Types and the Shortcomings of Their Application,” *Journal of Energy*, vol. 2013, 2013, doi: 10.1155/2013/768632.

[29] Z. Afroz, G. M. Shafiullah, T. Urmee, and G. Higgins, “Modeling techniques used in building HVAC control systems: A review,” *Renewable and Sustainable Energy Reviews*, vol. 83. 2018. doi: 10.1016/j.rser.2017.10.044.

[30] B. Tashtoush, M. Molhim, and M. Al-Rousan, “Dynamic model of an HVAC system for control analysis,” *Energy*, vol. 30, no. 10, 2005, doi: 10.1016/j.energy.2004.10.004.

[31] N. Nassif, S. Moujaes, and M. Zaheeruddin, “Self-tuning dynamic models of HVAC system components,” *Energy Build*, vol. 40, no. 9, 2008, doi: 10.1016/j.enbuild.2008.02.026.

[32] Y. Chen and S. Treado, “Development of a simulation platform based on dynamic models for HVAC control analysis,” *Energy Build*, vol. 68, no. PARTA, 2014, doi: 10.1016/j.enbuild.2013.09.016.

[33] Z. Lei and M. Zaheeruddin, “Dynamic simulation and analysis of a water chiller refrigeration system,” *Appl Therm Eng*, vol. 25, no. 14–15, 2005, doi: 10.1016/j.applthermaleng.2005.01.002.

[34] D. M. Kumar, P. Catrini, A. Piacentino, and M. Cirrincione, “Advanced modeling and energy-saving-oriented assessment of control strategies for air-cooled chillers in space cooling applications,” *Energy Convers Manag*, vol. 291, 2023, doi: 10.1016/j.enconman.2023.117258.

[35] H. W. Stanford III and H. W. Stanford III, *HVAC Water Chillers and Cooling Towers*. 2003. doi: 10.1201/9780203912492.

[36] C. Vatansever and I. Turetgen, “Investigation of the effects of various stress factors on biofilms and planktonic bacteria in cooling tower model system,” *Arch Microbiol*, vol. 203, no. 4, 2021, doi: 10.1007/s00203-020-02116-2.

[37] A. Zargar, A. Kodkani, B. Vickers, M. R. Flynn, and M. Secanell, “A hybrid cooling tower model for plume abatement and performance analysis,” *Appl Therm Eng*, vol. 219, 2023, doi: 10.1016/j.applthermaleng.2022.119593.

[38] K. Ma, M. Liu, and J. Zhang, “Online optimization method of cooling water system based on the heat transfer model for cooling tower,” *Energy*, vol. 231, 2021, doi: 10.1016/j.energy.2021.120896.

[39] J. A. Romero, J. Navarro-Esbrí, and J. M. Belman-Flores, “A simplified black-box model oriented to chilled water temperature control in a variable speed vapour compression system,” *Appl Therm Eng*, vol. 31, no. 2–3, 2011, doi: 10.1016/j.applthermaleng.2010.09.013.

[40] G. Mustafaraj, J. Chen, and G. Lowry, “Development of room temperature and relative humidity linear parametric models for an open office using BMS data,” *Energy Build*, vol. 42, no. 3, 2010, doi: 10.1016/j.enbuild.2009.10.001.

[41] G. Huang, S. Wang, and X. Xu, “A robust model predictive control strategy for improving the control performance of air-conditioning systems,” *Energy Convers Manag*, vol. 50, no. 10, 2009, doi: 10.1016/j.enconman.2009.06.014.

[42] J. Rehrl and M. Horn, “Temperature control for HVAC systems based on exact linearization and model predictive control,” in *Proceedings of the IEEE International Conference on Control Applications*, 2011. doi: 10.1109/CCA.2011.6044437.

[43] G. Huang, S. Wang, and X. Xu, “Robust model predictive control of VAV air-handling units concerning uncertainties and constraints,” *HVAC and R Research*, vol. 16, no. 1, 2010, doi: 10.1080/10789669.2010.10390890.

[44] Q. Bi *et al.*, “Advanced controller auto-tuning and its application in HVAC systems,” *Control Eng Pract*, vol. 8, no. 6, 2000, doi: 10.1016/S0967-0661(99)00198-7.

[45] G. S. Okochi and Y. Yao, “A review of recent developments and technological advancements of variable-air-volume (VAV) air-conditioning systems,” *Renewable and Sustainable Energy Reviews*, vol. 59. 2016. doi: 10.1016/j.rser.2015.12.328.

[46] A. Afram and F. Janabi-Sharifi, “Review of modeling methods for HVAC systems,” *Applied Thermal Engineering*, vol. 67, no. 1–2. 2014. doi: 10.1016/j.applthermaleng.2014.03.055.

[47] P. P. Angelov and D. P. Filev, “An Approach to Online Identification of Takagi-Sugeno Fuzzy Models,” *IEEE Transactions on Systems, Man, and Cybernetics, Part B: Cybernetics*, vol. 34, no. 1, 2004, doi: 10.1109/TSMCB.2003.817053.

[48] L. Dos Santos Coelho and A. Askarzadeh, “An enhanced bat algorithm approach for reducing electrical power consumption of air conditioning systems based on differential operator,” *Appl Therm Eng*, vol. 99, 2016, doi: 10.1016/j.applthermaleng.2016.01.155.

[49] S. Boahen, J. M. Choi, K. O. Amoabeng, R. Opoku, and G. Y. Obeng, “Efficient control of cascade heat pumps using variable speed compressors,” *Sci Afr*, vol. 18, 2022, doi: 10.1016/j.sciaf.2022.e01399.

[50] I. Watson, “A case study of maintenance of a commercially fielded case-based reasoning system,” *Comput Intell*, vol. 17, no. 2, 2001, doi: 10.1111/0824-7935.00151.

[51] H. Tsutsui and K. Kamimura, “Chiller condition monitoring using topological case-based modeling,” *ASHRAE Trans*, vol. 102, no. 1, 1996.

[52] J. Nishiguchi, T. Konda, and R. Dazai, “Data-driven optimal control for building energy conservation,” in *Proceedings of the SICE Annual Conference*, 2010.

[53] K. Sun, D. Yan, T. Hong, and S. Guo, “Stochastic modeling of overtime occupancy and its application in building energy simulation and calibration,” *Build Environ*, vol. 79, 2014, doi: 10.1016/j.buildenv.2014.04.030.

[54] C. Ghiaus, A. Chicinas, and C. Inard, “Grey-box identification of air-handling unit elements,” *Control Eng Pract*, vol. 15, no. 4, 2007, doi: 10.1016/j.conengprac.2006.08.005.

[55] A. Afram and F. Janabi-Sharifi, “Gray-box modeling and validation of residential HVAC system for control system design,” *Appl Energy*, vol. 137, 2015, doi: 10.1016/j.apenergy.2014.10.026.

[56] H. Blervaque, P. Stabat, S. Filfli, M. Schumann, and D. Marchio, “Variable-speed air-to-air heat pump modelling approaches for building energy simulation and comparison with experimental data,” *J Build Perform Simul*, vol. 9, no. 2, 2016, doi: 10.1080/19401493.2015.1030862.

[57] R. Dott *et al.*, “Models of Sub-Components and Validation for the IEA SHC Task 44 / HPP Annex 38 Part C: Heat Pump Models,” 2013.

[58] B. Birdsall, W. Buhl, and K. Ellington, “Overview of the DOE-2 building energy analysis program,” *Report LBL-19735m …*, 1990.

[59] C. J. Banister, W. R. Wagar, and M. R. Collins, “Validation of a single tank, multi-mode solar-assisted heat pump TRNSYS model,” in *Energy Procedia*, 2014. doi: 10.1016/j.egypro.2014.02.059.

[60] U. Camdali, M. Bulut, and N. Sozbir, “Numerical modeling of a ground source heat pump: The Bolu case,” *Renew Energy*, vol. 83, 2015, doi: 10.1016/j.renene.2015.04.030.

[61] W. Wei *et al.*, “Technical, economic and environmental investigation on heating performance of quasi-two stage compression air source heat pump in severe cold region,” *Energy Build*, vol. 223, 2020, doi: 10.1016/j.enbuild.2020.110152.

[62] M. Abdelghani, E. A. Mahmoud, A. S. Abdel-Khalik, and H. F. Soliman, “An improved post-fault controller for asymmetrical six-phase induction machine using fractional order PI current controllers,” in *2017 19th International Middle-East Power Systems Conference, MEPCON 2017 - Proceedings*, 2017. doi: 10.1109/MEPCON.2017.8301184.

[63] K. Ohyama and T. Kondo, “Energy-saving technologies for invester air conditioners,” *IEEJ Transactions on Electrical and Electronic Engineering*, vol. 3, no. 2. 2008. doi: 10.1002/tee.20254.

[64] B. Blunier, M. Pucci, M. Cirrincione, G. Cirrincione, and A. Miraoui, “A scroll compressor with a high-performance sensorless induction motor drive for the air management of a PEMFC system for automotive applications,” *IEEE Trans Veh Technol*, vol. 57, no. 6, 2008, doi: 10.1109/TVT.2008.919618.

[65] H. B. Marulasiddappa and V. Pushparajesh, “Review on different control techniques for induction motor drive in electric vehicle,” *IOP Conf Ser Mater Sci Eng*, vol. 1055, no. 1, 2021, doi: 10.1088/1757-899x/1055/1/012142.

[66] C. B. Rasmussen, E. Ritchie, and A. Arkkio, “Variable speed induction motor drive for household refrigerator compressor,” in *IEEE International Symposium on Industrial Electronics*, 1997. doi: 10.1109/isie.1997.649045.

[67] O. Solomon and P. Famouri, “On efficiency and performance improvement of three-phase induction motors in refrigeration and HVAC applications,” in *IEEE Green Technologies Conference*, 2021. doi: 10.1109/GreenTech48523.2021.00097.

[68] H. Ahn, H. Park, C. Kim, and H. Lee, “A Review of State-of-the-art Techniques for PMSM Parameter Identification,” *Journal of Electrical Engineering and Technology*, vol. 15, no. 3, 2020, doi: 10.1007/s42835-020-00398-6.

[69] Q. Wang, S. Wang, and C. Chen, “Review of sensorless control techniques for PMSM drives,” *IEEJ Transactions on Electrical and Electronic Engineering*, vol. 14, no. 10, 2019, doi: 10.1002/tee.22974.

[70] A. A. Abdelhafez, M. A. Aldalbehi, N. F. Aldalbehi, F. R. Alotaibi, N. A. Alotaibia, and R. S. Alotaibi, “Comparative Study for Machine Candidates for High Speed Traction Applications,” 2017.

[71] S. I. Cosman, V. I. Boanca, C. Oprea, and C. S. Martis, “Design, Building and Testing of a Low Voltage-High Current Drive for SRMs Used for HVAC Applications,” in *EPE 2018 - Proceedings of the 2018 10th International Conference and Expositions on Electrical And Power Engineering*, 2018. doi: 10.1109/ICEPE.2018.8559845.

[72] B. Bilgin, J. W. Jiang, and A. Emadi, *Switched Reluctance Motor Drives Fundamentals to Applications*. 2019.

[73] G. S. Lukose, S. Paramasivam, and M. Vijayakumar, “A review of various converter topologies for SRM drives,” in *SAE International Journal of Alternative Powertrains*, 2014. doi: 10.4271/2014-01-1881.

[74] Y. Liao, G. Huang, Y. Sun, and L. Zhang, “Uncertainty analysis for chiller sequencing control,” *Energy Build*, vol. 85, 2014, doi: 10.1016/j.enbuild.2014.09.037.

[75] R. H. Wang, S. H. Jia, and G. Liu, “Saving-energy control method of the water-circling pump in winter heating,” in *Proceedings - 2012 9th International Conference on Fuzzy Systems and Knowledge Discovery, FSKD 2012*, 2012. doi: 10.1109/FSKD.2012.6234253.

[76] P. H. Shaikh, N. B. M. Nor, P. Nallagownden, I. Elamvazuthi, and T. Ibrahim, “A review on optimized control systems for building energy and comfort management of smart sustainable buildings,” *Renewable and Sustainable Energy Reviews*, vol. 34. 2014. doi: 10.1016/j.rser.2014.03.027.

[77] I. W. Eames, A. Milazzo, and G. G. Maidment, “Modelling thermostatic expansion valves,” *International Journal of Refrigeration*, vol. 38, no. 1, 2014, doi: 10.1016/j.ijrefrig.2013.06.010.

[78] C. Aprea and R. Mastrullo, “Experimental evaluation of electronic and thermostatic expansion valves performances using R22 and R407C,” *Appl Therm Eng*, vol. 22, no. 2, 2002, doi: 10.1016/S1359-4311(01)00071-0.

[79] R. Lazzarin and M. Noro, “Experimental comparison of electronic and thermostatic expansion valves performances in an air conditioning plant,” *International Journal of Refrigeration*, vol. 31, no. 1, 2008, doi: 10.1016/j.ijrefrig.2007.09.004.

[80] F. W. Yu, K. T. Chan, and H. Y. Chu, “Constraints of using thermostatic expansion valves to operate air-cooled chillers at lower condensing temperatures,” *Appl Therm Eng*, vol. 26, no. 17–18, 2006, doi: 10.1016/j.applthermaleng.2005.11.018.

[81] Y. Sun *et al.*, “Development of an optimal control method of chilled water temperature for constant-speed air-cooled water chiller air conditioning systems,” *Appl Therm Eng*, vol. 180, p. 115802, Nov. 2020, doi: 10.1016/J.APPLTHERMALENG.2020.115802.

[82] D. M. Kumar, P. Catrini, A. Piacentino, and M. Cirrincione, “Advanced modeling and energy-saving-oriented assessment of control strategies for air-cooled chillers in space cooling applications,” *Energy Convers Manag*, vol. 291, p. 117258, Sep. 2023, doi: 10.1016/J.ENCONMAN.2023.117258.

[83] R. S. Foss and R. Story, “FUNDAMENTALS OF COMPRESSED AIR SYSTEMS.,” *Plant Engineering (Barrington, Illinois)*, vol. 35, no. 14, 1981.

[84] J. K. Jensen, M. R. Kærn, P. H. Pedersen, and W. B. Markussen, “Comparison of compressor control strategies for energy efficient refrigerated counters,” *International Journal of Refrigeration*, vol. 126, 2021, doi: 10.1016/j.ijrefrig.2021.02.008.

[85] S. W. Yu, Y. J. Jung, S. H. Kim, J. H. Jo, Y. S. Kim, and Y. H. Cho, “A study on the optimized control strategies of geothermal heat pump system and absorption chiller-heater,” *Int J Energy Res*, vol. 38, no. 8, 2014, doi: 10.1002/er.3122.

[86] S. Wang and X. Xu, “Effects of alternative control strategies of water-evaporative cooling systems on energy efficiency and plume control: A case study,” *Build Environ*, vol. 43, no. 11, 2008, doi: 10.1016/j.buildenv.2007.11.017.

[87] J. S. H. Teo, K. H. Law, and V. C. C. Lee, “Energy Management Controls for Chiller System: A Review,” in *2021 International Conference on Green Energy, Computing and Sustainable Technology, GECOST 2021*, 2021. doi: 10.1109/GECOST52368.2021.9538754.

[88] E. Sperber, U. Frey, and V. Bertsch, “Reduced-order models for assessing demand response with heat pumps – Insights from the German energy system,” *Energy Build*, vol. 223, p. 110144, Sep. 2020, doi: 10.1016/J.ENBUILD.2020.110144.

[89] M. Szreder and M. Miara, “Effect of heat capacity modulation of heat pump to meet variable hot water demand,” *Appl Therm Eng*, vol. 165, p. 114591, 2020, doi: https://doi.org/10.1016/j.applthermaleng.2019.114591.

[90] N. A. Efkarpidis, S. A. Vomva, G. C. Christoforidis, and G. K. Papagiannis, “Optimal day-to-day scheduling of multiple energy assets in residential buildings equipped with variable-speed heat pumps,” *Appl Energy*, vol. 312, p. 118702, Apr. 2022, doi: 10.1016/J.APENERGY.2022.118702.

[91] L. Schibuola, M. Scarpa, and C. Tambani, “Demand response management by means of heat pumps controlled via real time pricing,” *Energy Build*, vol. 90, pp. 15–28, Mar. 2015, doi: 10.1016/J.ENBUILD.2014.12.047.

[92] L. Maier, M. Schönegge, S. Henn, D. Hering, and D. Müller, “Assessing mixed-integer-based heat pump modeling approaches for model predictive control applications in buildings,” *Appl Energy*, vol. 326, p. 119894, 2022, doi: https://doi.org/10.1016/j.apenergy.2022.119894.

[93] H. Liu and J. Cai, “Improved superheat control of variable-speed vapor compression systems in provision of fast load balancing services,” *International Journal of Refrigeration*, vol. 132, pp. 187–196, 2021, doi: https://doi.org/10.1016/j.ijrefrig.2021.08.028.

[94] J. Clauß and L. Georges, “Model complexity of heat pump systems to investigate the building energy flexibility and guidelines for model implementation,” vol. 255, p. 113847, 2019, doi: https://doi.org/10.1016/j.apenergy.2019.113847.

[95] G. Bagarella, R. M. Lazzarin, and B. Lamanna, “Cycling losses in refrigeration equipment: An experimental evaluation,” *International Journal of Refrigeration*, vol. 36, no. 8, pp. 2111–2118, Dec. 2013, doi: 10.1016/J.IJREFRIG.2013.07.020.

[96] M. Cirrincione, M. Pucci, and G. Vitale, *Power converters AC electrical drives: With linear neural networks*. 2017. doi: 10.1201/b12073.

[97] P. Vas, “Electrical machines and drives : a space-vector theory approach,” *Monographs in electrical and electronic engineering 25*, 1992.

[98] F. C. McQuiston, J. D. Parker, and J. D. Spitler, *Heating, Ventilating, and Air Conditioning Analysis and Design*, vol. 91. 2005.

[99] H. W. Stanford, *HVAC Water Chillers and Cooling Towers: Fundamentals, Application, and Operation, Second Edition*. 2016. doi: 10.1201/b11510.

[100] O. Arsenyeva, L. Tovazhnyanskyy, P. Kapustenko, J. J. Klemeš, and P. S. Varbanov, “Review of Developments in Plate Heat Exchanger Heat Transfer Enhancement for Single-Phase Applications in Process Industries,” *Energies*, vol. 16, no. 13. 2023. doi: 10.3390/en16134976.

[101] J. Claesson, “Thermal and hydraulic characteristics of brazed plate heat exchangers - Part I: Review of single-phase and two-phase adiabatic and flow boiling characteristics,” in *ASHRAE Transactions*, 2005.

[102] A. Sadeghianjahromi and C. C. Wang, “Heat transfer enhancement in fin-and-tube heat exchangers – A review on different mechanisms,” *Renewable and Sustainable Energy Reviews*, vol. 137. 2021. doi: 10.1016/j.rser.2020.110470.

[103] G. Lorentzen, “Principles of refrigeration,” *International Journal of Refrigeration*, vol. 3, no. 3, 1980, doi: 10.1016/0140-7007(80)90102-4.

[104] I. Dincer and M. A. Rosen, *Exergy Analysis of Heating, Refrigerating and Air Conditioning: Methods and Applications*. 2015. doi: 10.1016/C2013-0-06800-4.

[105] M. H. Rashid, *Power Electronics Handbook: Devices, Circuits, and Applications, Third Edition*. 2010. doi: 10.1016/B978-0-12-382036-5.00053-7.

[106] V. Michele and D. Diego, *Le Centrali Frigorifere*. 2015.

[107] W. Kim, “Fault detection and diagnosis for air conditioners and heat pumps based on virtual sensors,” 2013. [Online]. Available: https://api.semanticscholar.org/CorpusID:109685996

[108] W. Kim and S. Katipamula, “A review of fault detection and diagnostics methods for building systems,” *Sci Technol Built Environ*, vol. 24, no. 1, 2018, doi: 10.1080/23744731.2017.1318008.

[109] D. M. Kumar, H. K. Mudaliar, M. Cirrincione, U. Mehta, and M. Pucci, “Design of a Fractional Order PI (FOPI) for the Speed Control of a High-Performance Electrical

Drive with an Induction Motor," *ICEMS 2018 - 2018 21st International Conference on Electrical Machines and Systems*, pp. 1198–1202, Nov. 2018, doi: 10.23919/ICEMS.2018.8549407.

[110] M. Cirrincione, M. Pucci, and V. G., *Power converters and AC electrical drives with linear neural networks*. CRC Press, 2016.

[111] A. Arteconi and F. Polonara, "Assessing the Demand Side Management Potential and the Energy Flexibility of Heat Pumps in Buildings," *Energies 2018, Vol. 11, Page 1846*, vol. 11, no. 7, p. 1846, Jul. 2018, doi: 10.3390/EN11071846.

[112] J. E. Braun, S. A. Klein, and J. W. Mitchell, "Effictiveness models for cooling towers and cooling coils," United States, 1989. [Online]. Available: https://www.osti.gov/biblio/5770692

[113] Sabiana, "'Carisma' Fan Coils (Product specifications)." 2022. [Online]. Available: https://www.sabiana.it/en/products/carisma-crc

[114] "EFFECTIVENESS MODELS FOR COOLING TOWERS AND COOLING COILS." Accessed: Apr. 02, 2024. [Online]. Available: https://iifiir.org/en/fridoc/effectiveness-models-for-cooling-towers-and-cooling-coils-10188

[115] C. Naldi and E. Zanchini, "Dynamic simulation during summer of a reversible multi-function heat pump with condensation-heat recovery," *Appl Therm Eng*, vol. 116, pp. 126–133, Apr. 2017, doi: 10.1016/J.APPLTHERMALENG.2017.01.066.

[116] R. O'Hegarty, O. Kinnane, D. Lennon, and S. Colclough, "Air-to-water heat pumps: Review and analysis of the performance gap between in-use and product rated performance," *Renewable and Sustainable Energy Reviews*, vol. 155, p. 111887, Mar. 2022, doi: 10.1016/J.RSER.2021.111887.

[117] S. H. Lee, Y. Jeon, H. J. Chung, W. Cho, and Y. Kim, "Simulation-based optimization of heating and cooling seasonal performances of an air-to-air heat pump considering operating and design parameters using genetic algorithm," *Appl Therm Eng*, vol. 144, pp. 362–370, Nov. 2018, doi: 10.1016/J.APPLTHERMALENG.2018.08.078.

[118] P. Artuso *et al.*, "Dynamic Modelling and Validation of an Air-to-Water Reversible R744 Heat Pump for High Energy Demand Buildings," *Energies 2021, Vol. 14, Page 8238*, vol. 14, no. 24, p. 8238, Dec. 2021, doi: 10.3390/EN14248238.

[119] P. Hu, Q. Hu, Y. Lin, W. Yang, and L. Xing, "Energy and exergy analysis of a ground source heat pump system for a public building in Wuhan, China under different control strategies," *Energy Build*, vol. 152, 2017, doi: 10.1016/j.enbuild.2017.07.058.

[120] D. Del Col, M. Azzolin, G. Benassi, and M. Mantovan, “Experimental analysis of optimal operation mode of a ground source heat pump system,” in *Energy Procedia*, 2014. doi: 10.1016/j.egypro.2014.01.142.

[121] R. S. Adhikari, N. Aste, M. Manfren, and D. Marini, “Energy savings through variable speed compressor heat pump systems,” in *Energy Procedia*, 2012. doi: 10.1016/j.egypro.2011.12.964.

[122] T. Y. Kim, J. M. Lee, Y. Yoon, and K. H. Lee, “Application of Artificial Neural Network Model for Optimized Control of Condenser Water Temperature Set-Point in a Chilled Water System,” *Int J Thermophys*, vol. 42, no. 12, pp. 1–17, Dec. 2021, doi: 10.1007/S10765-021-02922-W/METRICS.

[123] W. Hee Kang, Y. Yoon, J. Hyeon Lee, K. Woo Song, Y. Tae Chae, and K. Ho Lee, “In-situ application of an ANN algorithm for optimized chilled and condenser water temperatures set-point during cooling operation,” *Energy Build*, vol. 233, p. 110666, Feb. 2021, doi: 10.1016/J.ENBUILD.2020.110666.

[124] J. Deng, W. Qiang, C. Peng, Q. Wei, and H. Zhang, “Research on systematic analysis and optimization method for chillers based on model predictive control: A case study,” *Energy Build*, vol. 285, p. 112916, Apr. 2023, doi: 10.1016/J.ENBUILD.2023.112916.

[125] C. Fan and X. Zhou, “Model-based predictive control optimization of chiller plants with water-side economizer system,” *Energy Build*, vol. 278, p. 112633, Jan. 2023, doi: 10.1016/J.ENBUILD.2022.112633.

[126] M. Dongellini, M. Abbenante, and G. L. Morini, “A strategy for the optimal control logic of heat pump systems: impact on the energy consumptions of a residential building,” *12th IEA Heat Pump Conference 2017*, 2017.

[127] F. Illán-Gómez, J. R. García-Cascales, F. Hidalgo-Mompeán, and A. López-Belchí, “Experimental assessment of the replacement of a conventional fin-and-tube condenser by a minichannel heat exchanger in an air/water chiller for residential air conditioning,” *Energy Build*, vol. 144, pp. 104–116, Jun. 2017, doi: 10.1016/J.ENBUILD.2017.03.041.

[128] B. D. Mselle, G. Zsembinszki, D. Vérez, E. Borri, and L. F. Cabeza, “A detailed energy analysis of a novel evaporator with latent thermal energy storage ability,” *Appl Therm Eng*, vol. 201, 2022, doi: 10.1016/j.applthermaleng.2021.117844.

[129] B. D. Mselle *et al.*, “Experimental Assessment of the Influence of the Design on the Performance of Novel Evaporators with Latent Energy Storage Ability,” *Applied Sciences (Switzerland)*, vol. 12, no. 4, 2022, doi: 10.3390/app12041813.

[130] B. Doğan, M. M. Ozturk, T. Tosun, M. Tosun, and L. B. Erbay, “A novel condenser with offset strip fins on a mini channel flat tube for reducing the energy consumption

of a household refrigerator," *Journal of Building Engineering*, vol. 44, 2021, doi: 10.1016/j.jobe.2021.102932.

[131] K. R. Sagar, H. B. Naik, and H. B. Mehta, "Novel condenser based cryogenic pulsating heat Pipe: Investigations on influence of geometrical parameters," *Cryogenics (Guildf)*, vol. 126, 2022, doi: 10.1016/j.cryogenics.2022.103543.

[132] M. Catarino, P. Barandier, and A. J. M. Cardoso, "Retrofit of a Heat Pump Unit †," *Engineering Proceedings*, vol. 24, no. 1, 2022, doi: 10.3390/IECMA2022-12902.

[133] P. Barandier and A. J. Marques Cardoso, "A review of fault diagnostics in heat pumps systems," *Applied Thermal Engineering*, vol. 228. Elsevier Ltd, Jun. 25, 2023. doi: 10.1016/j.applthermaleng.2023.120454.

[134] P. Barandier and A. J. Marques Cardoso, "Asset Management and Energy Improvements in a Critical Environment – The Case of a University Bioterium," in *Lecture Notes in Mechanical Engineering*, 2022. doi: 10.1007/978-3-030-96794-9_33.

[135] A. J. M. Cardoso, *Diagnosis and fault tolerance of electrical machines, power electronics and drives*. 2018. doi: 10.1049/PBPO126E.

[136] D. P. Yuill and J. E. Braun, "Evaluating the performance of fault detection and diagnostics protocols applied to air-cooled unitary air-conditioning equipment," in *HVAC and R Research*, 2013. doi: 10.1080/10789669.2013.808135.

[137] J. E. Braun, "Automated fault detection and diagnostics for vapor compression cooling equipment," *Journal of Solar Energy Engineering, Transactions of the ASME*, vol. 125, no. 3. 2003. doi: 10.1115/1.1591001.

[138] I. Bellanco, E. Fuentes, M. Vallès, and J. Salom, "A review of the fault behavior of heat pumps and measurements, detection and diagnosis methods including virtual sensors," *Journal of Building Engineering*, vol. 39. 2021. doi: 10.1016/j.jobe.2021.102254.

[139] J. J. Aguilera *et al.*, "A review of common faults in large-scale heat pumps," *Renewable and Sustainable Energy Reviews*, vol. 168, p. 112826, Oct. 2022, doi: 10.1016/J.RSER.2022.112826.

[140] I. Bellanco, E. Fuentes, M. Vallès, and J. Salom, "A review of the fault behavior of heat pumps and measurements, detection and diagnosis methods including virtual sensors," *Journal of Building Engineering*, vol. 39, p. 102254, Jul. 2021, doi: 10.1016/J.JOBE.2021.102254.

[141] H. Li, J. E. Braun, R. W. H. Laboratories, and W. Lafayette, "An Economic Evaluation of Automated Fault Detection and Diagnosis for Rooftop Air Conditioners," *Refrigeration And Air Conditioning*, no. 1997, 2004.

[142] M. S. Mirnaghi and F. Haghighat, “Fault detection and diagnosis of large-scale HVAC systems in buildings using data-driven methods: A comprehensive review,” *Energy Build*, vol. 229, p. 110492, Dec. 2020, doi: 10.1016/J.ENBUILD.2020.110492.

[143] M. S. Breuker and J. E. Braun, “Common faults and their impacts for rooftop air conditioners,” *HVAC and R Research*, vol. 4, no. 3, 1998, doi: 10.1080/10789669.1998.10391406.

[144] M. Mehrabi and D. P. Yuill, “Normalized Effect Of Condenser Fouling And Refrigerant Charge On Performance Of Vapor Compression Air Conditioning Systems,” 2016.

[145] D. Noel, P. Riviere, C. Teuillieres, O. Cauret, D. Marchio, and D. Marchio Experimental, “Experimental Characterization of Fault Impacts on the Functioning Variables of an Inverter Driven Heat Pump,” p. 1968818, 2018, Accessed: Jun. 02, 2023. [Online]. Available: https://hal-mines-paristech.archives-ouvertes.fr/hal-01968818

[146] D. C. Lee, M. Lee, W. Cho, and Y. Kim, “Performance improvement of heat pumps by optimizing refrigerant charge using novel variable liquid-line length system,” *Appl Therm Eng*, vol. 196, 2021, doi: 10.1016/j.applthermaleng.2021.117287.

[147] M. Mehrabi and D. Yuill, “Generalized effects of refrigerant charge on normalized performance variables of air conditioners and heat pumps,” *International Journal of Refrigeration*, vol. 76, 2017, doi: 10.1016/j.ijrefrig.2017.02.014.

[148] H. Li and J. E. Braun, “Decoupling features and virtual sensors for diagnosis of faults in vapor compression air conditioners,” *International Journal of Refrigeration*, vol. 30, no. 3, 2007, doi: 10.1016/j.ijrefrig.2006.07.024.

[149] Y. Hu and D. P. Yuill, “Non-condensable gas in the refrigerant of air-source heat pumps: Interactions between detection features, charge level, and temperature,” *International Journal of Refrigeration*, 2023, doi: 10.1016/j.ijrefrig.2022.10.006.

[150] T. S. Park, S. H. Kim, N. J. Kim, J. Y. Yoo, and G. T. Park, “Speed-sensorless vector control of an induction motor using recursive least square algorithm,” *IEEE International Electric Machines and Drives Conference Record, IEMDC*, 1997, doi: 10.1109/IEMDC.1997.604231.

[151] D. C. Huynh, M. W. Dunnigan, and S. J. Finney, “On-line parameter estimation of an induction machine using a recursive least-squares algorithm with multiple time-varying forgetting factors,” *PECon2010 - 2010 IEEE International Conference on Power and Energy*, pp. 444–449, 2010, doi: 10.1109/PECON.2010.5697624.

[152] A. Piacentino and C. Barbaro, “A comprehensive tool for efficient design and operation of polygeneration-based energy μgrids serving a cluster of buildings. Part

II: Analysis of the applicative potential," *Appl Energy*, vol. 111, pp. 1222–1238, Nov. 2013, doi: 10.1016/j.apenergy.2012.11.079.

[153] D. M. Kumar, P. Catrini, A. Piacentino, and M. Cirrincione, "Advanced modeling and energy-saving-oriented assessment of control strategies for air-cooled chillers in space cooling applications," *Energy Convers Manag*, vol. 291, p. 117258, Sep. 2023, doi: 10.1016/J.ENCONMAN.2023.117258.

[154] J. B. Castro, J. F. Urchueguía, J. M. Corberán, and J. Gonzálvez, "Optimized design of a heat exchanger for an air-to-water reversible heat pump working with propane (R290) as refrigerant: Modelling analysis and experimental observations," *Appl Therm Eng*, vol. 25, no. 14–15, pp. 2450–2462, Oct. 2005, doi: 10.1016/J.APPLTHERMALENG.2004.12.009.

[155] "IEEE Standard Test Procedure for Polyphase Induction Motors and Generators," *IEEE Std 112-2017 (Revision of IEEE Std 112-2004)*, pp. 1–115, 2018, doi: 10.1109/IEEESTD.2018.8291810.